Screening of water pollutants using metallophthalocyanine-based chemically modified electrodes

by

Kevin Kantize

Submitted in the fulfilment of the requirements for the degree of

Master of Science

in the School of Chemistry and Physics at the

University of KwaZulu-Natal

May 2021

Supervisor: Prof. Irvin N. Booysen

Co-supervisor: Dr. Allen Mambanda

TABLE OF CONTENTS

Chapter 4

Electrocatalytic determination of mercury cations at the interfaces of gold electrodes modified with self-assembled monolayers of cobalt phthalocyanines and electropolymerized 3-hexylthiophene films

Chapter 5

Electrocatalytic determination of nevirapine using a platinum electrode modified with a polymeric CoPc-nafion-carbon nanotube composite

Chapter 6

Conclusions and future work

ABSTRACT

Rapid and accurate screening of organo-pharmaceuticals and heavy metals in water reservoirs are of utmost importance as elevated concentrations of these emerging pollutants can have detrimental consequences to animal and human health. Moreover, the monitoring of water quality in rural areas is challenging since analytical laboratories is often non-existent or poorly equipped and lack the necessary skilled workforce to operate sophisticated instrumentation. However, these techniques are either time consuming or demand tedious extraction processes prior to detection which is very inconvenient in routine sample analysis. MPcs are well known for their molecular recognition capability which are promoted by their metal- and ligand based redox properties while the latter can be readily influenced by the stereo-electronic properties of the substituents. This research study focused on the synthesis and characterization of cobalt(II) phthalocyanines (CoPcs) with analyte targeting aromatic substituents as well as exploring their application as selective and sensitive electrocatalytic sensors for water pollutants including Acetaminophen (commonly known as Paracetamol), mercury and Nevirapine.

In the first experimental chapter, multiwalled carbon nanotubes (MWCNTs) conjugates of cobalt phthalocyanines with peripherally *tetra*-substituted flavone or benzoxazole (CoPc-flav/benzoaxole-*f*-MWCNTS) were fabricated, characterized by transmission electron microscopy as well as infrared spectroscopy (IR). Their respective suspension mixtures were drop-casted onto the surface of a glassy carbon electrode to form CoPc-flav-*f*-MWCNTs and CoPc-benz-*f*-MWCNTs-GCEs. The chemically modified electrodes (CME) were used as electrocatalytic detectors for paracetamol which has been reported in high concentration in various location in KwaZulu-Natal. Under optimized conditions, the peak currents for CoPc-flav-*f*-MWCNTs- and CoPc-bo-*f*-MWCNTs- GCEs were linear in wide acetaminophen concentration ranges of 1 – 1000 μM and 15 – 1000 μM

respectively. Electron transfer kinetics of the CMEs were superior to the bare electrode where diffusion- and convection-controlled electrocatalytic constants were in the order of $10^2$and 10^4 $M^{-1}s^{-1}$ were obtained for the CMEs. Good selectivity was attained when tested in the presence of other emerging water pollutants.

In the second experimental chapter, *in-situ* fabrication of gold electrodes was performed by self-assembled monolayer (SAM) formations of peripherally furan (**3**) or benzothiazole (**4**) substituted cobalt phthalocyanines followed by electropolymerization of 3-hexylthiophene (3-HT) molecules (SAMs-**3**|Poly(3-HT) or SAMs-**4**|Poly(3-HT) Au electrodes). The resultant chemically modified electrodes (CMEs) portrayed optimal electrocatalytic activities during the voltammetric detection of Hg(I) and Hg (II) cations. Operational parameters including the accumulation potential, accumulation time and pH studies were fine-tuned and optimized. SAMs-**3**|Poly(3-HT) and SAMs-**4**|Poly(3-HT) Au electrodes showed linear ranges in the concentration ranges of 1.48 x 10^{-5} and 4.06 x 10^{-5} M, respectively. The SAMs-CoPc-furan|Poly (3-HT) Au electrode could reliably quantify Hg (II) in the surface water of a river sample with good accuracy and the excellent recovery of 104% attained, provided confidence in the standard addition method as well as the integrity of the CME. The CMEs displayed excellent discriminatory capabilities in the presence of other divalent metal cations.

In the final experimental chapter, sequential drop-casting of a suspension comprising of conjugate of *f*-MWCNTs and coumarin *tetra*-substituted CoPc, followed by the immobilization of 5% Nafion resin solution (Naf-5) on a Pt electrode rendered the CME, CoPc- *f*-MWCNTs/Naf-5/Pt. The resultant CME could selectively detect the antiretroviral drug, Nevirapine (NVP) in the presence of other common organic pollutants. In addition, linear sweep voltammetric responses were linear in the concentration ranges of 0.6 nM to 30 μM whilst its chronoamperometric responses were

linear in the concentration of 4 nM to 30 μM, with an excellent lower detection limits of 0.212 nM and 2.5 nM respectively. Moreover, the CME was used to detect the presence of NVP in a river water sample with a good percentage recovery of 110%.

Keywords: Metallophthalocyanines, coumarin, benzothiazole, furan, benzoxazole, linear sweep voltammetry, carbon nanotubes, Nafion and 3-hexylthiophene.

PREFACE

The experimental work described in this dissertation was carried out in the School of Chemistry and Physics at the University of KwaZulu-Natal, Pietermaritzburg, from January 2018 to April 2021, under the supervision of Prof. Irvin Noel Booysen and co-supervision of Dr. Allen Mambanda.

These studies represent original work by the author and have not otherwise been submitted in any form for any degree or diploma to any tertiary institution. Where use has been made of the work of others, it is duly acknowledged in the text.

DECLARATION 1–PLAGIARISM

I, Kevin Kantize, declare that:

1. The research reported in this dissertation, except where otherwise indicated, is my original research.
2. This dissertation has not been submitted for any degree or examination at any other university.
3. This dissertation does not contain any other persons' data, pictures, graphs or other information, unless specifically acknowledged as being sourced from other persons.
4. This dissertation does not contain any other persons' writing, unless specifically acknowledged as being sourced from other researchers. Where other written sources have been quoted, then:
    a. Their words have been re-written but the general information attributed to them has been referenced.
    b. Where their exact words have been used, then their writing has been placed in italics and inside quotation marks and referenced.
5. This dissertation does not contain text, graphics or tables copied and pasted from the internet, unless specifically acknowledged, and the source being detailed in the dissertation and in the References section.

Signed: 

DECLARATION 2–PUBLICATIONS

Manuscripts published:

1. **Kantize, K**., Booysen, I.N. and Mambanda, A., **2019**. Electrochemical sensing of acetaminophen using nanocomposites comprised of cobalt phthalocyanines and multiwalled carbon nanotubes. *Journal of Electroanalytical Chemistry*, *850*, p.113391.

2. **Kantize, K**., Ngwenya, V., Booysen, I.N. and Mambanda, A., **2021**. Electrocatalytic determination of mercury cations at the interfaces of gold electrodes modified with self-assembled monolayers of cobalt phthalocyanines and electropolymerized 3-hexylthiophene films. *Polyhedron*, *203*, p.115235 .

Manuscript in preparation:

1. **Kantize, K**., Booysen, I.N. and Mambanda, A., Electrocatalytic determination of nevirapine using a platinum electrode modified with a polymeric CoPc-nafion-carbon nanotube composite**.**

The compounds involved in all the aforementioned manuscripts have been synthesized, Kevin Kantize

Signed: [redacted] Date: 5/05/2021

Supervisors:

Prof. I.N. Booysen

[redacted]

Signed: _____ Date: 5/05/2021

Dr. A. Mambanda

Signed: [redacted] Date: 5/05/2021

ACKNOWLEDGEMENTS

First and foremost, I would like to thank God, the creator of heaven and earth, the one every creature should bow to, for his blessings, provision, protection throughout my life and more so during my master's studies, all glory belongs to you Lord!!!

I would like to thank my supervisor, Prof. I.N. Booysen for the time he has invested in my research, the guidance, and the motivation to be able to reach the target goal, is deeply appreciated. The intellectual capacity you have transferred to me will go a long way in building the next generation of electrochemists.

I would like to thank Dr Mambanda for his critical insights and time he has dedicated towards the completion of this research.

I am grateful to the technicians in the school of chemistry for their help and fruitful discussion for various characterization techniques. I am also thankful to the University of KwaZulu-Natal for enabling me to make use of their laboratory and LAN facilities to be able to conduct my research.

I am grateful for the Nation Research Foundation for sponsoring this important research.

I would like to thank unreservedly The Nelson Mandela Rhodes Foundation for their financial support during this research study.

I would like to thank my fellow research members; Vuyelwa Ngwenya, Zabenguni Mthombothi, Siyabonga Shoba, Shabaaz Abdullah, Patrick Mangundu, Daniel Makanyane and Danica Moodley, you have made my research journey a whole lot easier with your different contributions. I am grateful to have been in the same research group.

This research work is solely dedicated to both my late Father Edouard Niyungeko and my mentor, my uncle and my second Father Ernest Nkunzimana, I know that you are proud of your son! To conclude, I would like to thank my mother Spès-Caritas Kanyange, my aunty Esperande Bigirimana, my sister Nabelle Nagateka, my nephew Zayne Jayden Migisha and the rest of the family for their love and support, I LOVE YOU!

Chapter One
Introduction

1.1 General background

Since their early discovery in the early 1900s, metallopthalocyanines (MPcs) have found themselves at the centre of an intense investigations.[1, 2] Their early application entailed mainly dyes used in the textile industry. Since then their applications have grown significantly and include a wide spectrum of practices *viz.* medical technologies such as potential dynamic therapy (PDT) and clean energy generators as in fuel cells.[3-6] Relevant to this study, is the capability of MPcs to serve as current signal enhancers in thin films on the surface of electrodes.[7]

MPcs are highly conjugated planar metallocyclic complexes which share a similar structural skeleton to haemoproteins such as Haemoglobin, Vitamin B_{12} and Cytochromes.[8] In particular, the aforementioned biomolecules contains four isoindole groups that are linked together by four nitrogen atoms. MPcs can undergo coordination at the central metal ion (*e.g.* Mn(OAc)Pc) as well as the attachment of peripheral and/or non-peripheral substitutions on the ring system, see **Fig. 1.1**.[9] The electrochemical properties of MPcs are significantly dependent on the nature of the substituents and their positioning as well as the metal centre, which underline their versatility in different applications.[10, 11]

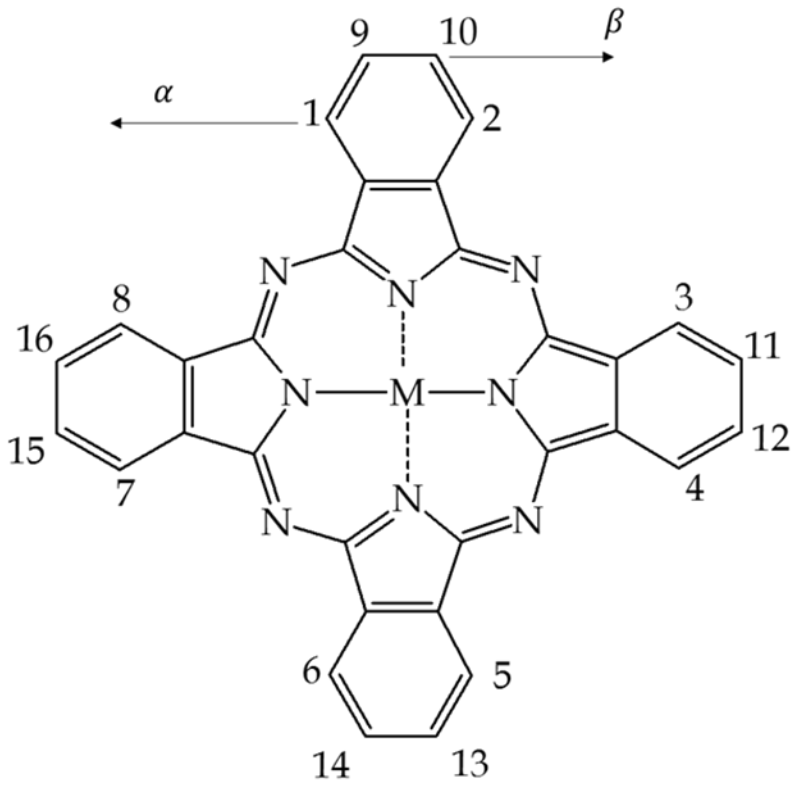

Fig. 1.1: *General structure of Metallophthalocyanines (MPcs) where the alpha- and beta-substitution positions are indicated by arrows.*

1.2 Motivation and aim of the study

Chemically modified electrodes (CMEs) with electron-mediating thin films have attracted widespread attention of material scientists and electrochemists.[12, 13] This is a result of their superior electrocatalytic activities achieved by increasing the surface area and electron transfer kinetics of the working electrode. In addition, CMEs can afford no, or less surface fouling compared to their corresponding bare substrates.[14, 15] Meticulous selection of the elementary components for a thin film is imperative to achieve high sensitivity and selectivity towards a desired analyte.[16, 17] Another prerequisite of an optimally functional electrochemical sensor is reproducibility which can also be directly

correlated to the robustness of CMEs.[18] Consequently, the electrode modification technique must be carefully considered to promote strong adhesion between the interfacial layer of the substrate and the conductive thin film.[18-20]

Electrochemical sensors offer numerous advantages compared to traditional analytical techniques, which include cost effectiveness, portability, simple to use and faster analyte determination amongst others.[21] Nonetheless, more research is still required to enhance the sensitivity and the selectivity of electrochemical sensors. In the quest to find new materials for CMEs, nanomaterials and their nanoconjugates have emerged and have been incorporated into thin films that have been immobilized on various electrodes.[21, 22] Generally, the modified substrates with nanohybrids offer increased surface area and electrical conductivity, culminating into higher electrocatalytic responses but lower redox potentials.[22, 23]

Numerous structure-activity relationships of Metallophthalocyanines (MPcs) have been derived, and through the diverse structural features of MPcs, their redox, photophysical and electronic properties can be manipulated.[24] MPcs can form nano films on the surfaces of several substrates *via* various electrode modifications methods and these MPc-based electrochemical sensors have portrayed electrocatalytic sensing capabilities to various analytes largely owing to the 18π-metallocyclic generic structure.[18] Literature trends are showing that substituents have critical roles to play, not only in altering metal- or Pc-based redox properties within the potential window of the analytes by promoting the discrimination of detection of analytes.[25, 26] The latter is of particular importance due to the complex make-up of real samples such as biological or polluted water samples.[27]

Herein, heterocyclic moieties as peripheral substituents have been used on the Pc core to promote the distinctive detection of pharmaceutically derived pollutants or mercuric cations, see **Fig. 1.2**. The rationale behind the selection of these heterocyclic moieties stems from their similar stereo-electronic properties with the pharmaceuticals or that complementary intermolecular interactions which can favourably occur between the former and the latter.[28, 29] For example, a sensitive GCE electrode modified with a non-symmetrical CoPc containing benzothiazole moieties was used to selectively detect Hg^{2+} in a multifarious sample and in tap water. This CoPc was anchored to the surface of a GCE *via* a cycloaddition reaction between the electrochemically grafted azides and alkynyl mast-groups of the CoPcs. Incidentally, the coordination affinity of the heavy metal pollutants towards the sulphur donor atoms of the benzothiazole played a central role in the mechanism of electrocatalysis.[30]

In the quest to increase the electrode sensitivity, MPcs are often coupled with carbon nanotubes or polymers.[31, 32] In particular, the extended *pi*-conjugation of multiwalled carbon nanotubes' (MWCNTs') network structure generally encourages higher redox currents for MPc-based electrochemical sensors.[31] Moreover, functionalization of MWCNTs can render stable MPc nanoconjugates and depending on the chemical modification approach, a mixture of functionalized MWCNTs with a MPc can be immobilized on working electrodes.[33] In addition, the CMEs comprising of MWCNTs and MPcs generally increase their effective surface area and mechanical stability.[34, 35]

Electrochemically-conducting polymers have been incorporated into thin films on various substrates.[36, 37] These polymeric electron mediators offer several advantages including higher surface area, faster diffusion of redox species, good adhesion to the bare substrates and lower electrode modification costs. In addition, this class of CMEs can

have a unique mode of electrocatalysis whereby their polymer components can act as ion-exchange polymers that accumulates the analyte of interest depending on their structures.[38] In fact, the specificity of these electrode modifiers towards analytes is often governed by the Lewis acid-base complexation interaction.[39] Molecularly imprinting of polymers is another emerging electrode alteration technique that besides the core benefits of polymeric CMEs, affords compactness to the latter which is an essential step for miniaturizing the electrochemical sensing technology.[40]

Lately, there have been reports on the increasing concentrations of pharmaceuticals in water sources globally.[41, 42] The escalating prominence of these pharmaceutically-derived pollutants is largely attributed to the population "boom" and the advancement of modern medicine. Matongo *et al.* reported a wide distribution of pharmaceuticals in the Msunduzi river based in KwaZulu-Natal (KZN) using a high-performance liquid chromatography (HPLC-MS/MS) detection technique. More specifically, a high acetaminophen concentration of 1.74 μg L^{-1} was found in close proximity of residential and industrial areas.[43] Similarly, Wood *et al.* detected the presence of many anti-retroviral drugs at various major rivers and dams, using an ultra-high pressure liquid chromatography tandem mass spectrometry (UHPLC-MS/MS), with an upper limit of 1480 ng L^{-1} for Nevirapine in the Roodeplaat Dam system.[44] Also, Abafe *et al.* noted the persistence of Nevirapine in the effluents of three wastewater treatment plants (WWTPs) with concentrations in the range of 540 – 1900 ng L^{-1} using liquid chromatography tandem mass spectrometry (LC-MS/MS).[45] Recently, there was a report on the widespread Hg contamination emanating from an unsecured waste-storage facility located at Cato Ridge KZN, which may have contaminated surrounding streams, ground water and affecting local communities.[46]

Adverse consequences of these emerging contaminants are huge both for humans and aquatic life. Paracetamol is known to cause serious health issues such as

hepatotoxicity and nephrotoxicity when used above recommended dosage.[47, 48] On the other hand mercury in its different forms is a well-known acute toxin agent, with far more reaching dire consequences such as hypoxia,[49] Minamata disease,[50] and acrodynia.[51] Nevirapine has also shown to cause skin exanthem as well as hepatotoxicity.[52] The United States Environmental Protection Agency (US EPA) set a maximum contaminant level (MCL) for mercury in drinking water at 2 μg L^{-1}.[53] Thus, it is imperative that the water quality be preserved by keeping the heavy metal concentrations below the threshold that can have dire consequences to human and animal life.

Therefore, the main aims of the research project were to:

- synthesize and characterise substituted phthalonitriles with the respective heterocyclic groups,
- probe the redox properties of the novel CoPcs,
- construct the various chemically modified electrodes (CMEs), and confirm of surface modification for the respective CMEs,
- optimize the electroanalytical parameters for the individual CMEs for optimal electrocatalysis,
- investigate the electrocatalytic detection capabilities of the CMEs towards the respective analytes,
- determine the diffusion and convection-controlled electron transfer kinetics of the CMEs,
- assess the reproducibility and stability of the individual CMEs,
- deduce the mechanism of electrocatalysis,
- examine the respective CMEs' selectivities and sensitivities in samples containing various interferents,
- and apply the CMEs for qualitative and quantitative analysis of the analytes in real water samples.

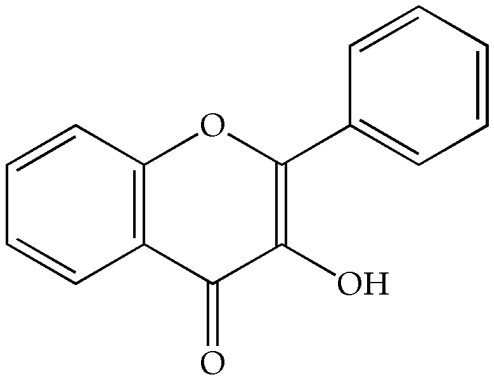

3-hydroxyflavone

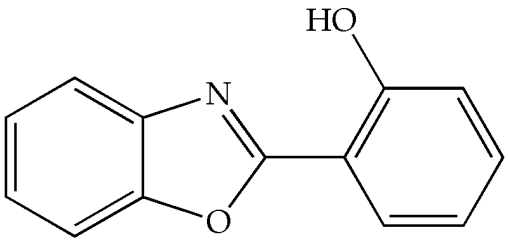

2-hydroxyphenylbenzoxazole

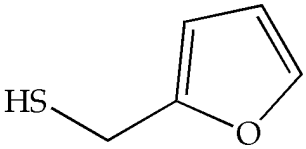

2-furanmethanethiol

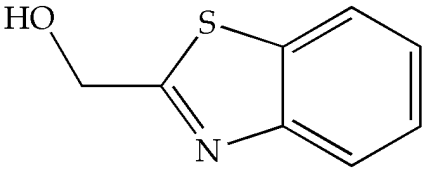

2-hydroxymethylbenzothiazole

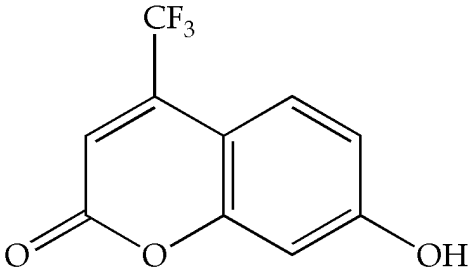

7-hydroxy-4-trifluoromethylcoumarin

Fig. 1.2: *Molecular structures of the different heterocyclic moieties.*

1.3 Electronic properties of MPcs

MPcs exhibit characteristic absorption bands that play a critical role in their inherent photocatalytic activities. As shown in **Figure 1.3**(**a**), MPcs show two characteristics absorption bands namely the Soret bands or commonly known as *B*-bands in the region of 300 - 450 nm, a vibronic band which are typically near and in blue-shifted regions relative to intense *Q*-bands in the region of 600-800 nm. These absorption bands occur due to the л – л* intraligand transitions of the highly conjugated Pc system except for the vibronic band which corresponds to n - л* transitions. According to Gouterman's model, the *B*-band is observed due to the electron transitions from the a_{2u}, b_{2u} (HOMO orbitals) to e_g (LUMO orbital) while the *Q*-bands arise from the a_{1u} to e_g transitions, see **Figure 1.3**(**b**). Evidently, *B*-bands are typically broader compared to the *Q*-bands because of the superimposition of the B_1- and B_2-bands.

The introduction of metal ion in the cavity of the Pc ring is known to cause a blue shift in the *Q*-band, this is a result of the metal ion decreasing the electron density of the Pc ring. As electro-positivity of metal cations is increased, greater blue shifts in the *Q*-bands are induced. In addition, the stereo-electronic properties of the substituents on the Pc ring can also dictate the position of the *Q*-band. More specifically, it is well known that electron-donating groups decreases the HOMO-LUMO gap, thus leading to more bathochromic-shifted *Q*-bands.[54] In contrast, MPcs with electron-withdrawing substituents, experience hypsochromic shifts of their corresponding electronic transitions.[55] Literature trends illustrate that the position of the substituents can also affect where the *Q*-bands occurs. For instance, *octa*-substituted MPcs with electron donating thioether substituents at the peripheral positions caused a red shift of the *Q* band's absorbance peak maximum relative to their corresponding *tetra*-substituted MPcs.[56]

Effects of organic solvents on the electronic spectra of MPcs have been widely investigated.[57] Coordinating solvents such as DMF or DMSO to redox active metal centres have shown to shift the *Q*-bands to higher wavelengths during aggregation studies.[58] Tandem formations of broad electronic transitions in the region of 450 - 550 nm are observed as the result of the *d*-orbitals of the metals positioned within the band-gap energy of Pc ring resulting in charge transfer bands, *viz.* Ligand to Metal charge transfer (LCMT) or metal-to-ligand charge transfer (MLCT).[59]

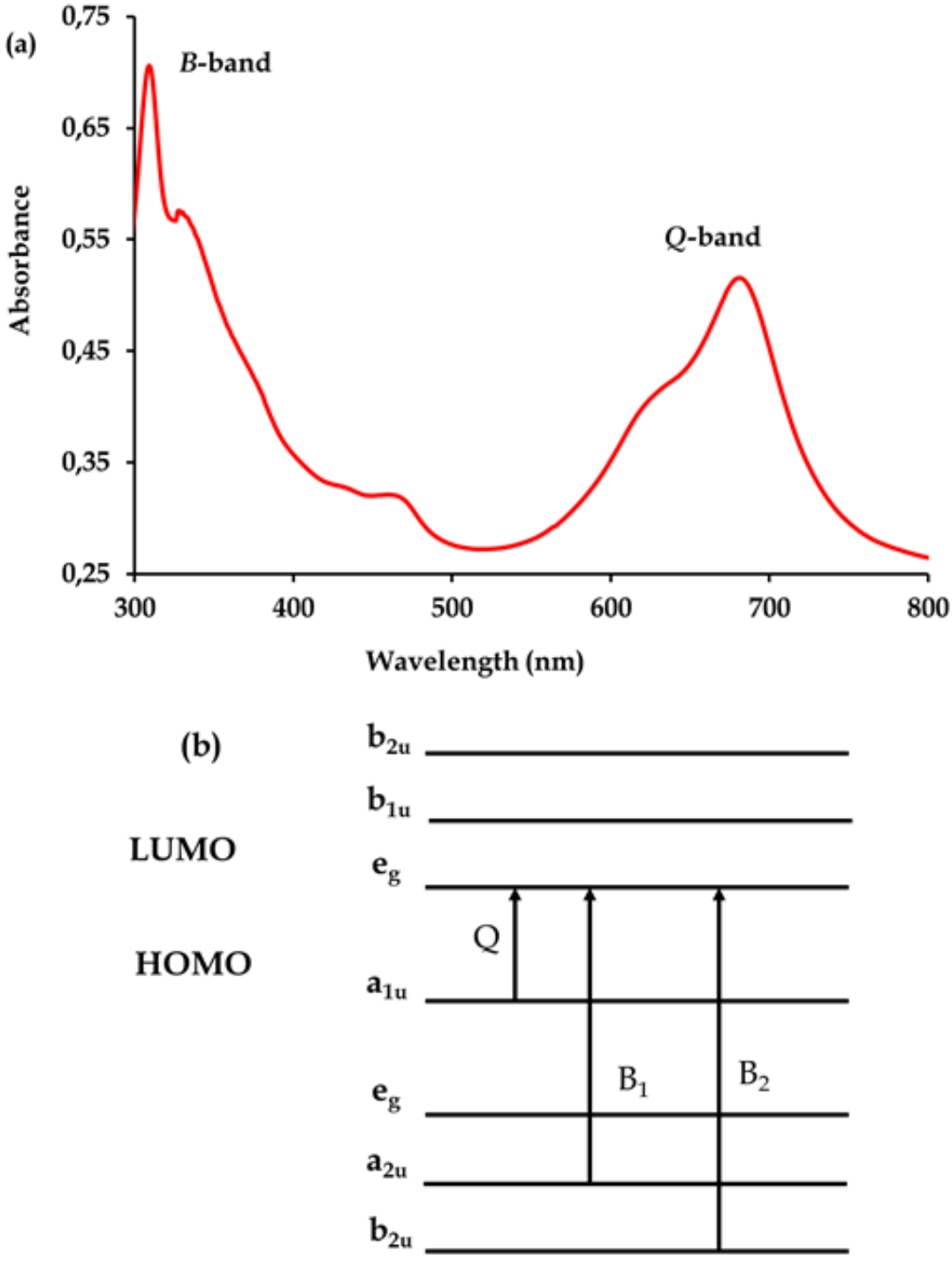

Fig. 1.3: *(**a**) A typical absorption spectrum of a tetrasubstituted with 2-methylbenzothiazole metallophthalocyanine and (**b**) the Gouterman's model, indicating electron transitions.*

1.4 Redox properties of MPcs

Metallophthalocyanines are electron rich metal complexes with an extended π-conjugation system, and as such, they can promote redox transformations. Oxidation of the Pc ring will entail the removal of 2 consecutives electrons from the a_{1u} orbital to form Pc^{-1} and Pc^{0} species. The reduction, on the other hand, which is the addition of electrons to the e_g orbital of the LUMO, can result in the formation of Pc^{3-} and Pc^{4-} species.[60, 61] The e_g orbitals are doubly degenerate and hence can accommodate four electrons to allow for several reductions of Pc^{2-}.

For Pcs containing redox active metal centres within their cavities, metal-redox based reactions will be observed.[62] Electrochemical properties of MPcs are influenced by the nature of solvents, metal centres, substituents and their positions on the metallocyclic rings. For example, CuPcs *octa*-substituted with non-peripheral hexyloxy moieties or *tetra*-substituted with chloro and 2-naphthoxy groups, rendered higher redox potentials than other CuPcs found in literature.[63] The coordinating solvents improved the reversibility of redox processes as opposed to non-coordinating solvents.[64]

UV-Vis spectroelectrochemistry is a dynamic technique which is often used to affirm redox properties of MPcs. Consequently, this technique allows a means of conducting tandem qualitative and quantitative analysis.[63, 65, 66] A Pc reduction ring-centred redox process is readily distinguished by decreasing intensity in the *Q*-band as well as the appearance of a new CT band in the region of 500 – 600 nm.[67, 68] It is also noteworthy to mention that during the spectroelectrochemical experiments, the solution of the metal complex changes colour inside the OTTLE cell.[65] Metal-based redox processes manifest by shifts in the *Q*-bands.[67]

1.5 Application of MPcs

Currently, there is widespread interest in fine-tuning the physico-chemical properties of MPcs for applications such as sensors, solar cells, therapeutic and degradation agents.[3, 69, 70] More often, the MPcs nanoconjugates have shown higher efficacy than their parent metal complexes as the quantum confinement of electron density and the surface areas of nanomaterials enhances the physical properties of MPcs. Herein, a portrayal of the versatility of MPcs as electrochemical sensors is presented, however a brief overview of other applications will also be highlighted.

1.5.1 Fundamentals of MPc-based electrocatalysis

A simplified definition of electrocatalysis is the increase in electron transfer rates during an electrochemical reaction by means of an electron-mediating thin film that has been immobilized on the interface of an electrode. MPcs act as electrocatalysts by forming thin film layers on the electrode surfaces which acts as electron mediator between the analyte and the substrate. On the contrary, upon the use of bare electrodes for the electrocatalytic detections of analytes, the responses are normally sluggish due to high overpotentials or may even be undetectable. Therefore, the fundamental electrocatalytic action of MPcs is to effectively promote these redox reactions by reducing the activation energy, thereby lowering the overpotentials and increasing the redox currents.

Furthermore, there has been a significant interest in the monitoring of pharmaceuticals and heavy metals.[42, 71] The sudden interest was prompted by a paucity of information on their occurrence mainly in water bodies especially on the African continent.[42, 71] The analytical field has seen a remarkable development over the years and the pool of analytical techniques are extensively known and developed. Traditional analytical techniques include HPLC-MS-TOF,[72] spectrophotometry,[73] chemiluminescence[74] to name but a few. Although they can conduct multi-analysis of analytes and can detect sufficiently lower concentrations, they are tedious, their

maintenance is very expensive, they are also not portable and most importantly they are normally not for field workers, low level and semi-skilled scientists.

In the quest to improve the aforementioned disadvantages of traditional analytical techniques, electrochemical techniques have been extensively sought after due to their simplicity, easy portability, user-friendliness, low cost and can also detect at low concentrations. Several sensors have been developed to detect a wide spectrum of analytes. The sensors can be named depending on the recognition element used, the transducer elements or the output signal, *e.g.* chemical sensor,[75] immunosensor,[76] DNA sensor,[77] cell sensor[78] *etc.*

In electrochemical sensing systems, there are four important components that are critical to its functioning, namely, the recognition element, transducer element, analyte of interest and a signal processor, see **Fig. 1.4**. The recognition element interacts with the analyte through chemical or physical means. The transducer in turn measures out the interaction as an electrical response which correspond to the concentration of analyte present.

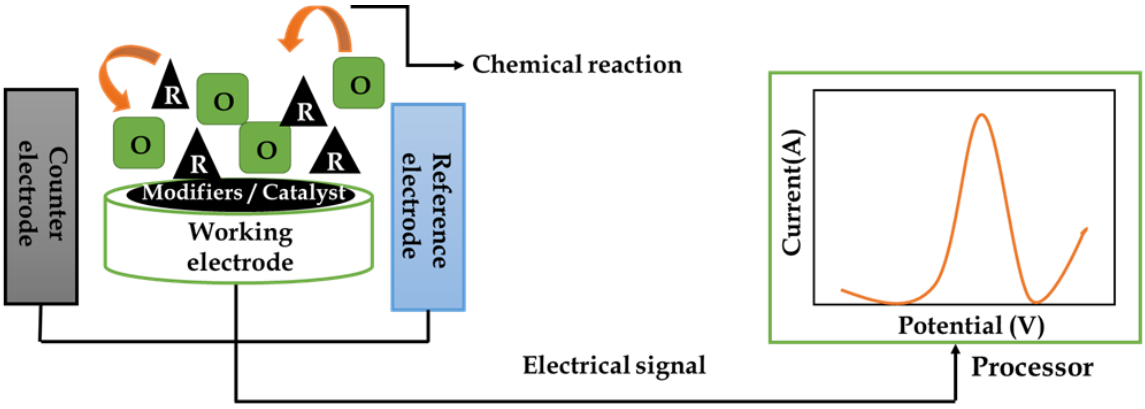

Fig. 1.4: *A general framework and a depicted mechanism of electrocatalysis for an electrochemical sensor.*

1.5.1.1 Recent trends in electrochemical sensor development

This research study focused on the detection of the heavy metal cations of mercury, pharmaceuticals, including the mild pain reliever, paracetamol and the antiretroviral drug (ARVD), Nevirapine. As such, an update on the latest trends in developments of electrochemical sensors for the detection of these analytes is pertinent.

Heavy metal and their cations are well known to pose a serious health and environmental hazards due to their high toxicity. As reiterated, various sophisticated laboratory scale instrumentation has been used for the detection and concentration determination of these species but can be inconvenient for daily routine analysis and within the field analysis, especially within our rural areas where communities rely on natural water reservoirs.[79] Thus, scientists are actively engaged to sought after alternative electrochemical detection methods.[80]

Bodji *et al.* proposed a class of mesoporous silica nanoparticles with intrinsic properties such high surface area and an ease of functionalization. Through carefully designed and controlling pores sizes, these class of materials can be tailored for the detection of various analytes. A mesoporous silica material *viz* siliceous mesostructured cellular foam (MCF) was synthesized with increased surface area as well as with a controlled pore size distribution. To further increase its selectivity towards Hg^{2+}, dithizone a sulfur containing organic molecule was embedded in the mesostructured material, which subsequently led to a low voltammetric detection at picomolar level.[81] Lu *et al.* prepared a glassy carbon electrode (GCE) modified with a graphene aerogel (GA) and metal-organic framework (MOF) UiO-66-NH_2 composites for simultaneous detection of heavy metals. Due to its structural features, GA's role was not only a support structure to UiO-66-NH_2, but also enhanced the conductivity of the composites. UiO-66-NH_2 provided binding sites between the hydrophilic groups and the metal cations. The developed method showed excellent selectivity

towards Cd^{2+}, Pb^{2+}, Cu^{2+} and Hg^{2+} when in the presence of other interferences. The results suggested that the GA modified GCE could be used in detecting heavy-metals ions in complicated sample matrices.[82]

Recently pharmaceuticals have become a concern due to their ease of availability as well as their difficulties in removing them from water treatment plants. Consequently, these pharmaceutically-derived pollutants have found their way into water sources and some have potential endocrine disruptions both to humans and marine life.[83] Paracetamol is an over-the-counter analgesic and antipyretic drug which is widely used for pain relief. As such, it is easily abused and can found its way into water sources, hence the monitoring a very crucial exercise.

Fu *et al.* used a polyoxometalate *viz* $Cu_3Mo_2O_9$ to modify a glassy carbon electrode. The resultant CME afforded excellent electrocatalytic activity which stem from their linkage between the respective metals with the oxygen donors of the electron-mediating thin films. The detection capabilities of the CME can be manipulated by rearranging the Cu ions' positions within the material. Consequently, the optimized CME exhibited selective and high responses towards paracetamol in a biological sample.[84] Carefully design of the substituents is of critical importance. A cobalt *tetra*-substituted with cysteine was used to modify the glassy carbon electrode for the sensitive voltammetric detection of both paracetamol and 4-aminophenol (4-AP). The biological moiety presented structural similarities with the analytes, thereby enhancing strong adhesion. The fabricated sensor achieved nanomolar detections and showed excellent recovery of 4-AP when tested in complex matrices.[28]

A sensitive and selective sensor based on a molecular imprinted polymer (MIP) on the carbon paste electrode for the voltammetric determination of the ARV drug, Nevirapine was proposed. The successful fabrication of molecular MIPs encompasses the target molecule in their network, which is subsequently removed. The blueprinted

binding site is an excellent connector with the targeted molecule. The sensor provided an excellent linear calibration range as well as lower detection limit.[85]

1.5.1.2 Fuel cells

Proton exchange membrane (PEM) fuel cells possess an immense potential as environmentally friendly power generators due to their low/zero emission, high energy power densities compared to other traditional power generation units. They have potential application as a plausible alternative clean power generation in both stationary and portable devices.[86, 87] They convert chemical energy of different fuels into electricity without combustion. However, more research is needed to reach the commercialization ambition. The major obstacles usually encountered include reliability, durability and high cost. The electrocatalyst and the polymer electrolyte are at the core of the limiting factor for both the acid PEM and alkaline fuel cells, respectively.[86] Pt-based catalysts for fuel cell reactions are unsustainable due to their high cost and limited source, thus research and development have concentrated in finding alternatives materials.

A wide range of non-precious metal-containing materials such as cobalt phthalocyanines,[88] transition metal chalcogenide[89] and metal carbide[90] have emerged as possible alternative to platinum. Interest in the pursuit of non-platinum-containing electrocatalysts for oxygen reduction reactions (ORR) was sparked by Jasinski in the 1960s who pioneered the discovery of Cobalt phthalocyanine (CoPc) with ORR catalytic activity in alkaline systems.[91] Subsequent research studies have revealed that a mononuclear iron Pc promote a four-electron reduction pathway while a monomeric cobalt Pc induces a two electron-system during electrocatalysis.[92] Interestingly, the mixture of iron and cobalt porphyrins displayed a superior higher electrocatalytic efficiency for ORR the respective MPcs, *i.e.* CoPc or FePc.[93] The trend was rationalized based on the preferential interaction between two different transition metals and

dimolecular oxygen molecules which could promote the O-O bond breakage and induce reduction to water. Furthermore, a heptadecafluorodecyl-substituted, pentaerythritol-bridged ball-type dinuclear Co_2Pc_2 showed significant electrocatalytic activity towards ORR in acidic medium. This was thought to be due to the two opposing CoPc units' metal centres and multiple electrons withdrawing groups at the periphery of the MPc units, which in return promoted the O-O bond breakage and favouring the easier reduction to water.[94]

Although they have been significant improvements, MPc-based electrocatalysts still face challenges surviving the harsh operating conditions of PEM fuels cells which results in demetallation. The ORR is a complex process proceeding with several intermediates. The two half-reactions can be simplified as:

Anode: $2H_2 \longrightarrow 4H^+ + 4e^-$

Cathode: $O_2 + 4H^+ + 4e^- \longrightarrow 2H_2O$

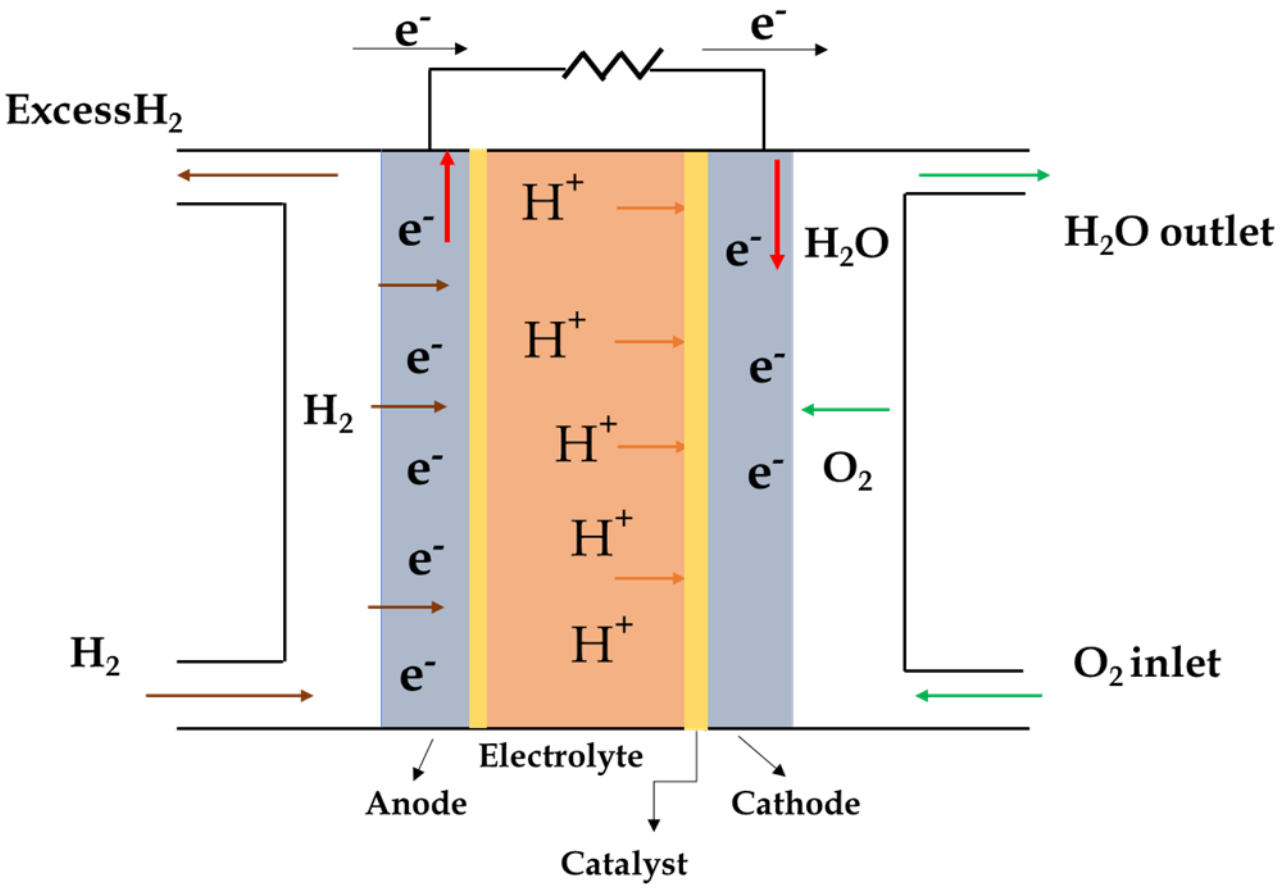

Fig. 1.5: *A cross-section of a general PEM fuel cell.*

1.5.2 Electrochemical remediation of pollutants

Electrochemical degradation of pollutants is an important technique in addressing the current challenges of safely transforming recalcitrant pollutants.[95, 96] There is a significant paucity of literature reports on the electrochemical remediation of pollutants using chemically modified electrodes with MPcs. Nonetheless, a definitive illustration of this application is the electrocatalytic degradation of acid red 1 (AR 1), a synthetic red dye which is used as a food additive, using cobalt tetraaminophthalocyanine covalently linked to a carbon fiber (CF).[97] Upon the incorporation of the MPc onto the CF network, an enhanced electrocatalytic degradation of the pollutant is observed owing it to the increased formation of H_2O_2.

The MPc reacts with dissolved O_2 producing H_2O_2 whereby through ionisation process of the hydrogen peroxide, a hydroperoxyl radical coordinates to the metal centre, generating an intermediate MPc species which is responsible for the degradation of the pollutant.

1.6 Electrode modification techniques

Amongst the challenges scientists had to overcome, were the improvement of sluggish responses and surface fouling of the bare electrode. In the process, substrates have been modified using various methods ranging from the simple drop-dry method (which is governed by adsorption) to electrodeposition and electropolymerization where molecules align in a regular manner through intermolecular interactions or direct covalent bonding. In addition, spontaneous covalent bonding can occur between sulphur containing MPcs and gold electrodes which afford self-assembled monolayers (SAMs). The subsections below highlight in brief each modification technique.

1.6.1. Electropolymerization

This technique is based on the MPc containing functional groups which are susceptible of undergoing polymerization under an applied potential. To achieve this, repetitive cycling (using cyclic voltammetry) of a monomer containing solution under a specified potential range is conducted. A successful electropolymerization process will lead to an increase in peak currents and/ or formation of new peaks. The advantages of electropolymerization are better control of film thickness and the rate of film deposition. There are well researched functional groups that can be attached onto the Pc ring and form readily electropolymeric films, these include pyrrole ,[98, 99] aniline,[100, 101] phenols,[102] *etc*.

The following criteria are necessary for effective polymer growth,[103] these include:

- the solvent,
- the type and size of electrode,
- nature of counter ion employed and
- optimum potential window as well as controlled scan rate and the number of cycles.

1.6.2. Self-assembled monolayers (SAMs)

Self-assembled monolayers (SAMs) is a method involving immobilizing sulphur or amine containing molecules onto the metal surfaces usually gold or silver .[104, 105] The formation of SAMs is *via* chemisorption between the electroactive materials and the substrate through covalent bonding.[106] SAM-modified electrodes are relatively simple to prepare, usually it involves dipping of an electrode into a solution containing the active specie. SAMs of CoPcs where the Pc was a *tetra*-benzyl (TBMPc) and *tetra*-dodecylmercapto phthalocyanines (TDMPc) were grown onto different gold electrodes which rendered stable CMEs. The influence of time on the surface packing of these CoPcs revealed different SAMs orientations which in return impacted the surface reactivity of the CMEs. [107] There are several factors governing the successful formation of a SAM onto the substrate surface which include the solvent, the concentration of the sample solution and the SAM formation period. The three common orientations of MPc-SAMs onto a gold electrode surface are largely dictated by steric factors and the positions of the sulphur groups within MPc molecules, see **Fig. 1.7**.

Octopus orientations are typically generated from *octa*- or *tetra*-substituted MPcs where the sulphur atoms occur as aliphatic thioether bridges or within the substituents.[108, 109] The second scenario is initiated by axial ligation followed by covalent attachment of substrate to the axial ligand's sulphur donor atom.[110]

Asymmetric MPcs or symmetrical MPcs with sterically-hindered sulphur containing groups afford SAMs adopting a vertical orientation.[111]

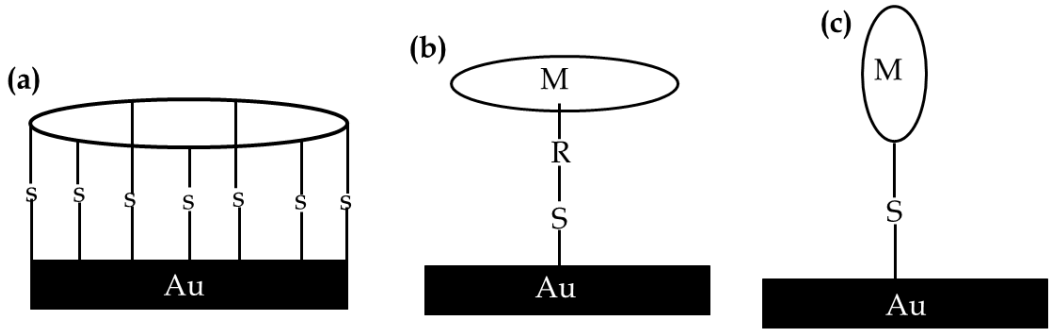

Fig. 1.7: *Possible orientations of SAMs of MPc onto the electrode: (a) octopus, (b) umbrella and (c) vertical.* [111]

1.6.3. Adsorption

Adsorption involves the physical formation of a thin layer of the active specie onto the electrode surface. Adsorption can be implemented in two manners, *viz.* dip-dry or drop-dry. [112, 113] Modifications of a GCE by dropping and drying a suspension of a mixed solution of MWCNTs and CoPc tetraaminophthalocyanine (CoTAPc) against a phased-in dispensation of a solution of MPc followed by MWCNTs on a glassy carbon electrode were comparatively used for *L*-cysteine detection. The latter technique afforded lower detection limits.[113] However, this class of CMEs tends to afford unstable films which are notoriously susceptible to passivation that can be ascribed to the amorphous nature of the thin film and the weak interactions between the MPcs and the electrode.

1.6.4. Electrodeposition

Electrodeposition is achieved by collected conducting repetitive CV scans of a working electrode in a sample solution containing the MPc. Characteristic

electrodeposition CV profiles are depicted by an increase in the peak currents of the redox couple. Indicative to electropolymerization, this technique offers control over the thickness of the film.[114] Although electrodeposition has been widely used for electrode modification for the electrocatalysis of various analytes, it still suffers from poor reproducibility due to weak adhesion of the fabricated thin film to the substrate leading to progressive leaching of MPc molecules.

1.7. References

1. McKeown, N. B., *Phthalocyanine materials: synthesis, structure and function*. Cambridge University Press: 1998.
2. Linstead, R., *Journal of the Chemical Society (Resumed)* **1934**, 1016-1017.
3. Ding, X.; Han, B. H., *Angewandte Chemie* **2015,** *127*, 6636-6639.
4. Idowu, M.; Nyokong, T., *Journal of Photochemistry and Photobiology A: Chemistry* **2008,** *200*, 396-401.
5. Guo, J.; He, H.; Chu, D.; Chen, R., *Electrocatalysis* **2012,** *3*, 252-264.
6. Li, Z.; Liu, B., *Journal of Applied Electrochemistry* **2010,** *40*, 475-483.
7. Ngwenya, V.; Booysen, I. N.; Mambanda, A., *Journal of Coordination Chemistry* **2019,** *72*, 1131-1145.
8. Ponce, I.; Aragonès, A. C.; Darwish, N.; Pla-Vilanova, P.; Oñate, R.; Rezende, M. C.; Zagal, J. H.; Sanz, F.; Pavez, J.; Díez-Pérez, I., *Electrochimica Acta* **2015,** *179*, 611-617.
9. Erdoğmuş, A.; Koca, A.; Uğur, A. L.; Erden, I., *Synthetic metals* **2011,** *161*, 1319-1329.
10. Thimiopoulos, A.; Vogiatzi, A.; Simandiras, E.; Mousdis, G.; Psaroudakis, N., *Inorganica Chimica Acta* **2019,** *488*, 170-181.
11. Farajzadeh, N.; Akyüz, D.; Koca, A.; Koçak, M. B., *Monatshefte für Chemie-Chemical Monthly* **2020,** *151*, 1337-1348.
12. Marquitan, M.; Mark, M. D.; Ernst, A.; Muhs, A.; Herlitze, S.; Ruff, A.; Schuhmann, W., *Journal of Materials Chemistry B* **2020,** *8*, 3631-3639.
13. Kumar, S. P.; Parashuram, L.; Suhas, D.; Krishnaiah, P., *Materials Science for Energy Technologies* **2020,** *3*, 159-166.
14. Fredj, Z.; Ali, M. B.; Abbas, M. N.; Dempsey, E., *Analytical Methods* **2020,** *12* (31), 3883-3891.
15. Sajjan, V. A.; Mohammed, I.; Nemakal, M.; Aralekallu, S.; Kumar, K. H.; Swamy, S.; Sannegowda, L. K., *Journal of Electroanalytical Chemistry* **2019,** *838*, 33-40.
16. Demir, E.; Silah, H.; Uslu, B., *Critical Reviews in Analytical Chemistry* **2020**, 1-37.

17. Erady, V.; Mascarenhas, R. J.; Satpati, A. K.; Bhakta, A. K.; Mekhalif, Z.; Delhalle, J., *Surfaces and Interfaces* **2020,** *19*, 100517.
18. Jilani, B. S.; Malathesh, P.; Mruthyunjayachari, C.; Reddy, K. V., *Materials Chemistry and Physics* **2020,** *239*, 121920.
19. Gorduk, O.; Gorduk, S.; Sahin, Y., *ECS Journal of Solid State Science and Technology* **2020,** *9*, 061003.
20. Mpeta, L. S.; Sen, P.; Nyokong, T., *Journal of Electroanalytical Chemistry* **2020,** *860*, 113896.
21. Brown, M. D.; Schoenfisch, M. H., *Electrochimica acta* **2018,** *273*, 98-104.
22. Lu, S.; Hummel, M.; Kang, S.; Gu, Z., *Journal of The Electrochemical Society* **2020,** *167* (4), 046515.
23. Mpeta, L. S.; Sen, P.; Nyokong, T., *Journal of Electroanalytical Chemistry* **2020,** *866*, 114173.
24. Özen, Ü. E.; Keleş, T.; Bıyıklıoğlu, Z.; Koca, A.; Özkaya, A. R., *Journal of The Electrochemical Society* **2016,** *163*, B673.
25. Kaya, E. N.; Şenocak, A.; Klyamer, D. D.; Demirbaş, E.; Basova, T. V.; Durmuş, M., *Journal of Materials Science: Materials in Electronics* **2019,** *30*, 7543-7551.
26. Raicopol, M. D.; Chira, N. A.; Pandele, A. M.; Hanganu, A.; Ivanov, A. A.; Tecuceanu, V.; Bugean, I. G.; Buica, G.-O., *Sensors and Actuators B: Chemical* **2020,** *313*, 128030.
27. Meenakshi, S.; Pandian, K.; Jayakumari, L.; Inbasekaran, S., *Materials Science and Engineering: C* **2016,** *59*, 136-144.
28. Palanna, M.; Mohammed, I.; Aralekallu, S.; Nemakal, M.; Sannegowda, L. K., *New Journal of Chemistry* **2020,** *44*, 1294-1306.
29. Liu, X.; Sun, C.; Wu, H.; Zhang, Y.; Jiang, J.; Shen, G.; Yu, R., *Electroanalysis* **2010,** *22*, 2110-2116.
30. Fomo, G.; Nwaji, N.; Nyokong, T., *Journal of Electroanalytical Chemistry* **2018,** *813*, 58-66.
31. Koçak, Ç. C.; Nas, A.; Kantekin, H.; Dursun, Z., *Talanta* **2018,** *184*, 452-460.

32. Winiarski, J. P.; de Barros, M. R.; Wecker, G. S.; Nagurniak, G. R.; Parreira, R. L. T.; Affeldt, R. F.; Peralta, R. A.; Jost, C. L., *Journal of Materials Chemistry C* **2020,** *8*, 6839-6850.
33. Reddy, K. V., *Analytica Chimica Acta* **2020,** *1108*, 98-107.
34. Spindola, R. F.; Zanin, H.; Macena, C. S.; Contin, A.; Luz, R. d. C. S.; Damos, F. S., *Journal of Solid State Electrochemistry* **2017,** *21*, 1089-1099.
35. Jilani, B. S.; Mruthyunjayachari, C.; Malathesh, P.; Sharankumar, T.; Reddy, K. V., *Sensors and Actuators B: Chemical* **2019,** *301*, 127078.
36. Deshmukh, M. A.; Shirsat, M. D.; Ramanaviciene, A.; Ramanavicius, A., *Critical Reviews in Analytical Chemistry* **2018,** *48*, 293-304.
37. Oularbi, L.; Turmine, M.; El Rhazi, M., *Synthetic Metals* **2019,** *253*, 1-8.
38. Cheng, K. C.; Chen, P. Y., *Electroanalysis: An International Journal Devoted to Fundamental and Practical Aspects of Electroanalysis* **2008,** *20* (2), 207-210.
39. Saman, N.; Johari, K.; Mat, H., *Microporous and mesoporous materials* **2014,** *194*, 38-45.
40. Malitesta, C.; Di Masi, S.; Mazzotta, E., *Frontiers in chemistry* **2017,** *5*, 47.
41. Kondor, A. C.; Jakab, G.; Vancsik, A.; Filep, T.; Szeberényi, J.; Szabó, L.; Maász, G.; Ferincz, Á.; Dobosy, P.; Szalai, Z., *Environmental Pollution* **2020,** *265*, 114893.
42. Madikizela, L. M.; Ncube, S.; Chimuka, L., *Journal of environmental management* **2020,** *253*, 109741.
43. Matongo, S.; Birungi, G.; Moodley, B.; Ndungu, P., *Chemosphere* **2015,** *134*, 133-140.
44. Wood, T. P.; Duvenage, C. S.; Rohwer, E., *Environmental Pollution* **2015,** *199*, 235-243.
45. Abafe, O. A.; Späth, J.; Fick, J.; Jansson, S.; Buckley, C.; Stark, A.; Pietruschka, B.; Martincigh, B. S., *Chemosphere* **2018,** *200*, 660-670.
46. Tons of toxic mercury waste remains uncleared in KZN|eNCA. https://www.enca.com/news/tons-toxic-mercury-waste-remains-uncleared-kzn (accessed February 04, 2021).
47. Jiang, J.; Briedé, J. J.; Jennen, D. G.; Van Summeren, A.; Saritas-Brauers, K.; Schaart, G.; Kleinjans, J. C.; de Kok, T. M., *Toxicology letters* **2015,** *234*, 139-150.

48. Mazer, M.; Perrone, J., *Journal of Medical Toxicology* **2008,** *4*, 2-6.
49. Monteiro, D. A.; Taylor, E. W.; McKenzie, D. J.; Rantin, F. T.; Kalinin, A. L., *Ecotoxicology* **2020**, 1-14.
50. Marumoto, M.; Sakamoto, M.; Marumoto, K.; Tsuruta, S.; Komohara, Y., *Acta Histochemica et Cytochemica* **2020**, 20-00009.
51. Yildiz, M.; Adrovic, A.; Gurup, A.; Yilmaz, E. K.; Ozer, Y.; Koker, O.; Sahin, S.; Kiykim, E.; Canpolat, N.; Barut, K., *Rheumatology international* **2020,** *40*, 1333-1342.
52. Sharma, A. M.; Li, Y.; Novalen, M.; Hayes, M. A.; Uetrecht, J., *Chemical research in toxicology* **2012,** *25* (8), 1708-1719.
53. National Primary Drinking Water Regulations | Ground Water and Drinking Water | United States Environmental Protection Agency. https://www.epa.gov/ground-water-and-drinking-water/national-primary-drinking-water-regulations (accessed October 7, 2020).
54. Fukuda, T.; Ishiguro, T.; Kobayashi, N., *Tetrahedron letters* **2005,** *46*, 2907-2909.
55. Özçeşmeci, M.; Özçeşmeci, İ.; Sorar, İ.; Hamuryudan, E., *Inorganic Chemistry Communications* **2017,** *86*, 209-212.
56. Arıcan, D.; Arıcı, M.; Uğur, A. L.; Erdoğmuş, A.; Koca, A., *Electrochimica Acta* **2013,** *106*, 541-555.
57. Özçeşmeci, M.; Sorar, İ.; Hamuryudan, E., *Journal of Porphyrins and Phthalocyanines* **2019,** *23*, 136-141.
58. Farajzadeh, N.; Akyüz, D.; Koca, A.; Kocak, M. B., *Polyhedron* **2020,** *177*, 114264.
59. Mwanza, D.; Khene, S.; Mashazi, P., *Polyhedron* **2017,** *134*, 263-274.
60. Özçeşmeci, İ.; Koca, A.; Gül, A., *Electrochimica acta* **2011,** *56*, 5102-5114.
61. Chauke, V. P.; Arslanoglu, Y.; Nyokong, T., *Polyhedron* **2011,** *30*, 2132-2139.
62. Kılıçaslan, M. B.; Koca, A., *Dyes and Pigments* **2014,** *103*, 95-105.
63. Kurt, Ö.; Koca, A.; Gül, A.; Koçak, M. B., *Synthetic Metals* **2015,** *206*, 72-83.
64. Peterson, M.; Hunt, C.; Wang, Z.; Heinrich, S. E.; Wu, G.; Ménard, G., *Dalton Transactions* **2020**.
65. Akçay, H. T.; Bayrak, R.; Demirbaş, Ü.; Koca, A.; Kantekin, H.; Değirmencioğlu, I., *Dyes and Pigments* **2013,** *96*, 483-494.

66. Sevim, A. M.; Yenilmez, H. Y.; Aydemir, M.; Koca, A.; Bayır, Z. A., *Electrochimica Acta* **2014,** *137*, 602-615.
67. Köse, G. G.; Karaoğlan, G. K.; Işık, S. N.; Akyüz, D.; Koca, A., *Synthetic Metals* **2020,** *264*, 116386.
68. Feridun, S. G.; Orman, E. B.; Salan, Ü.; Özkaya, A. R.; Bulut, M., *Dyes and Pigments* **2019,** *160*, 315-327.
69. Guo, J.-J.; Bai, Z.-C.; Meng, X.-F.; Sun, M.-M.; Song, J.-H.; Shen, Z.-S.; Ma, N.; Chen, Z.-L.; Zhang, F., *Solar Energy* **2017,** *155*, 121-129.
70. Xu, T.; Ni, D.; Chen, X.; Wu, F.; Ge, P.; Lu, W.; Hu, H.; Zhu, Z.; Chen, W., *Journal of Hazardous Materials* **2016,** *317*, 17-26.
71. Ebele, A. J.; Oluseyi, T.; Drage, D. S.; Harrad, S.; Abdallah, M. A.-E., *Emerging Contaminants* **2020,** *6*, 124-132.
72. Gómez-Ramírez, P.; Blanco, G.; García-Fernández, A. J., *International Journal of Environmental Research and Public Health* **2020,** *17*, 4058.
73. Doğan, B.; Elik, A.; Altunay, N., *Microchemical Journal* **2020,** *154*, 104645.
74. Orooji, Y.; Irani-nezhad, M. H.; Hassandoost, R.; Khataee, A.; Pouran, S. R.; Joo, S. W., *Spectrochimica Acta Part A: Molecular and Biomolecular Spectroscopy* **2020**, 118272.
75. Xu, H.; Xiao, J.; Yan, L.; Zhu, L.; Liu, B., *Journal of Electroanalytical Chemistry* **2016,** *779*, 92-98.
76. Liu, J.; Wang, J.; Wang, T.; Li, D.; Xi, F.; Wang, J.; Wang, E., *Biosensors and Bioelectronics* **2015,** *65*, 281-286.
77. Deshmukh, R.; Prusty, A. K.; Roy, U.; Bhand, S., *Analyst* **2020,** *145*, 2267-2278.
78. Ghazizadeh, E.; Neshastehriz, A., *Analytica Chimica Acta* **2020**.
79. Verlicchi, P.; Grillini, V., *Water* **2020,** *12*, 305.
80. Cinti, S.; Neagu, D.; Carbone, M.; Cacciotti, I.; Moscone, D.; Arduini, F., *Electrochimica Acta* **2016,** *188*, 574-581.
81. Bojdi, M. K.; Behbahani, M.; Omidi, F.; Hesam, G., *New Journal of Chemistry* **2016,** *40*, 4519-4527.
82. Lu, M.; Deng, Y.; Luo, Y.; Lv, J.; Li, T.; Xu, J.; Chen, S.-W.; Wang, J., *Analytical chemistry* **2018,** *91*, 888-895.

83. Tijani, J. O.; Fatoba, O. O.; Babajide, O. O.; Petrik, L. F., *Environmental chemistry letters* **2016,** *14*, 27-49.
84. Fu, R.; Shen, M.; Ding, Y.; Li, M.; Li, L.; Ren, Z.; Wu, Q., *Electroanalysis* **2020,** *32*, 978-985.
85. Massumi, S.; Ahmadi, E.; Akbari, A.; Gholivand, M. B., *Journal of Electroanalytical Chemistry* **2020,** *876*, 114508.
86. Zhou, T.; Shao, R.; Chen, S.; He, X.; Qiao, J.; Zhang, J., *Journal of Power Sources* **2015,** *293*, 946-975.
87. Haque, M.; Sulong, A.; Majlan, E.; Loh, K.; Husaini, T.; Rosli, R., *International Journal Electrochemical Science* **2019,** *14*, 371-386.
88. Karim, N.; Kamarudin, S.; Loh, K., *Energy Conversion and Management* **2017,** *145*, 293-307.
89. Pu, L.; Liu, D.; Li, K.; Wang, J.; Yang, T.; Ge, B.; Liu, Z., *International Journal of Hydrogen Energy* **2017,** *42*, 14253-14263.
90. Li, W.; Amiinu, I. S.; Zhang, B.; Zhang, C.; Zhang, Z.; Zhu, J.; Liu, J.; Pu, Z.; Kou, Z.; Mu, S., *Carbon* **2018,** *139*, 1144-1151.
91. Jasinski, R., *Nature* **1964,** *201*, 1212-1213.
92. Zagal, J. H., *Coordination Chemistry Reviews* **1992,** *119*, 89-136.
93. Chu, D.; Jiang, R., *Solid State Ionics* **2002,** *148*, 591-599.
94. Koç, I.; Özer, M.; Özkaya, A.; Bekaroğlu, Ö., *Dalton Transactions* **2009**, 6368-6376.
95. Xu, L.; Tang, S.; Wang, K.; Ma, X.; Niu, J., *Chemosphere* **2020,** *241*, 125058.
96. Liu, Q.; Bai, X.; Su, X.; Huang, B.; Wang, B.; Zhang, X.; Ruan, X.; Cao, W.; Xu, Y.; Qian, G., *Journal of Cleaner Production* **2020,** *244*, 118890.
97. Liu, M.; Xia, H.; Lu, W.; Xu, T.; Zhu, Z.; Chen, W., *Journal of Applied Electrochemistry* **2016,** *46*, 583-592.
98. Shrivastava, S.; Kumar, A.; Verma, N.; Chen, B. Y.; Chang, C. T., *Electroanalysis* **2020**.
99. Jadi, S. B.; El Jaouhari, A.; Aouzal, Z.; El Guerraf, A.; Bouabdallaoui, M.; Wang, R.; Bazzaoui, E.; Bazzaoui, M., *Materials Today: Proceedings* **2020,** *22*, 52-56.
100. Chu, T.-X.; Vu, V.-P.; Tran, H.-T.; Tran, T.-L.; Tran, Q.-T.; Le Manh, T., *Journal of The Electrochemical Society* **2020,** *167*, 027527.

101. Hassan, A. A.; Abdulazeez, I.; Salawu, O. A.; Al-Betar, A. R., *SN Applied Sciences* **2020,** *2*, 1-8.
102. Kiss, L.; Kovács, F.; Li, H.; Kiss, A.; Kunsági-Máté, S., *Chemical Physics Letters* **2020**, 137642.
103. John, R.; Wallace, G., *Journal of electroanalytical chemistry and interfacial electrochemistry* **1991,** *306*, 157-167.
104. Arvand, M.; Farahpour, M.; Ardaki, M. S., *Talanta* **2018,** *176*, 92-101.
105. Sekine, T.; Sato, J.; Takeda, Y.; Kumaki, D.; Tokito, S., *ACS Applied Materials & Interfaces* **2018,** *10*, 16210-16215.
106. Matemadombo, F.; Durmuş, M.; Togo, C.; Limson, J.; Nyokong, T., *Electrochimica Acta* **2009,** *54* (23), 5557-5565.
107. Agboola, B.; Westbroek, P.; Ozoemena, K. I.; Nyokong, T., *Electrochemistry Communications* **2007,** *9*, 310-316.
108. Ozoemena, K. I.; Nyokong, T.; Westbroek, P., *Electroanalysis: An International Journal Devoted to Fundamental and Practical Aspects of Electroanalysis* **2003,** *15*, 1762-1770.
109. Ozoemena, K.; Westbroek, P.; Nyokong, T., *Electrochemistry Communications* **2001,** *3*, 529-534.
110. Ozoemena, K. I.; Nyokong, T., *Electrochimica Acta* **2006,** *51*, 2669-2677.
111. Nyokong, T.; Bedioui, F., *Journal of Porphyrins and Phthalocyanines* **2006,** *10*, 1101-1115.
112. Zhang, J.; Tse, Y.-H.; Pietro, W. J.; Lever, A., *Journal of Electroanalytical Chemistry* **1996,** *406*, 203-211.
113. Nyoni, S.; Mugadza, T.; Nyokong, T., *Electrochimica Acta* **2014,** *128*, 32-40.
114. Agboola, B.; Nyokong, T., *Analytica chimica Acta* **2007,** *587*, 116-123.

Chapter 2

Materials and Instrumentation

2.1 Materials

The synthetic organic and inorganic precursors used in this research study were acquired from Sigma-Aldrich and used without any further purification, see **Table 2.1**. The non-nucleophilic basic catalyst, 1, 8-diazabicyclo[5.4.0]undec-7-ene (DBU) and electrochemical supporting electrolyte grade, tetrabutylammonium tetrafluoroborate ($TBABF_4$) were purchased from the same supplier. The monomer, 3-hexylthiophene and the Nafion resin solution (5%) used in the electrode modification techniques, were procured from Sigma-Aldrich.

All organic solvents used in the synthesis and purification processes, phosphorus pentoxide (P_2O_5), molecular sieves (4 Å), silicon dioxide (silica) for column chromatography and silica plates for thin layer chromatography were all procured from Merck SA. Dimethylformamide (DMF) used in the synthesis was firstly distilled and subsequently stored over molecular sieves.

Aluminium oxide (alumina) for polishing the working electrodes was supplied by Metrohm. Carboxylic acid functionalized MWCNTs, phosphate buffer tablets as well as the analytical grade analytes were obtained from Sigma-Aldrich and are also listed in **Table 2.1**. The following derivatized phthalonitriles *viz* 4-(flavone-3-oxy)phthalonitrile, 4-(2-(benzoxazol-2-yl)phenoxy)phthalonitrile, 4-(furan-2-methylthio)phthalonitrile, 4-(benzothiazole-2-methoxy)phthalonitrile, 4-(4-trifluoromethyl)-coumarin-7-oxy) phthalonitrile as well as their corresponding CoPcs, *β*-tetra(3-oxyflavonephthalocyaninato)Cobalt(II) (*viz.* CoPc-flav), *β*-tetra(2-(2-oxyphenyl)benzoxazolephthalocyaninato)Cobalt(II) (*viz.* CoPc-bo), *β*-tetra(2-furanmethylthiophthalocyaninato)Cobalt(II) (*viz*. CoPc-fur) and *β*-tetra(7-oxy-4-

trifluoromethylcoumarinphthalocyaninato)Cobalt(II) (*viz.* CoPc-cou) were synthesized and confirmed as reported in literature.[1-4] The ultrapure water was attained from the ElgaPure ultra system.

Table 2.1: *List of commercially attained chemicals and their corresponding percentage purities.*

Chemicals	Purity
4-Nitrophthalonitrile	99%
Potassium Carbonate	99.5%
Potassium Ferricyanide	≥ 99%
Sodium Chloride	≥ 99.5%
3-Hydroxyflavone	≥ 98%
3-hexylthiophene	≥ 99%
Lithium Perchlorate	99.99
2-hydroxymethylbenzothiazole	97%
Cobalt(II) chloride	97%
1,8-Diazabicyclo[5.4.0] undec-7-ene	98%
Tetrabutylammonium tetrafluoroborate ($TBABF_4$)	99%
Dopamine hydrochloride	98%
Cysteine	≥ 98.5%
Metronidazole	97%
Ibuprofen	98%
Uric acid	≥ 99%
Ascorbic acid	99%
Paracetamol (Acetaminophen)	≥ 99%
Nevirapine	≥ 98%
Mercury(II) sulfate	≥ 99%
Lead(II) nitrate	≥ 99%
Zinc(II) acetate	≥ 99%

2.2 Instrumentation

To confirm the identity and purity of the derivatized phthalonitrile and the CoPcs, their NMR- (for the derivatized phthalonitrile only), IR and TOF-MS spectra were acquired, and their data was also compared with that of previously reported. The data were collected using the following spectrometers, a Bruker Alpha FTIR spectrometer, equipped with an ATR platinum Diamond 1 reflectance accessory, a 400 MHz Bruker NMR spectrometer equipped with an auto-sampler and a Waters Micromass LCT Premier mass spectrometer, equipped with an electrospray ionization (ESI) source and a time-of-flight (TOF) mass analyzer. An organic elemental analyser using a CHNS-O Flash 2000 was used for elemental analysis.

Electrochemical experiments were conducted out using an Autolab PGSTAT 302N electrochemical workstation equipped with an Electrochemical Impedance Spectroscopy (EIS) module and the Autolab NOVA 1.7 software package. Rotating disk electrode (RDE) voltammograms were collected by ramping the potential linearly over a defined range while rotating the work electrode at controlled speeds using an Autolab RDE-2 equipped with a motor controller whereas diffusion-controlled experiments were achieved using chronoamperometry. During these experiments, a three-electrode voltammetric cell including a glassy carbon, gold or platinum working electrode, Ag|AgCl wire as a pseudo reference electrode and Pt counter electrode were used. The pH measurements were done using a Metrohm 827 pH meter (Switzerland) after calibration with standard buffer solutions of pH values of 4, 7, and 10. The squarewave voltammetry settings includes a step potential of 4 mV, a frequency of 25 Hz and an amplitude of 20 mV. EIS data were fitted using the imbedded algorithms within the Autolab NOVA 1.7 software package.

Transmission electron microscopy (TEM) were done using a JEOL 1400 microscope. TEM samples were prepared by dispersing the samples in ethanol and allowing these samples to dry on a glass slit. Surface imagery of bare and modified gold-coated glass were acquired using a Zeiss EVO LS15 scanning electron

microscope operating under high vacuum. Elemental composition was done with an Oxford X-MAX EDX detector under high vacuum with an accelerating voltage of 20 kV.

2.3 References

1. Chohan, S.; Booysen, I. N.; Mambanda, A., *Polyhedron* **2015,** *102*, 284-292.
2. Chohan, S.; Booysen, I. N.; Mambanda, A.; Akerman, M. P., *Inorganica Chimica Acta* **2016,** *447*, 183-191.
3. Chohan, S.; Booysen, I. N.; Mambanda, A.; Akerman, M. P., *Journal of Coordination Chemistry* **2015,** *68*, 1829-1846.
4. Kantize, K.; Ngwenya, V.; Booysen, I. N.; Mambanda, A., *Polyhedron* **2021**, 115235.

CHAPTER THREE

Electrochemical sensing of acetaminophen using nanocomposites comprised of cobalt(II) phthalocyanines and multiwalled carbon nanotubes

3.1. Introduction

Rapid and accurate screening of organopharmaceuticals in water reservoirs are of utmost importance as elevated concentrations of these emerging pollutants can have detrimental consequences to animal and human health.[1] Studies conducted in developing countries reveal that pollution of surface water by pharmaceutical residues has been a growing environmental problem as a result of rapid growing populations in most urban settlements which is usually not matched by advanced waste handling and disposal practices.[2, 3] Moreover, the monitoring of water quality in rural areas is challenging since analytical laboratories are often non-existent, poorly equipped or lack the necessary skilled workforce to operate sophisticated instrumentation.[4]

A recent study conducted on water samples from the Msunduzi river in KwaZulu-Natal of the Republic of South Africa showed that widespread contamination of pharmaceuticals has occurred.[5] Among these pharmaceuticals include Acetaminophen, [N-acetyl-p-aminophenol], APAP which is an over-the-counter drug commonly used for analgesic and antipyretic therapy. It inhibits the synthesis of prostaglandin, thus relieving the pain associated with fever and inflammation of tissues.[6] At therapeutic doses, APAP is metabolized mainly through glucuronidation and sulfation to metabolites which are excreted as urinary salts. However, chronic intake of over therapeutic doses, can lead to hepatotoxicity and nephrotoxicity in mammals.[7, 8] Due to its non-prescriptive access, concentration of

APAP in domestic and medical wastes are high and its contamination in urban surface water resources has become an emerging water contaminant problem globally.[9-12] Furthermore, increased concentration levels of APAP in water directly affect the eco-balance and -sustainability of the affected aquatic ecosystems while portable water systems heavily contaminated with APAP can lead to organ failure.[13]

Analytical techniques including spectrophotometry,[14, 15] high performance liquid chromatography,[16,17]luminescence[18] and titrimetric methods[19] have traditionally been used to quantify APAP. However, these techniques are either time consuming or demand tedious extraction processes prior to detection which is very inconvenient in routine APAP analysis. As APAP is an electroactive compound, it can potentially be detected and quantified by functional electroanalytical sensors. Generally, electrochemical sensing offers faster analysis than the aforementioned conventional techniques and electrochemical sensors can be miniaturized for real-time analysis within the field.[20] Imperative prerequisites of functional electrochemical detectors include reproducibility, robustness, selectivity and sensitivity to ensure reliable data capturing and processing .[21]

Chemically modified electrodes (CMEs) have been widely used as electrocatalytic detectors of APAP as the electron mediating thin films addresses the poor recognition capabilities of the analyte in complex matrixes as well as minimizes passivation by oxidation by-products.[22] More specifically, most heterogeneous catalysts used for electro-oxidation of APAP have consisted of carbonaceous nanomaterial immobilized on various conductive substrates.[23-26] In this research study, the efficient electrocatalysis of APAP is reported using glassy carbon electrodes (GCEs) modified with nanoconjugates comprised of carboxylic acid functionalized multiwalled carbon nanotubes (*f*-MWCNTs) and cobalt(II) phthalocyanines (CoPcs) tetrasubstituted flavone (flav) or benzoxazole (bo) moieties.

CoPcs are well known for their molecular recognition capabilities which are promoted by their metal- and ligand based redox properties while the latter can be readily influenced by the stereo-electronic properties of the substituents.[27-29] The motivation behind the substituent choices, flavone and benzoxazole was to address the traditionally poor selectivity of MPc-based voltammetric sensors since these substituents have been already imbedded in various other sensors.[30, 31] In addition, the inclusion of the MWCNTs within CoPc-MWCNTs hybrids, have shown to lead to enhanced electrical conductivities under applied potentials due to the sp^2-hybridized network structure of MWCNTs.[32-34]

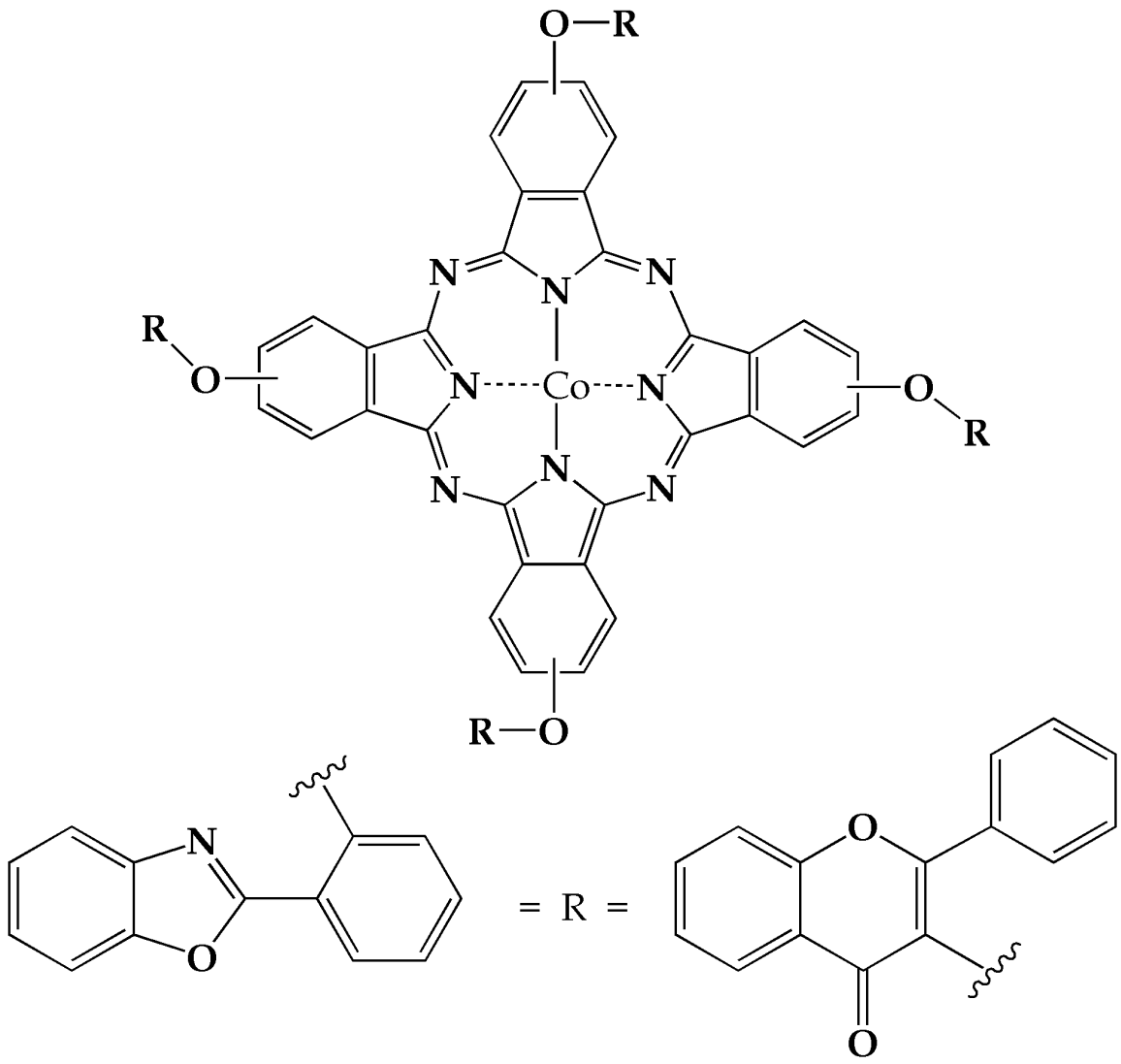

Fig. 3.1: *Generic structure of the CoPcs tetrasubstituted with 2-methoxy(flavone/phenylbenzoxazole) moieties.*

3.2. Experimental

3.2.1. Materials

The synthetic precursors: 4-nitrophthalonitrile, 3-hydroxyflavone, 2-(2-hydroxyphenyl) benzoxazole, cobalt (II) chloride and carboxylic acid functionalized multiwalled carbon nanotubes (*f*-MWCNTs) were purchased from Sigma-Aldrich. The catalysts: 1,8-diazabicyclo [*5.4.0*] undec-7-ene (DBU), potassium carbonate and electrochemical grade tetrabutylammonium tetrafluoroborate ($TBABF_4$) as well as analytical grade phosphate buffer saline tablets, acetaminophen (APAP), metronidazole (MTZ), ibuprofen (IBU), dopamine (DA) and ascorbic acid (AA) were procured from the same supplier. These chemicals were used without any purification.

Organic solvents, phosphorous pentoxide, molecular sieves (4 Å), silica dioxide for column chromatography and silica plates for thin layer chromatography were purchased from Merck SA. Dimethylformamide (DMF) was dried and stored over molecular sieves while ultrapure water was obtained from an Elga Purelab Ultra system. The derivatized phthalonitriles, 4-(flavone-3-oxy)phthalonitrile and 4-(2-(benzoxazol-2-yl)phenoxy)phthalonitrile as well as the corresponding CoPcs, *β*-tetra(3-oxyflavone/2-(2-oxyphenyl)benzoxazole)pthalocyanines (*viz.* CoPc-flav or CoPc-bo) were synthesized according to previously published experimental procedures.[34] The isolated metal complexes were stored over P_2O_5.

3.2.2. General electrode modification techniques

The bare GCE was polished on a Buehler-felt pad using 0.5 μm alumina paste and washed with ultrapure water. Thereafter, the electrode was sonicated in an ultrasonic bath for 5 minutes in a PBS pH 7.4 buffer solution and rinsed again with ultrapure water. As previously reported, the respective 1 mM CoPcs (*i.e.* CoPc-flav or

CoPc-bo) in dried DMF containing 0.1 M of $TBABF_4$, were electrodeposited onto the GCE surfaces which afforded the modified electrodes, CoPc-flav and CoPc-bo GCEs.[34]

Furthermore, the CoPc-X-*f*-MWCNTs (X = flav or bo) conjugates were fabricated by preparing a suspension made up of 1 mg of carboxylic acid functionalized MWCNTs, 0.5 mg of the individual CoPc in deaerated DMF. Afterwards, the suspensions were ultrasonicated for 30 minutes and drop-casted on the surfaces of separate GCEs which were dried at 80 ^{o}C for 24 hrs. This rendered the respective CMEs denoted as CoPc-flav-*f*-MWCNTs- and CoPc-bo-*f*-MWCNTs GCEs, see **Fig. 3.2**. Indicatively, the *f*-MWCNTs GCE was fabricated by the drop-dry method.

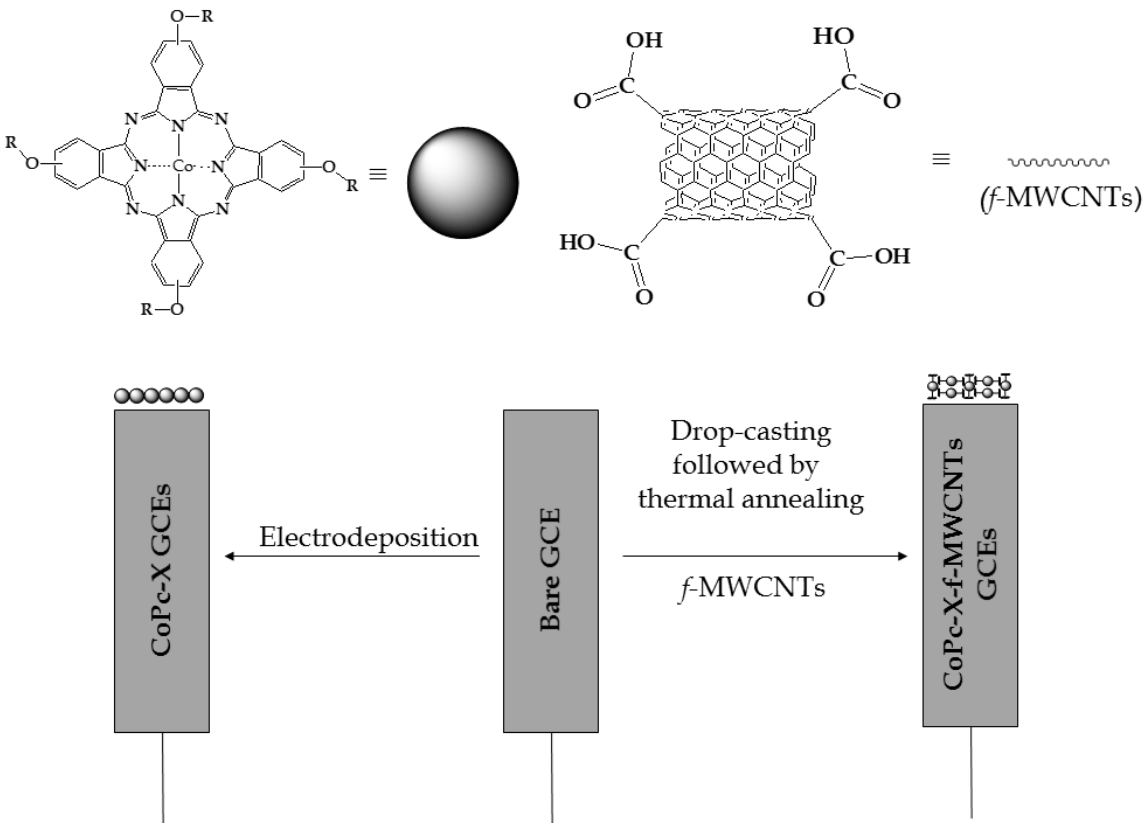

Fig. 3.2: *Stepwise modification of a bare GCE by the respective CoPc-X-f-MWCNTs (X = flav or bo) nanoconjugates.*

3.3. Results and Discussion

3.3.1. Fabrication and characterization of CoPc-X-f-MWCNTs conjugates

Nanofabrication of the respective CoPc-X-*f*-MWCNTs were achieved by ultrasonicating the respective CoPcs and *f*-MWCNTs in dry DMF followed by drying the mixture at an elevated temperature. TEM images were generated from samples of the respective CoPcs, *f*-MWCNTs and CoPc-X-*f*-MWCNTs which are shown in **Figs. 3.3** and **3.4**. Significant aggregation was observed in the TEM images of the CoPcs which is characteristic of $\pi - \pi$ stacking interactions between the planar N_4-metallocyclic molecules while well-dispersed nanoparticles could be observed in the TEM images of the *f*-MWCNTs. Interestingly, the TEM images of the nanoconjugates indicates nodal points along the surfaces of the *f*-MWCNTs, suggesting chemical interactions between its *f*-MWCNTs and CoPc constituents.

A nanocomposite, CoPc-*f*-MWCNTs synthesized in a similar manner (as CoPc-X-*f*-MWCNTs) from the conjugation of an unsubstituted CoPc and *f*-MWCNTs, indicated that the *f*-MWCNTs chemically interact *via* bonding of its carboxylic acids group with the metal and nitrogen atoms of the CoPc. In addition, secondary interactions occurred in the form of *pi*-stacking between the CoPc and MWCNTs constituents.[35] Overlay solid state IR spectra of *f*-MWCNTs and its CoPc-X hybrids distinctively showed common broad v(O-H) [3485 cm^{-1} for CoPc-flav-*f*-MWCNTs and 3399 cm^{-1} for CoPc-bo-*f*-MWCNTs] and intense v(C=O) [1657 cm^{-1} for CoPc-flav-*f*-MWCNTs and 1646 cm^{-1} for CoPc-bo-*f*-MWCNTs], see **Fig. 3.5**. This indicated chemical bonding had occurred between the carboxylic acid groups of the MWCNTs and the metallocyclic complexes, respectively.

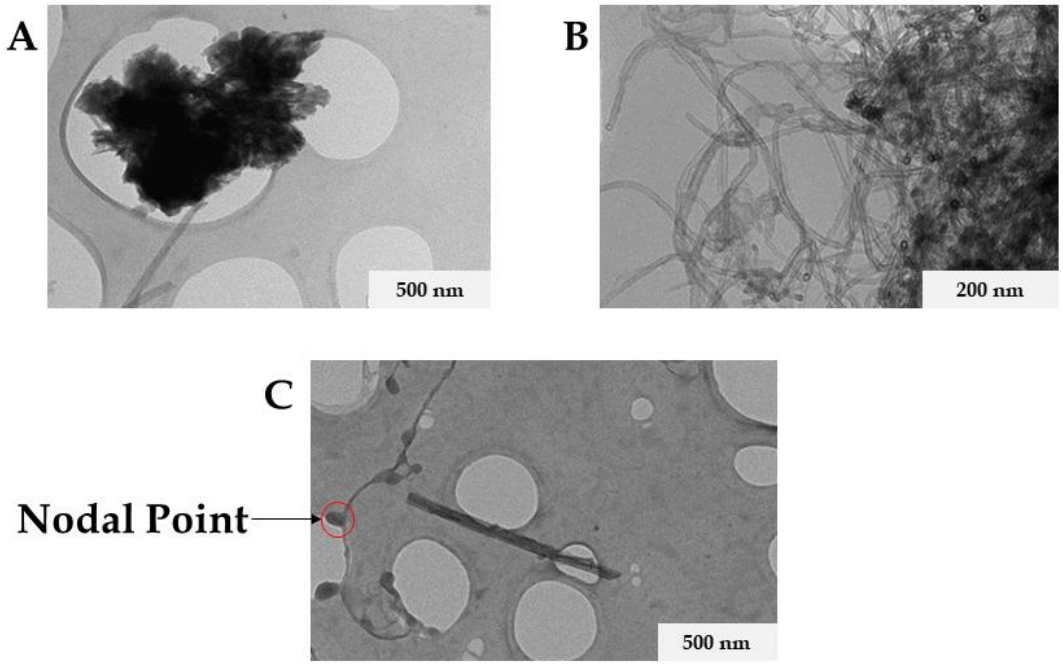

Fig. 3.3: *TEM images of (**A**) CoPc-flav, (**B**) f-MWCNTs and (**C**) CoPc-flav-f-MWCNTs.*

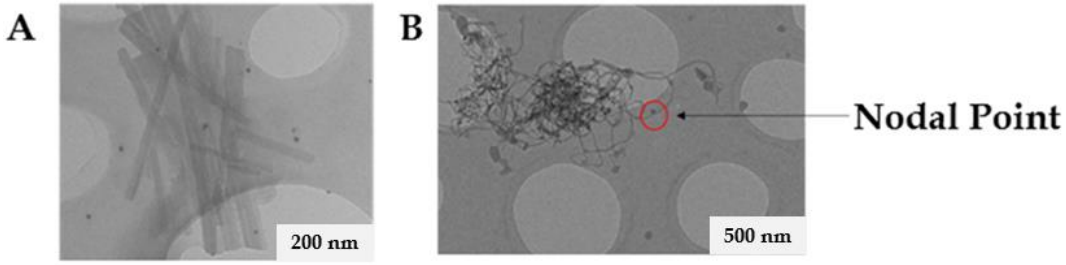

Fig. 3.4: *TEM images of (**A**) CoPc-bo and (**B**) CoPc-bo-f-MWCNTs*

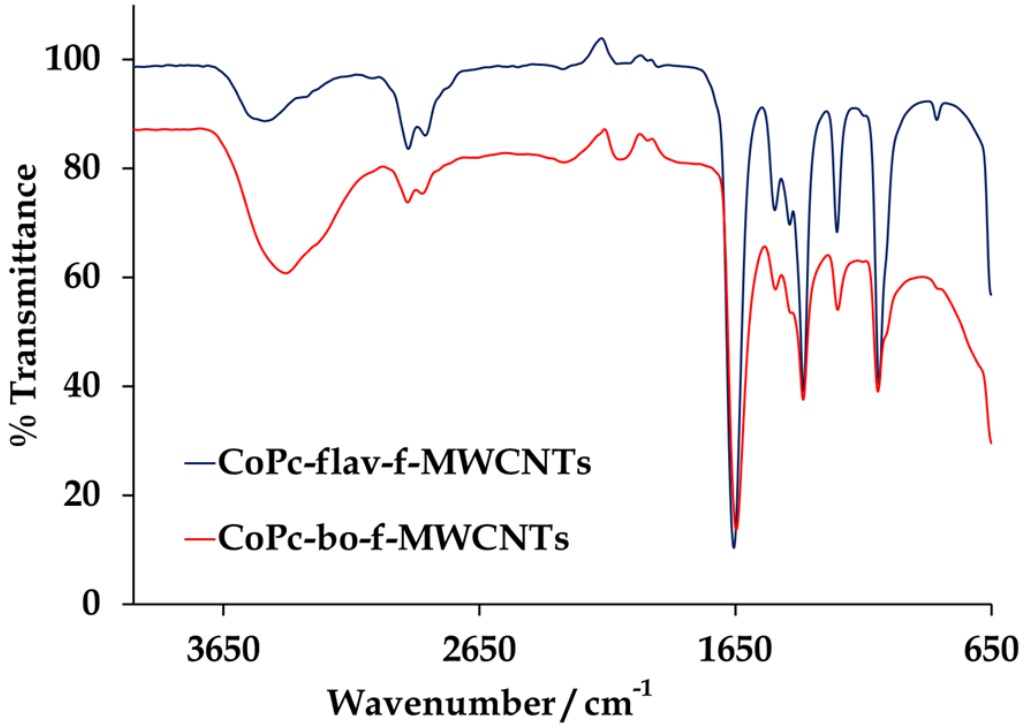

Fig. 3.5: *Overlay IR spectra of f-MWCNTs, CoPc-flav-f-MWCNTs and CoPc-bo-f-MWCNTs.*

3.3.2. Electrocatalytic responses of the CMEs

The electrochemical sensing performances of the CMEs depends on their capabilities of facilitating the redox responses during the oxidation and reduction of the analyte, APAP, see **Figs. 3.6** and **3.7**. The unmodified and CoPc-X GCEs induced minute redox peak potentials which indicates that the electrodeposited CoPcs exhibited poor electron-mediating capabilities during the electrocatalysis of APAP, see **Table 1**. Furthermore, sluggish electron-electron transfer kinetics of the CoPc-bo GCE was noted based on its wider ΔE value oppose to those obtained for the bare and CoPc-flav GCEs. Despite the fact that the *f*-MWCNTs GCE afforded higher catalytic currents, the oxidation of APAP at the surface of this electrode occurred at an anodic peak potential (E_{pa}) of 0.66 V, while the cathodic peak potential (E_{pc}) was found at 0.20 V. The higher oxidation peak potential attained using the *f*-MWCNTs GCE was indicative of slow electron transfer kinetics.

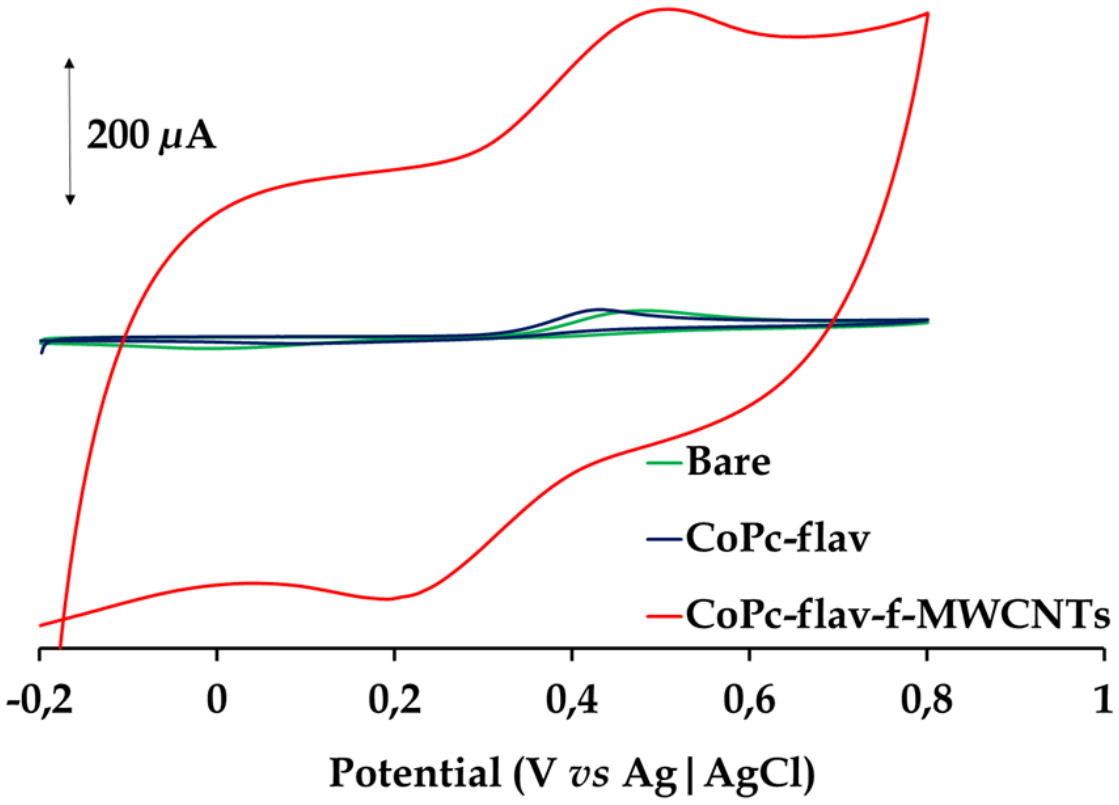

Fig. 3.6: *CVs conducted in 1.0 mM of acetaminophen (APAP) prepared in 0.01 M PBS buffer using the CoPc-flav-f-MWCNTs-, CoPc-flav- and bare GCEs.*

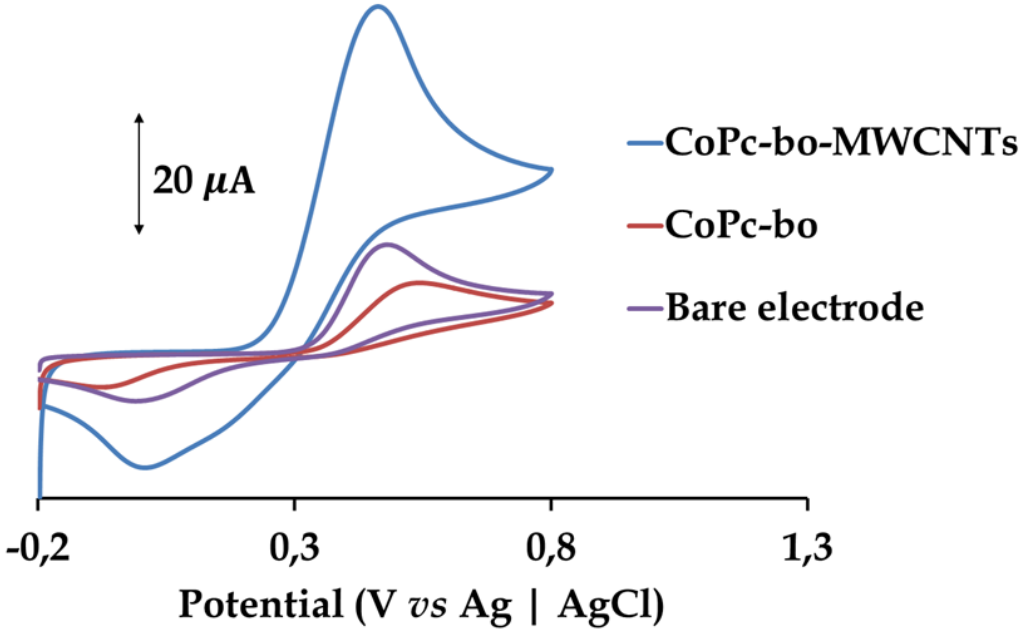

Fig. 3.7: *CVs of 1.0 mM of acetaminophen (APAP) (in 0.01 M PBS buffer, pH 7.4) using the CoPc-bo-f-MWCNTs-, CoPc-bo and bare GCEs.*

In contrast, upon using the CoPc-flav-*f*-MWCNTs GCE, oxidation- and reduction peak potentials of APAP at 0.50 V (E_{pa}) and 0.20 V (E_{pc}) were attained. In addition, higher oxidation current intensities were observed when using the CoPc-X-*f*-MWCNTs GCEs which were higher than the I_p values recorded with the bare GCE. Furthermore, these CMEs portrayed superior electron transfer rates as per smaller ΔE values than the APAP peak-to-peak potential separation obtained using the *f*-MWCNTs GCE. Hence, the synergetic electron-mediating effects of the CoPcs and the *f*-MWCNTs (in CoPc-X-*f*-MWCNTs) were clearly apparent during the reversible APAP redox reactions as illustrated below:

Table 1: *APAP Redox potentials (in V vs Ag|AgCl) attained using the different electrodes.*

Electrode	**E_{pa}**	**E_{pc}**	**ΔE**
Bare GCE	0.48	0.00	0.48
CoPc-flav	0.43	0.08	0.35
CoPc-bo	0.53	-0.07	0.60
f-MWCNTs	0.66	0.20	0.46
CoPc-flav-*f*-MWCNTs	0.50	0.20	0.30
CoPc-bo-*f*-MWCNTs	0.46	0.01	0.45

It is evident that the interconversion between APAP and its oxidized derivative, *N*-acetyl-*p*-benzoquinone (NAPQI) is largely electrocatalysed by the metal-based redox couple as the APAP peak potentials were in the proximity of the potential window [-0.92 V to +0.3 V *vs* Ag|AgCl at 100 mV/s] where the Co^{III}/Co^{II} redox couple occurs in pH 7 buffered aqueous solutions, see **scheme 3.1**.[34] In light of the dominating electrocatalytic performances of the working electrodes modified with the nanoconjugate thin films over the MPc-electrodeposited GCEs, the remaining electrochemical studies were done using the CoPc-X-flav GCEs.

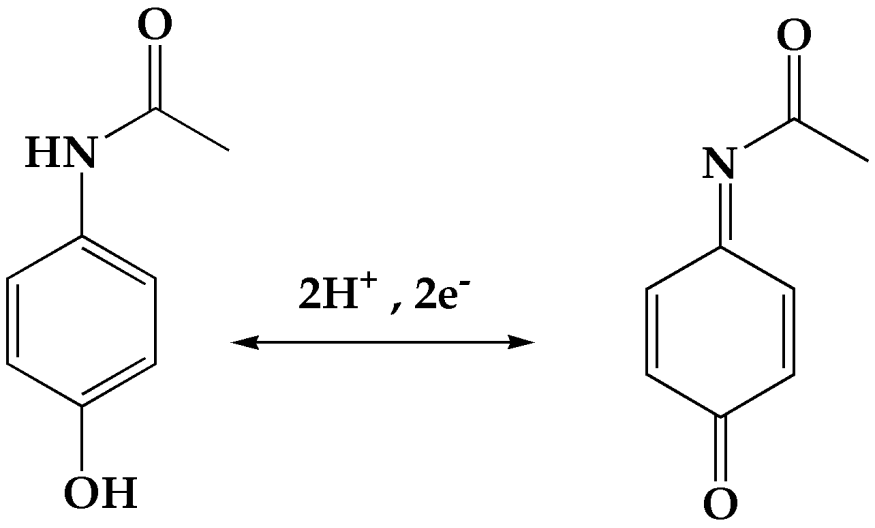

Scheme 3.1: *Redox interconversion mechanism of Paracetamol*

The effect of scan rate on the electrochemical redox reactions of APAP was investigated using a 1 mM of APAP in a PBS buffer at incrementing scan rates, see **Figs. 3.8** and **3.9**. Subsequently, linear relationships were attained between the redox peak currents and the scan rates which affirmed that the analyte transports *via* diffusion to the interface of the modified GCEs. The linear regression equations were as follows:

$$I_{pa}(\mu A) = 4E^{-06}v + 9E^{-05} \quad (R^2\text{=}0.992) \qquad (\mathbf{1})$$

$$I_{pc}(\mu A) = -3E^{-06}v - 3E^{-05} \quad (R^2\text{=}0.997) \qquad (\mathbf{2})$$

Interestingly, the CoPc-X-*f*-MWCNTs GCEs illustrated no-observable propensity to undergo surface fouling given by its high-level of reproducibility between CV runs. Furthermore, Tafel slopes were obtained from the individual plots of oxidation peak potentials against the scan rates, as defined by equation (**3**):[36]

$$E_{pa} = \frac{2.3RT}{2(1-\alpha)n_{\alpha}F} log\, v + K \qquad (\mathbf{3})$$

where α is the transfer coefficient, n_{α} number of electrons involved in the rate-determining step, v scan rate, K constant and the rest of the symbols hold their usual meaning. The Tafel slopes of 361 mV/decade (for CoPc-flav-*f*-MWCNTs GCE) and 148 mV/decade (for CoPc-bo-*f*-MWCNTs GCE) are higher than the typical range of 30-120 mV/decade where the electron-transfer kinetics dictate the mechanism of electrocatalysis.[37] In contrast, these higher Tafel slopes gave an indication of the strong interactions occurring between the substrate and electron-mediating thin film .[38]

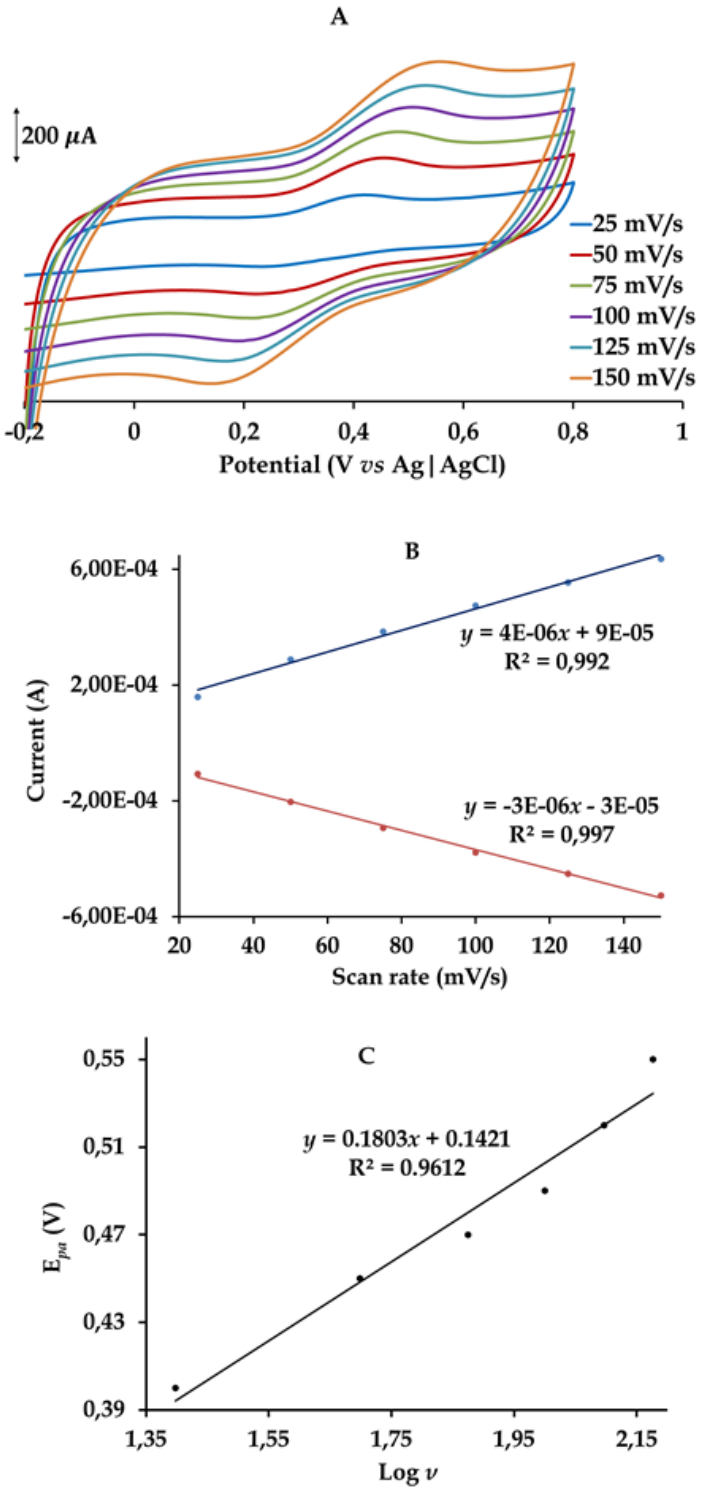

Fig. 3.8: (**A**) *Overlay CVs done in a 1 mM APAP solution prepared in a 0.01 M PBS (at pH 7.4) using the CoPc-flav-f-MWCNTs GCE at different scan rates.* (***B***)*: Plot of* (I_{pa} *or* I_{pc}) *vs scan rate.* (***C***) *Plot of* E_{pa} *vs Log* υ.

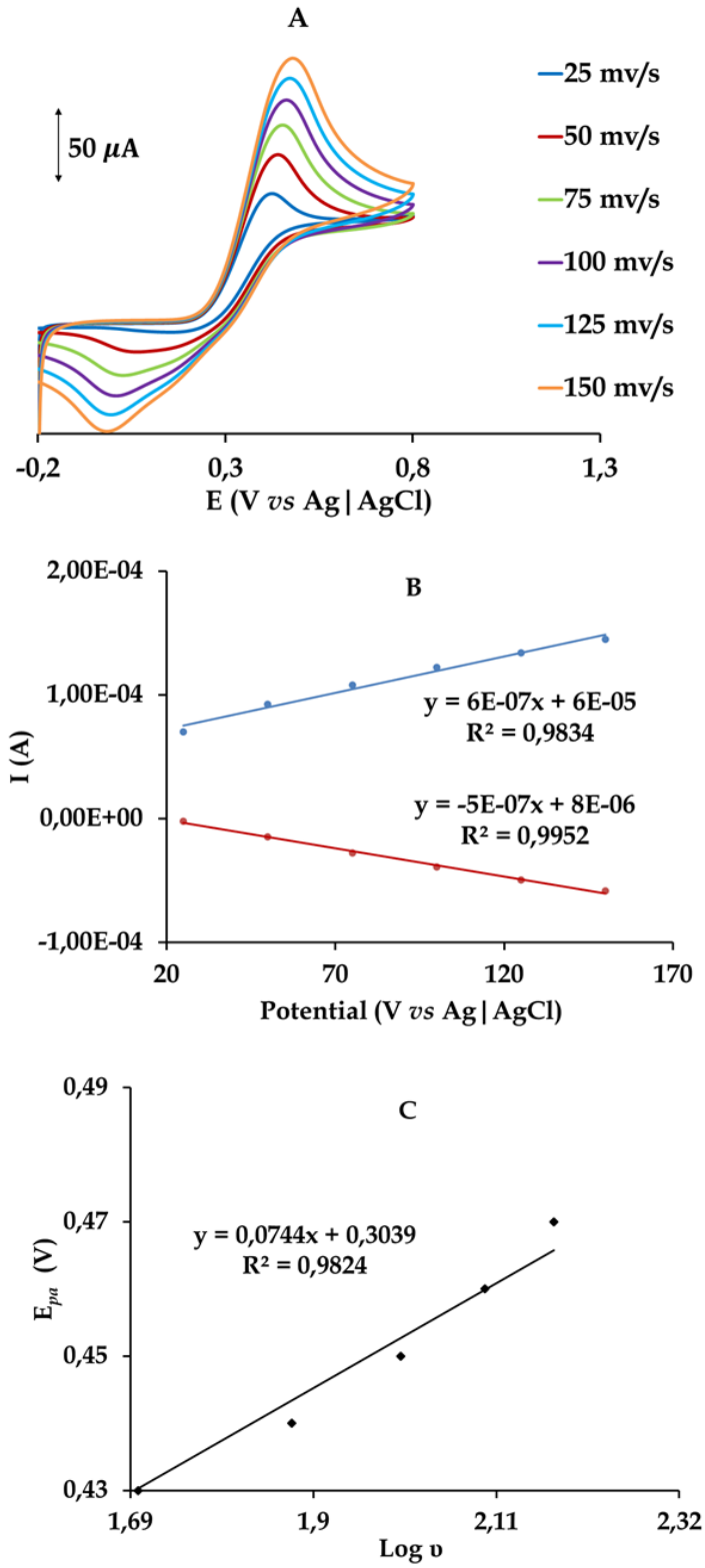

Fig. 3.9: (**A**) *Overlay CVs of 1 mM APAP solution prepared (in 0.01 M PBS, pH 7.4) using the CoPc-bo-f-MWCNTs GCE at different scan rates. (**B**): Plot of (I_{pa} or I_{pc}) vs scan rate. (**C**) Plot of E_{pa} vs Log υ.*

The electrochemical behavior of APAP is significantly influenced by the pH of the medium and thus, the latter can impact the electrochemical sensing capabilities of the chemically modified electrodes. To validate the choice of pH 7.4, CVs were collected of 1 mM APAP aliquots with pH values varying from 3 – 8 and these overlay CVs are depicted in **Fig. 3.10**. At acidic pH, the equilibrium of the reversible redox reaction lies towards APAP which resulted in negligible redox currents while at pH 8.3, the ΔE value was widened in comparison to the CV collected at pH 7.4. Thus, to ensure optimal redox signals (*viz.* peak currents and potentials), pH 7.4 was utilized during all the electrocatalytic studies.

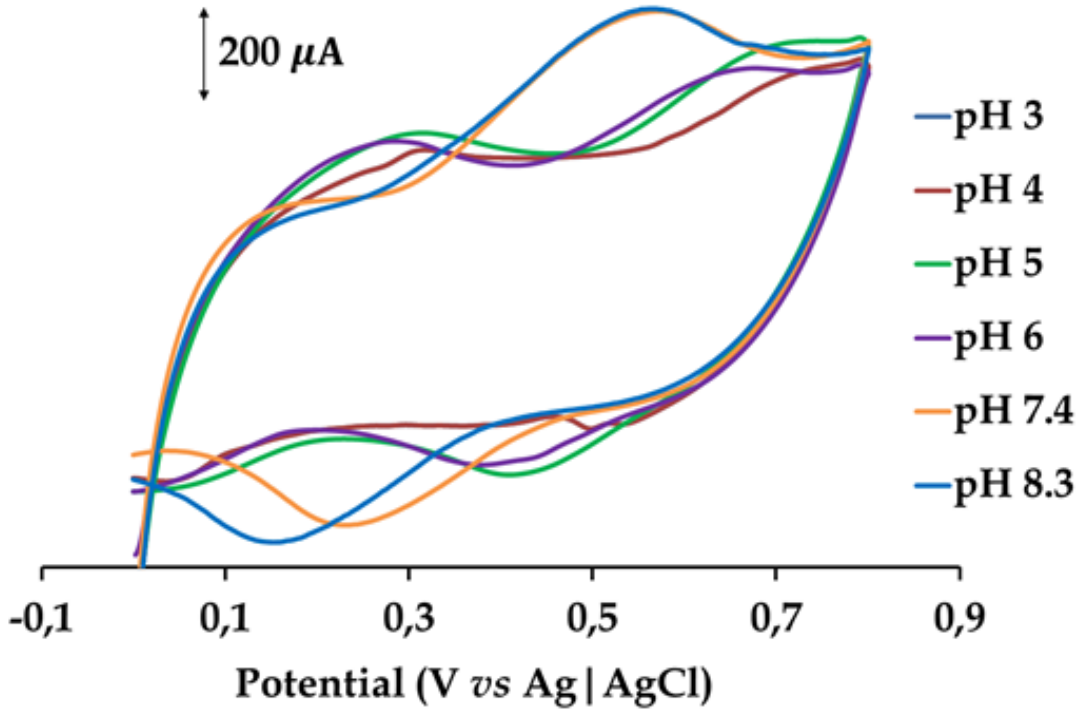

Fig. 3.10: *CVs conducted in 1 mM of APAP at different pH values of a 0.1 M PBS buffer recorded with the CoPc- f-MWCNTs-flav GCE at a scan rate of 100 mV/s.*

3.3.3. Surface area and coverage

The surface area plays an integral role in the electrocatalytic efficiencies of working electrodes modified with electron-mediating thin films. In order to ascertain changes in the surface areas of the individual working electrodes, a 5 mM of

$K_3[Fe(CN)_6]$ was used to probe the surfaces of the respective CMEs. Figures **3.11** and **3.12** show the CVs using the CMEs at variable scan rates done in 5 mM $K_3[Fe(CN)_6]$ prepared an aqueous solution of 0.1 M KCl. With the aid of the Randles-Sevcik equation (**Equation 4**),[39] the effective surface areas of the corresponding modified working electrodes were calculated:

$$I_{pa} = 2.69\ x\ 10^5 A D^{1/2} n^{3/2} v^{1/2} C \qquad (\mathbf{4})$$

where A is the effective surface area, D is the diffusion coefficient of $K_3[Fe(CN_6)]$, v is the scan rate, C is the bulk concentration of $K_3[Fe(CN)_6]$, n is the number of electrons transferred (n = 1). Interestingly, the effective surface areas were found to be 1.21 cm^2 (for CoPc-bo-*f*-MWCNTs GCE) and 1.15 cm^2, (for CoPc-flav-*f*-MWCNTs GCE). These values are higher than the surface area (0.503 cm^2) of the bare electrode. These noticeable significant increases in the surface areas of the CMEs are attributed to the influence of the MWCNTs. The enhanced surface areas induced by the presence of the MWCNTs within the thin films are a testimony to surface modification by nanoparticles whereby the higher surface areas afford more electrocatalytic sites.

The maximum surface coverage (Γ) of each CME was used to estimate the moles per unit area of the corresponding CoPcs present within the respective thin films according to equation **5**:[40]

$$I_{pc} = \frac{n^2 F^2 A\, \Gamma(v)}{4RT} \qquad (\mathbf{5})$$

where I_{pc} is the peak current of cobalt redox (Co^{II} / Co^{III}), n is the number of electrons and A is the real surface area of the bare electrode. From the slopes of the $I_{pc}\ vs\ v^{1/2}$ plots, the apparent surface coverage values of 6.02 x 10^{-11} mol cm^{-2} and 9.22 x 10^{-11} mol cm^{-2} were determined, see **Figs. 3.13** and **3.14**. Both surface coverages are less than the previously reported values (≈ 1 x 10^{-10} mol cm^{-2}) for a Pc molecule lying flat on the surface of the electrode surface.[41] This suggest that the thin films can be

regarded as amorphous due to the uneven distributions of the nanoconjugates on the electrodes.

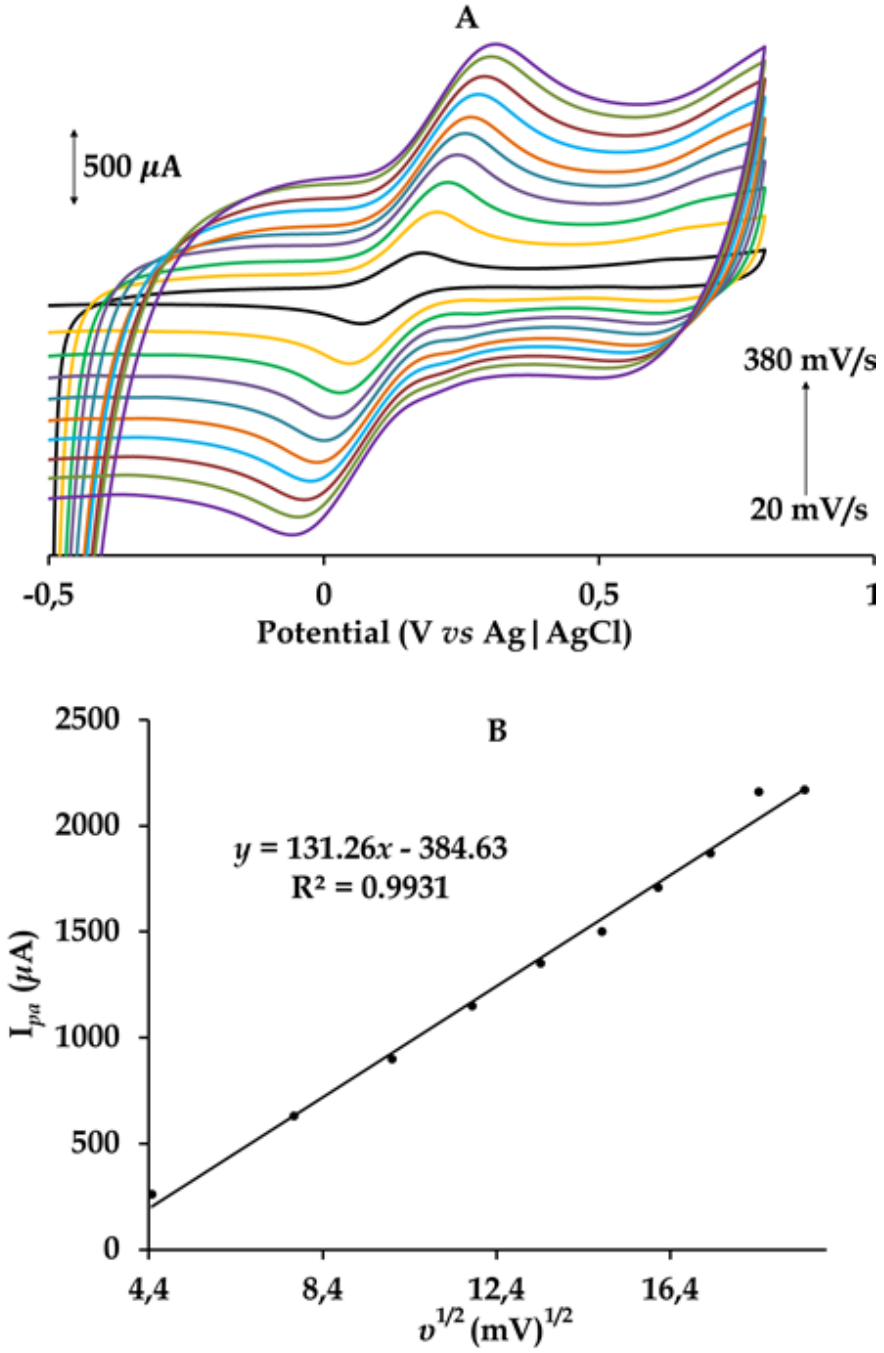

Fig. 3.11: *CVs curves conducted in 5.0 mM $K_3[Fe(CN_6)]$ prepared 0.1 M KCl(aq) at pH using the CoPc-bo-f-MWCNTs GCE at different scan rates (20, 60, 100, 140, 180, 220, 260, 300, 340 and 380 mV/s). (**B**) Plot of I_{pa} vs square root of scan rate.*

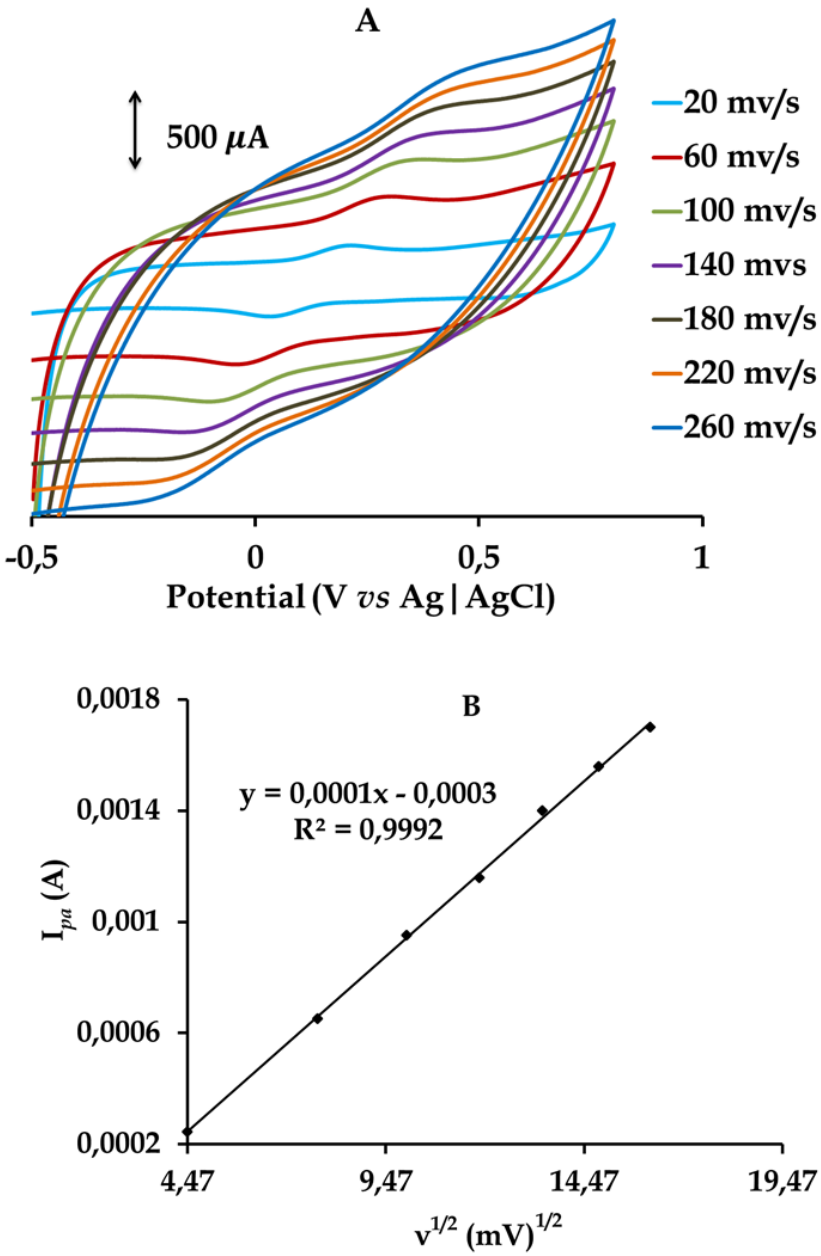

Fig. 3.12: *CVs curves of 5.0 mM $K_3[Fe(CN_6)]$ prepared 0.1 M KCl (aq) at pH using the CoPc-flav-f-MWCNTs GCE at different scan rates (20, 60, 100, 140, 180, 220, 260, 300, 340 and 380 mV/s). (**B**) Plot of I_{pa} vs square root of scan rate.*

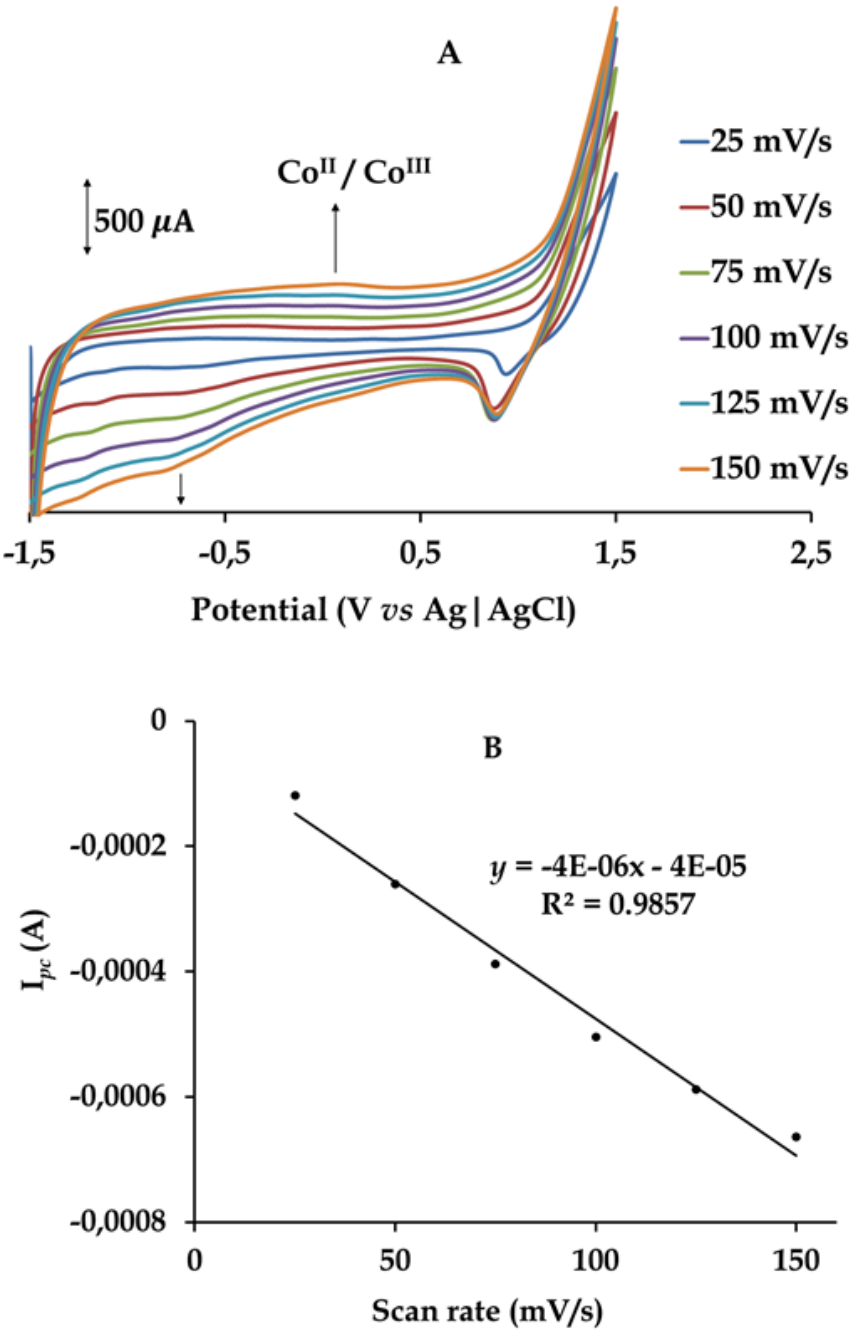

Fig. 3.13: (**A**) *CV curves at progressively increasing scan rates attained in a 0.1 M PBS buffer solution (at pH 7.4) using the CoPc-flav-f-MWCNTs GCE. Inset.* (**B**) *Plot of* I_{pc} *vs scan rate.*

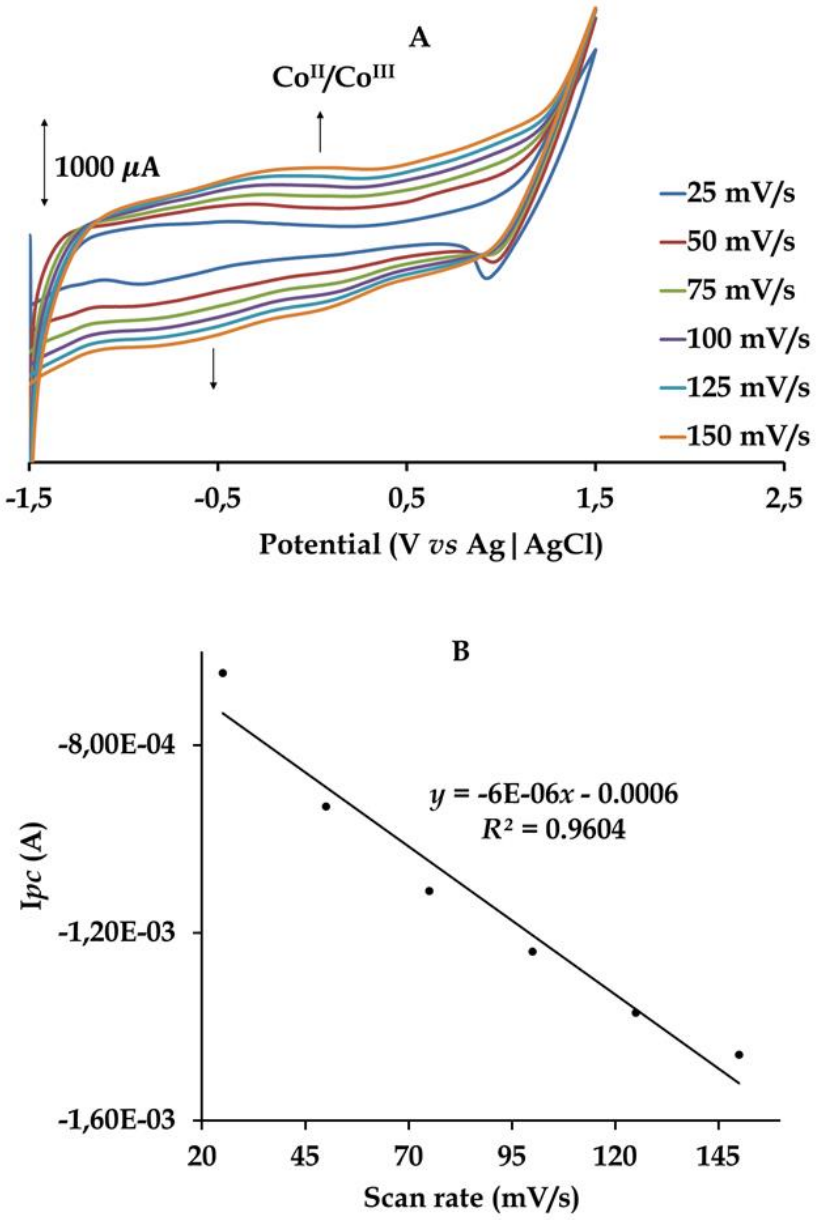

Fig. 3.14: (**A**) *CV curves at progressively increasing scan rates attained in a 0.1 M PBS buffer solution (at pH 7.4) using the CoPc-bo-f-MWCNTs GCE. Inset.* (**B**) *Plot of* I_{pc} *vs scan rate.*

3.3.4. Electrochemical impedance spectroscopy studies

Electrochemical impedance spectroscopy (EIS) was employed to investigate the interfacial electron-transfer kinetics and the mechanism of electrocatalysis of the CMEs.[42] The EIS data were analyzed using Nyquist plots which indicate the response of the electrode/electrolyte system and is shown as a plot of the imaginary component (-Z″) against the real component (Z′), see **Fig. 3.15**. It is well established that the semi-circle diameter at higher frequencies in the Nyquist plot is proportional to the charge transfer resistance (R_{ct}) and this resistance to charge transfer is an indirect parameter of gauging the electrical conductivity occurring at the electrode surface. At lower frequency, the Warburg impedance dominates which is typically for diffusion-controlled systems where diffusing of the redox active species from the bulk solution is the rate-determining step.[43]

Good correlations are found between the experimental and modelled data using an equivalent circuit shown in **Fig. 3.15**. This equivalent circuit is comprised of R_s, R_{ct}, CPE and Z_w components which represent the solution/electrolyte resistance, charge-transfer resistance, constant phase elements and the Warburg impedance, respectively. The CPEs accommodate for the heterogeneity of the electrode surface. More specifically, the $CPE_{(1)}$ relates to non–homogeneity of the electrodes due to surface roughness ($n < 1$) whereas $CPE_{(2)}$ ($n = 0.5$) caters for semi-infinite diffusion of the redox species.[44, 45] The superior electrical conductivity of the CoPc-X-f-MWCNTs GCEs were emphasized by its lower R_{ct} values of 64.8 Ω (for X = flav) and 19.8 Ω (for X = bo) compared to that obtained for the bare GCE (R_{ct} = 8.46 kΩ). The enhancements of the charge transfer kinetics for the CMEs were largely attributed to the presence of MWCNTs and these electrochemical trends are accustomed to MPc-MWCNTs nanoconjugate during electrocatalytic transformations of redox-active analytes.

These EIS trends corroborated the higher APAP redox currents obtained in the CVs acquired with the CMEs relative to the bare GCE's low peak currents. The Bode

plots illustrate that the phase angle for the bare GCE (~70 °C) was higher than those attained for CoPc-flav-*f*-MWCNTs (~8 °C) and CoPc-bo-*f*-MWCNTs (~3 °C) GCEs. These phase angles were less than (90 °C) for an ideal capacitor and indicate that the thin layers of the CMEs are permeable to charged species.[46] In addition, the frequencies of the CMEs were slightly negatively shifted compared to the bare electrode which suggested that the $[Fe(CN)_6]^{4-}/[Fe(CN)_6]^{3-}$ redox processes occurred at the interfaces of the respective CMEs, see **Fig. 3.16**. Synonymously to the latter, other CMEs have showed progressive shifts in their phase angles to lower frequencies which were accounted to their high electrocatalytic activities.[47]

Table 2: *Summary of EIS data collected in a 5 mM $[Fe(CN)_6]^{3-/4}$ using the bare and modified working electrodes. Error values are shown in brackets.*

GCE	R_s (Ω)	R_{ct} (Ω)	Z_w (*m*S)	$CPE_{(1)}$ (*m*S)	[a]*n*	$CPE_{(2)}$ (*μ*S)	[a]*n*
Bare	96.7 (0.6)	8460 (1.0)	0.00764 (1.4)	-	-	1.44 (2.0)	0.908 (0.3)
CoPc-flav-*f*-MWCNTs	72.3 (2.6)	19.8 (10.2)	9.88 (4.4)	2.82 (1.6)	0.9 (1.0)	131 (30.6)	0.5 (8.2)
CoPc-bo-*f*-MWCNTs	94.2 (0.6)	64.8 (3.7)	4.56 (6.8)	1.25 (2.8)	0.9 (1.9)	513 (7.3)	0.5 (2.1)

[a]*n is the exponent related to the depression angle.*

Values in brackets are percentage errors obtained from fitting the experimental Nyquist plots

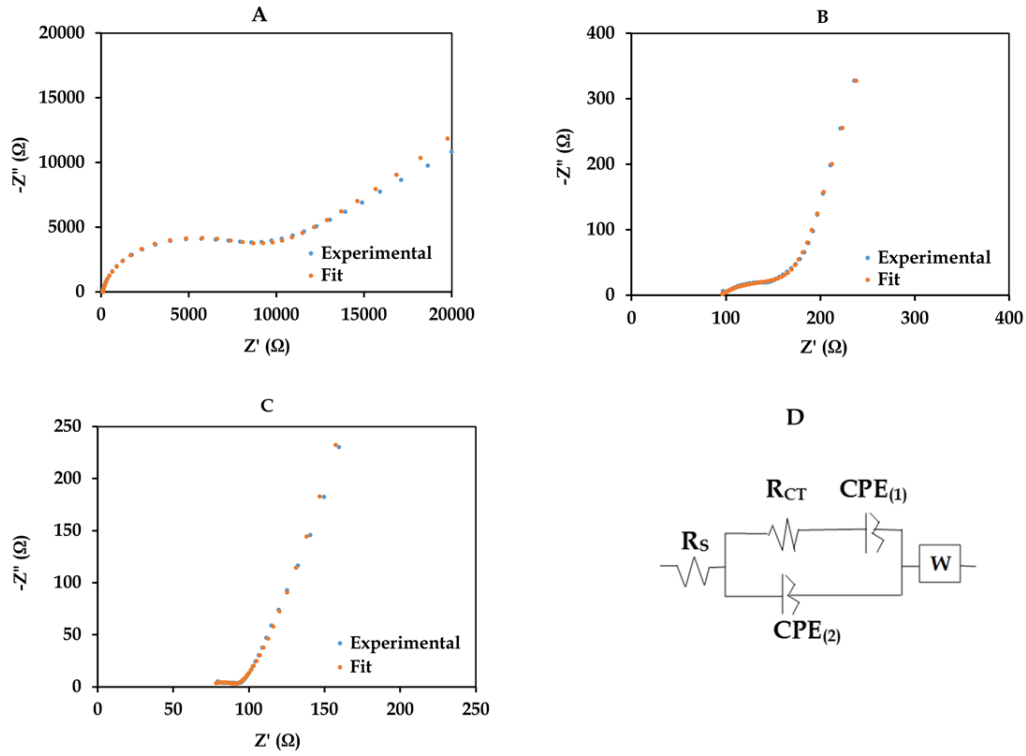

Fig. 3.15: *Nyquist plots attained in solution of 5 mM $[Fe(CN)_6]$ prepared PBS using (**A**) bare GCE, (**B**) CoPc-flav-f-MWCNTs GCE and (**C**) CoPc-bo-f-MWCNTs GCE. (**D**) Equivalent circuit used to fit the EIS data.*

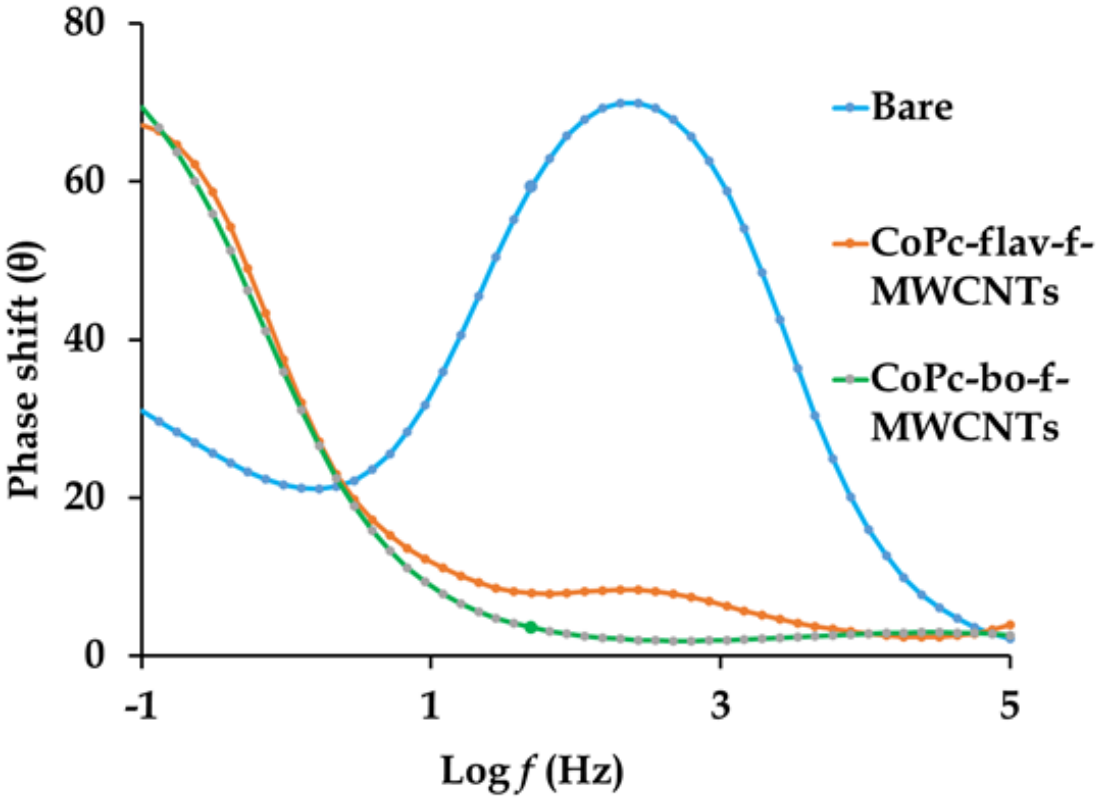

Fig. 3.16: *Bode plots generated with the respective working electrodes.*

3.3.5. Redox reactions kinetics

Convection and diffusion-controlled kinetics were investigated using rotating and stationary CMEs, respectively. In particular, single-step chronoamperometry was used to determine the diffusion-controlled electro-oxidation rate constants of the individual CMEs, see **Figs. 3.17** and **3.18**. These kinetic rate constants could be readily quantified by applying controlled overpotentials (*w.r.t.* E_{pa} of the APAP CVs) at an intermediate data collection interval of 5 – 20 seconds, using the bare and the individual CoPc-X-*f*-MWCNTs GCEs. It is well established that the reaction rates occurring at the surface of static electrodes can be defined using the following expression:

$$\frac{I_{\text{cat}}}{I_{buf}} = \frac{\gamma^{1/2}(\pi^{1/2}\,\text{erf}(\gamma^{1/2})+\exp(-\gamma))}{\gamma^{1/2}} \qquad (6)$$

where I_{cat} and I_{buff} are the catalytic currents attained in either the analyte and the buffer solutions using the respective CMEs, $\gamma = kCt$ with (C being the bulk molar concentration of the analyte, *k* is the catalytic rate constant while *t* is the time elapsed in seconds) and erf is the error function. Equation (**6**) can be simplified if γ is greater than 2 and the error function is almost equal to 1. Thus, the simplified Cottrell equation can be used to approximate the diffusion kinetics of the respective CMEs:[48]

$$\frac{I_{cat}}{I_{buf}} = \gamma^{1/2}\pi^{1/2} = \pi^{1/2}(kC_o t)^{1/2} \quad (7)$$

Thus, the diffusion-controlled rate constants could be calculated from the slopes of the plots of I_{cat}/I_{buff} *vs* $t^{1/2}$, generated using the individual CoPc-X-*f*-MWCNTs GCEs [1.67 x 10^2 M^{-1} s^{-1} (where X = flav) and 1.44 x 10^2 M^{-1} s^{-1} (where X =bo)]. Rate constants in the order of 10^2 M^{-1} s^{-1} can be regarded as moderate considering the values around $10^{3/4}$ M^{-1} s^{-1} attained for other MPc-based electrochemical sensors during chronoamperometry experiments.[41, 47, 49, 50]

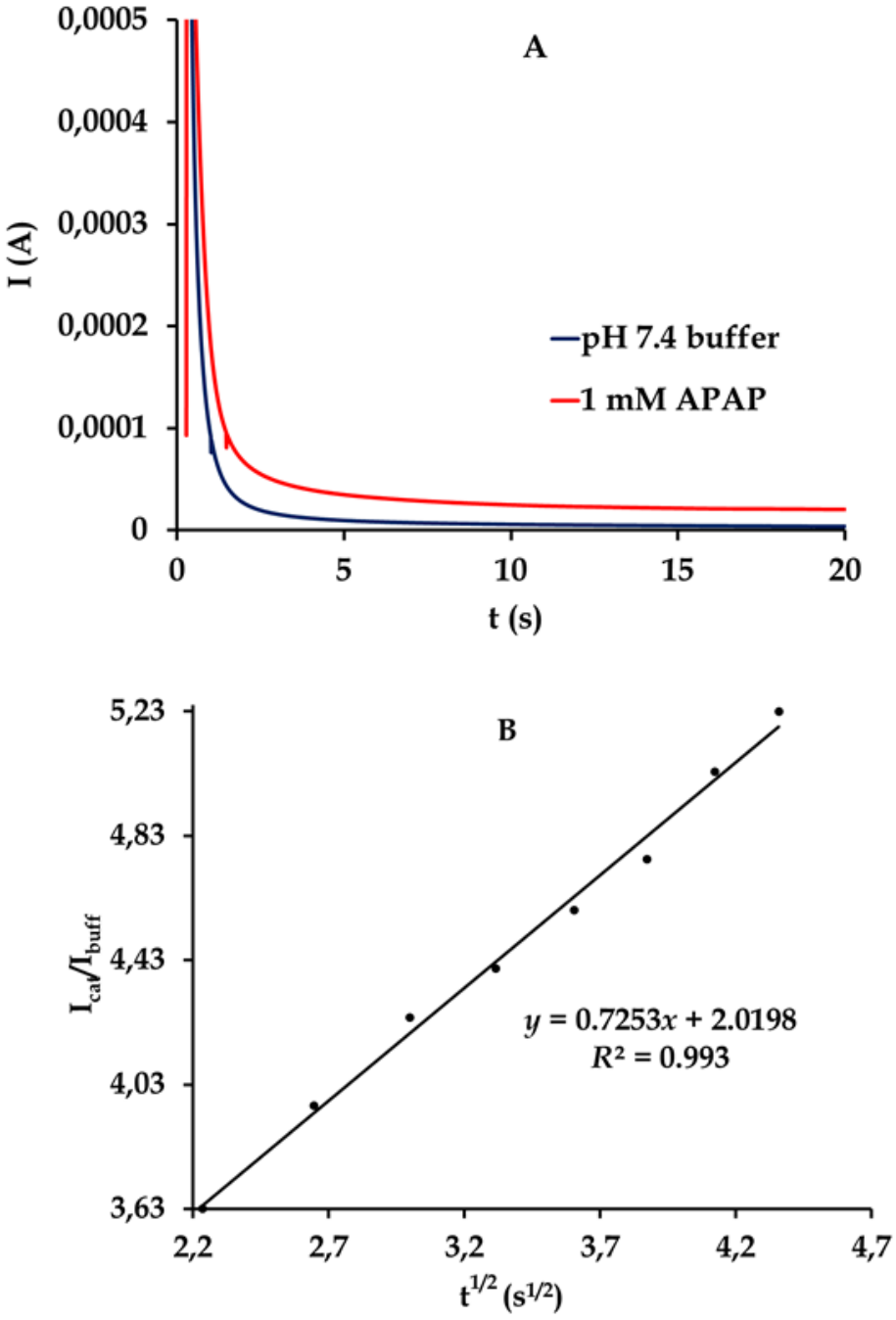

Fig. 3.17: *(**A**) Chronoamperograms generated in a 1 mM APAP prepared in pH 7.4 PBS buffer using the CoPc-flav-f-MWCNTs GCE. (**B**) Plot of* $\frac{I_{cat}}{I_{buff}}$ *vs* $t^{1/2}$.

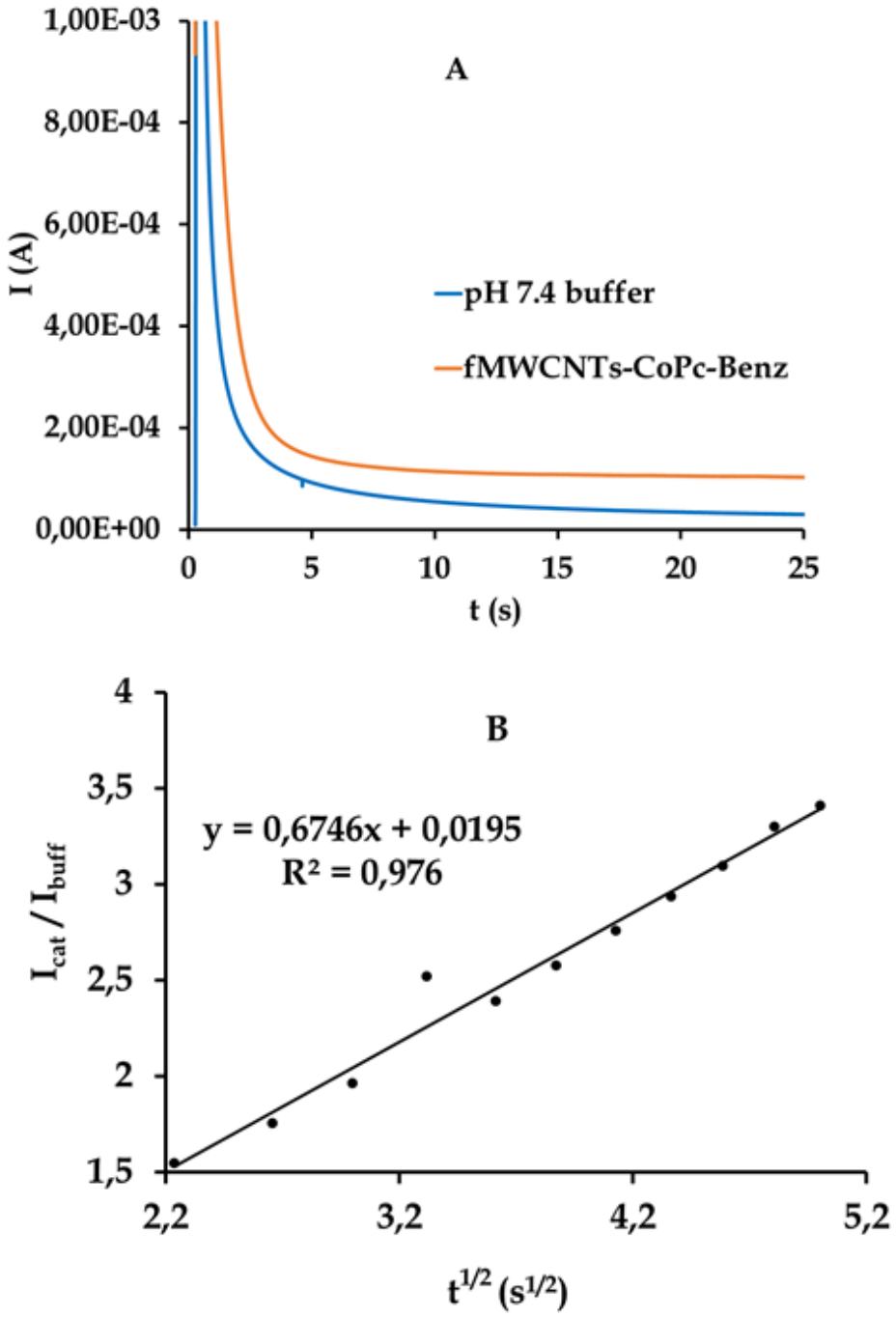

Fig. 3.18: *(**A**) Chronoamperograms generated in a 1 mM APAP prepared in pH 7.4 PBS buffer using the CoPc-bo-f-MWCNTs GCE. (**B**) Plot of* $\frac{I_{cat}}{I_{buff}}$ *vs* $t^{1/2}$.

Voltammetric detection of an analyte within a complex sample matrix can often suffer from interference by other redox active species. However, the hydrodynamic technique can be employed as it affords higher redox currents and leads to a more sensitive detection signal for the analyte of concern. In order to investigate the convection-controlled kinetics of the CMEs, the respective modified electrodes were rotated at variable rates while the linear sweep voltammograms (LSVs) were collected at relatively low scan rate to minimize eddy diffusion, see **Figs. 3.19** and **3.20**. A linear relationship between limiting current (I_L) and square root of the rotational rates ($\omega^{1/2}$) of the rotating disk electrode (RDE) affirmed that the mass transport to the CME surfaces was largely dominated by convection and this relationship can be defined by the Levich equation:

$$I_L = 0.62nFAD^{2/3}\nu^{-1/6}\omega^{1/2}C_0 \quad (\mathbf{8})$$

where D is the diffusion coefficient of the substrate, A is the electrode area, ν is the kinematic viscosity, ω is rotation rate and C_0 is the bulk concentration of the analyte. Accordingly, the oxidation rate constant of APAP occurring at the surfaces of the CoPc-X-*f*-MWCNTs GCEs was estimated using the equation:

$$I_{Kin} = nFAC_0k\Gamma \quad (\mathbf{9})$$

where Γ is the surface coverage, k is the heterogeneous rate constant and all the other symbols have their usual meanings. Combining equations (**8**) and (**9**) rendered the Koutecky-Levich expression which can be used to calculate the overall convection-controlled rate constants:[51]

$$\frac{1}{I_L} = \frac{1}{nFAC_o k\Gamma} + \frac{1}{0.62nFAD^{2/3}\upsilon^{-1/2}C_o\omega^{1/2}} \quad (\mathbf{10})$$

Therefore, the corresponding plots of $(I_L)^{-1}$ *vs* $\omega^{-1/2}$ gave straight lines with good correlation coefficients and their intercepts yielded the rate constants of 6.9 $x10^4$ M^{-1} s^{-1} and 3.48 $x10^4$ M^{-1} s^{-1} for the oxidative transformation of APAP occurring at the surfaces of the CoPc-bo-*f*-MWCNTs and CoPc-flav-*f*-MWCNTs GCEs, respectively. As per the expected faster convection mass transport rates, the

hydrodynamic experiments revealed rate constants nearly twice in magnitude as those produced when using the chronoamperometric technique.

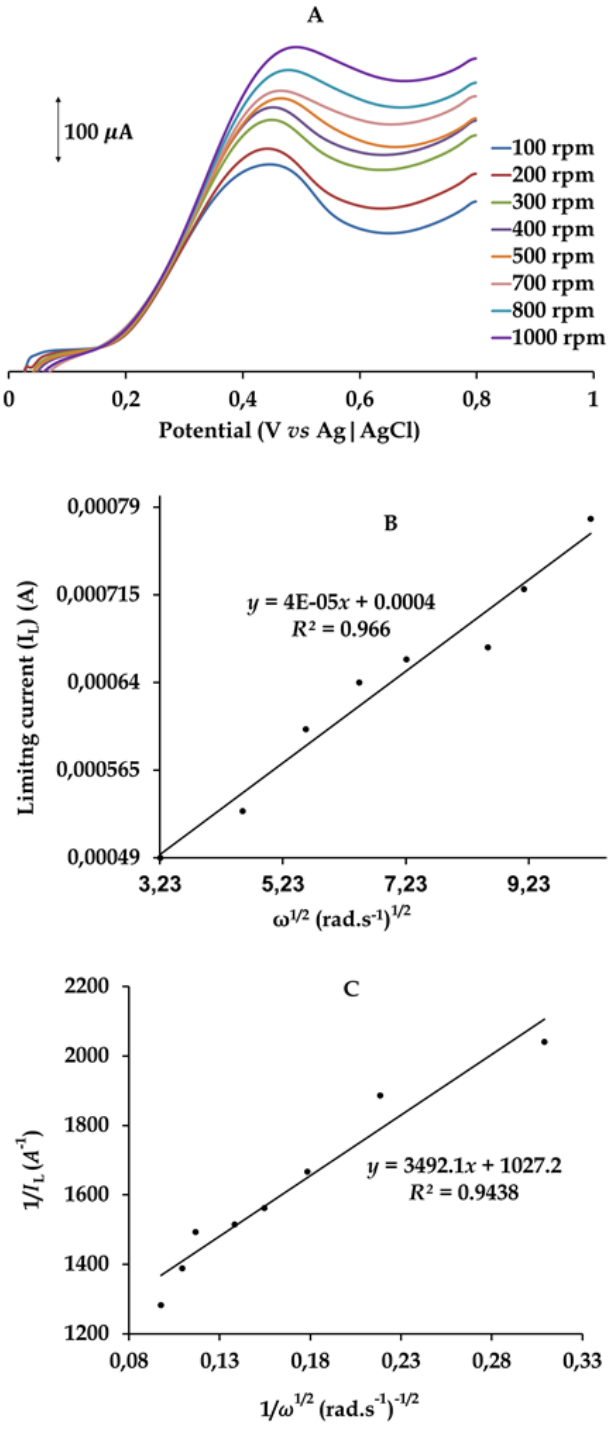

Fig. 3.19: (**A**): *RDE-LSVs attained at a scan-rate of 25 mV/s and using the CoPc-bo-f-MWCNTs GCE, in a 1 mM APAP standardized in a pH 7.4 PBS buffer solution*. (**B**) *The Levich plot.* (**C**) *The Koutecky-Levich plot.*

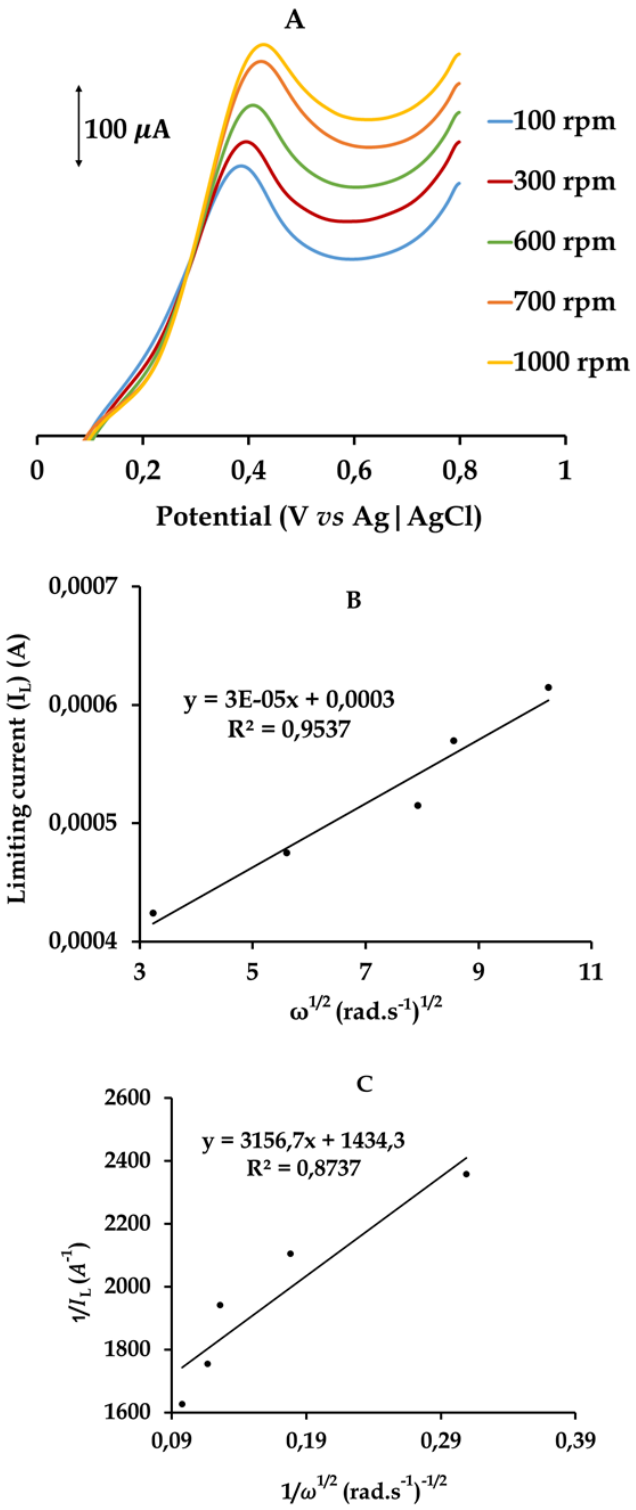

Fig. 3.20: (**A**): *RDE-LSVs of 1 mM APAP (in a pH 7.4 PBS buffer solution) attained at a scan-rate of 25 mV/s and using the CoPc-flav-f-MWCNTs GCE, in a.* (**B**) *The Levich plot.* (**C**) *The Koutecky-Levich plot.*

3.3.6. Analytical application

Linear responses of the respective CMEs were assessed using squarewave voltammetry (SWV), see **Figs. 3.21** and **3.22**. APAP could be detected in relatively wide linear ranges using the CoPc-X-*f*-MWCNTs GCEs with concentration ranging from 1 to 1000 μM L^{-1} (for **X** = flav) and 15 to 1000 μM L^{-1} (for **X** = bo), respectively. However, the majority of previously reported CMEs afforded lower detection limits than both of the CoPc-X-*f*-MWCNTs GCEs. Furthermore, the linear regression equations for both modified electrodes can be expressed as follows:

$$I_{pa} = 0.0657C + 3.7112 \ (R^2 = 0.9952) \quad (\mathbf{10})$$

$$I_{pa} = 0.044C + 14.594 \ (R^2 = 0.8741) \quad (\mathbf{11})$$

The lower correlation coefficient attained when using the CoPc-bo-*f*-MWCNTs GCE is attributed to the surface fouling occurring at elevated concentrations (≥ 500 μM). One of the integral attributes of a functional electrochemical sensor is its ability to discriminate the presence of interferences in the same sample solution. Metronidazole (MTZ) and ibuprofen (IB) were selected as interferences which is rationalized by their significant concentrations found in water samples attained from the Msunduzi river, see **Figs. 3.23** and **3.24**. Interestingly, using CoPc-flav-*f*-MWCNTs GCE, SWV analysis of a sample matrix comprised of APAP (at 0.38 V *vs* Ag|AgCl), MTZ (at -0.76 V *vs* Ag|AgCl) and (at 0.76 V *vs* Ag|AgCl) IB rendered a clear distinguishable APAP peak accompanied with fair resolutions with respect to the signals corresponding to the interferences. However, in the SWV of the same sample solution attained with CoPc-bo-*f*-MWCNT GCE, IB could not be detected, although (APAP) at 0.43 V *vs* Ag|AgCl and MTZ at -0.75 V *vs* Ag|AgCl) were detected in good resolution. The difference in the SWVs by the two CMEs emphasized the influence of the CoPc substituents on the electrocatalytic activities of the respective CMEs.

The selectivity of the modified electrodes was further tested in the presence of a range of bio-interferences. It is well known that dopamine (DA), ascorbic acid (AA) and paracetamol (APAP) coexist in biological fluids. Thus, the selective detection and

accurate quantification of APAP in biological media for conditions induced by these emerging pharmaceuticals is of importance for correct diagnosis, see **Figs. 3.25** and **3.26.** Noticeably, none of the CoPc-X-*f*-MWCNTs GCEs showed electrocatalytic affinity towards AA while the SWV indicated poorly resolved peaks for DA (at 0.34 V for X = flav and 0.23 V for X = bo) and APAP (at 0.70 V for X = flav and 0.46 V for X = bo), respectively. The significant shift in the redox potentials of APAP is ascribed to the influence of AA which alters the pH from 7.4 to 5 .[52]

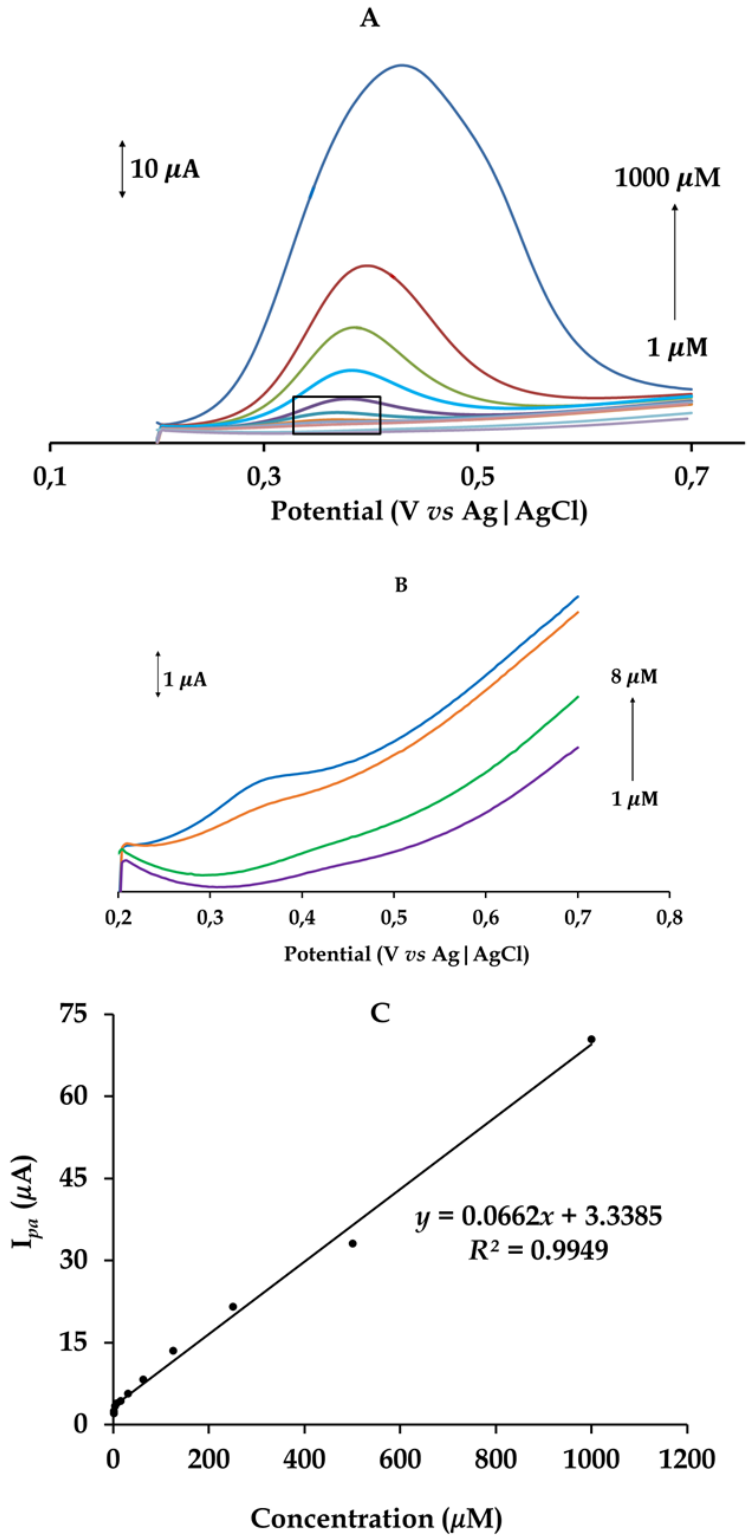

Fig. 3.21: (**A**): *SWVs recorded in varying concentration of APAP prepared in PBS (pH 7.4) using the CoPc-flav-f-MWCNTs GCE.* (**B**): *Amplified SWV response to APAP at low concentration (1 to 8 μM) as shown in black rectangle.* (**C**): *Calibration curve of the current response against APAP concentration (1 to 1000 μM).*

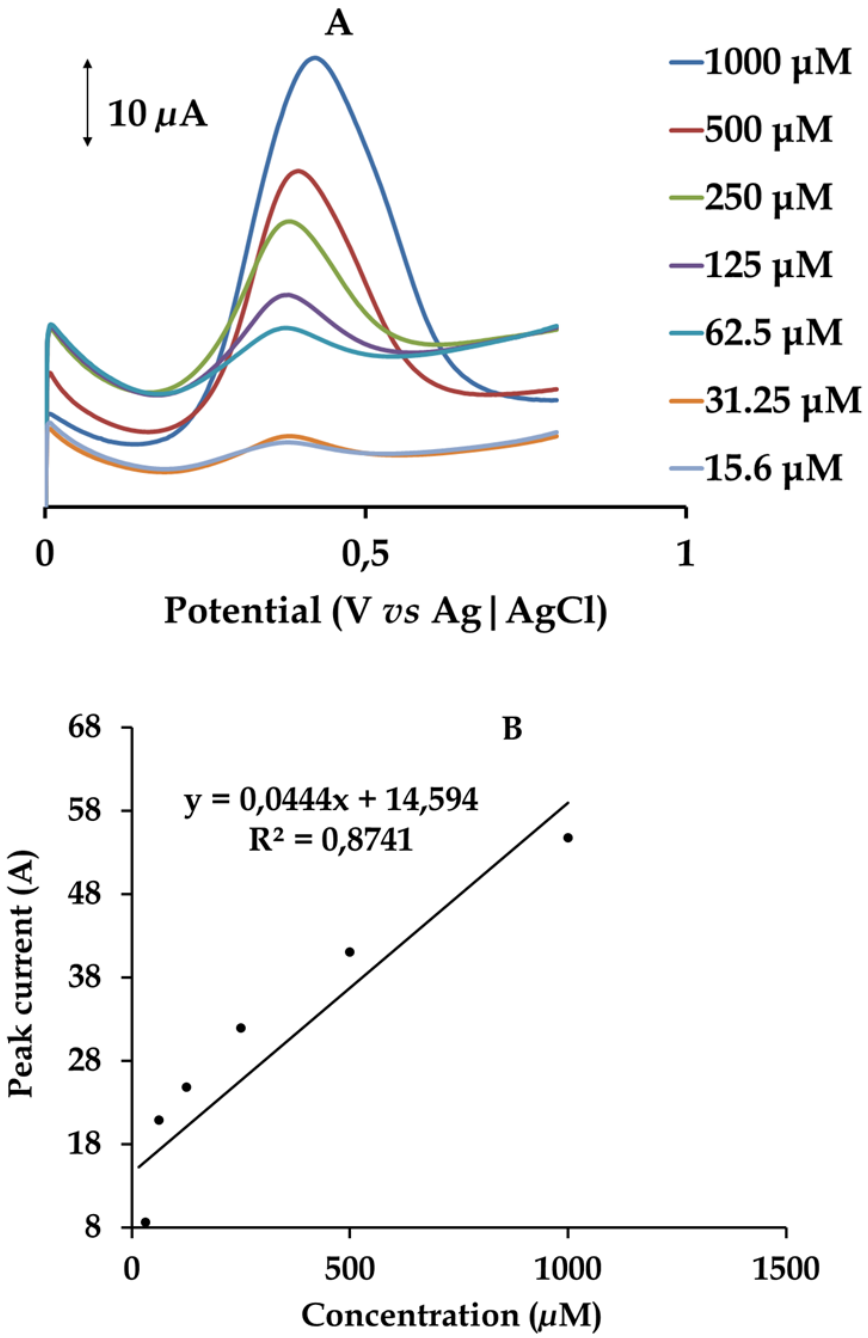

Fig. 3.22: (**A**): *SWVs recorded in varying concentration of APAP prepared in PBS (pH 7.4) using the CoPc-bo-f-MWCNTs GCE.* (**B**): *Calibration curve of the current response against APAP concentration (15.6 to 1000 μM).*

Table 2: *Comparison of the performances of chemically modified electrodes for oxidation of paracetamol.*

Electrodes	Detection Method	Limit of detection, LOD (μM)	Linear range (μM)	References
Graphene GCE	SWV	0.03	0-20	53
MWCNT-βCD GCE	DPV	0.0115	0.05-300	54
AuNPs-*f*-MWCNT CoPc GCE	SWV	0.13	1.49-107	55
Chitosan CPE	SWV	0.508	0.8-200; 400-1000	26
Gr/PDDA/PSS-[MWCNTs–NH_3 +–MWCNTs–COO^-]$_5$	DPV	0.5	25-400	52
CoPc-flav-f-MWCNTs GCE	SWV	1	0.98-1000	This work
CoPc-bo-f-MWCNTs GCE		15	15.6-1000	

Acronyms:

MWCNT GCE = Multi-wall carbon nanotube modified GCE

AuNPs-f-MWCNT-CoPc GCE = GCE modified with Au nanoparticles (AuNPs), functionalized MWCNT and cobalt phthalocyanine.

Gr/PDDA/PSS-[MWCNTs–NH_3^+–MWCNTs–COO^-]$_5$ = charged MWCNTs on poly(diallydimethyl ammonium chloride (PDDA)/ polystyrene sulfonate (PSS) modified graphite (GR) electrode.

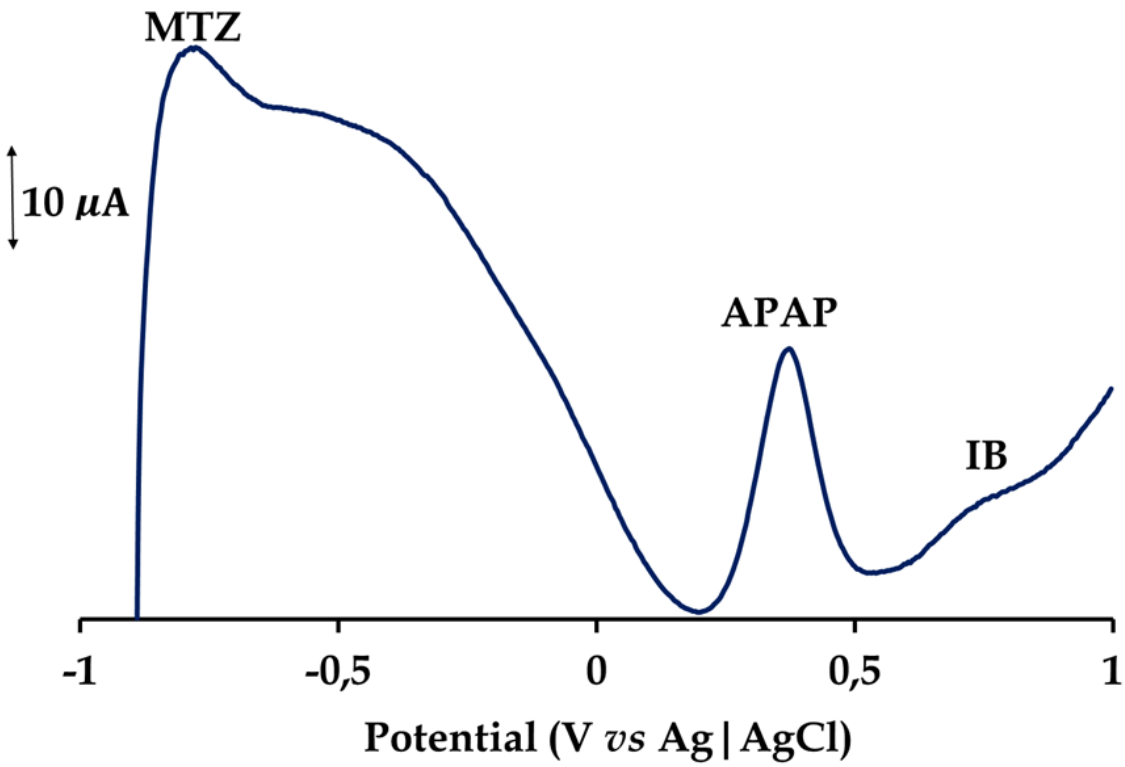

Fig. 3.23: *SWV analysis of a sample matrix comprised of 0.5 mM quantities of APAP, MTZ and IB prepared in PBS buffer using the CoPc-flav-f-MWCNTs GCE.*

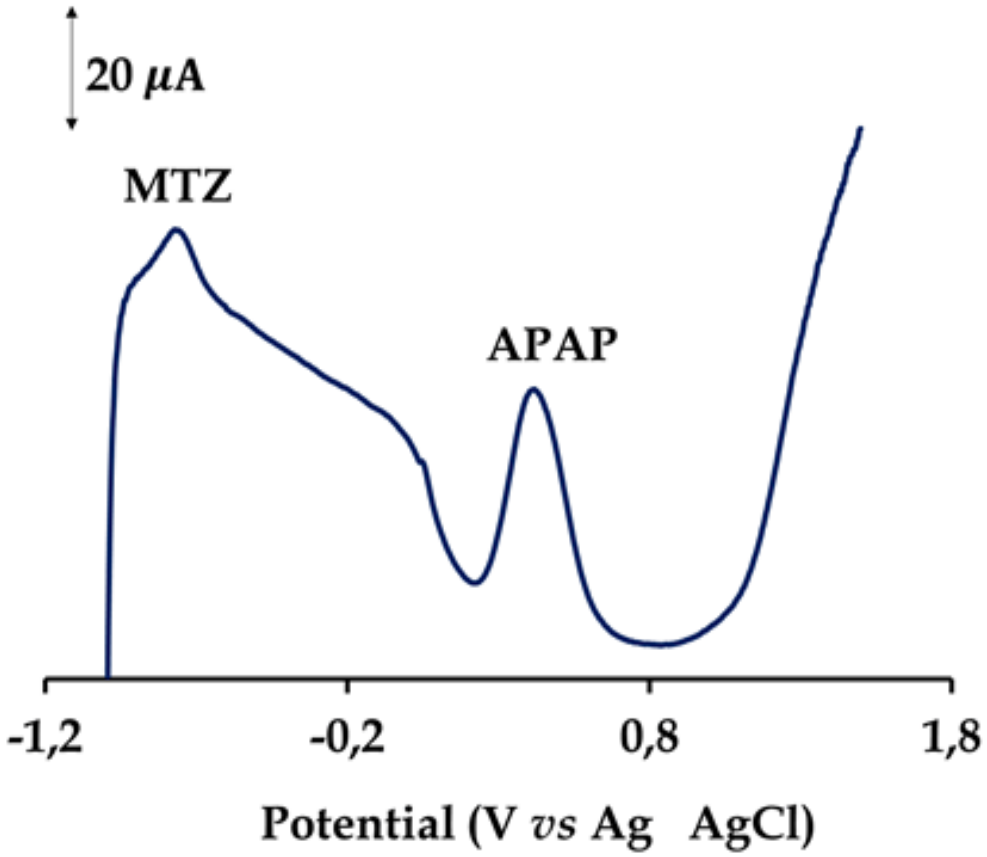

Fig. 3.24: *SWV analysis of 0.5 mM APAP in the presences of a sample matrix comprised of 0.5 mM MTZ and IB in PBS buffer using the CoPc-bo-f-MWCNTs GCE.*

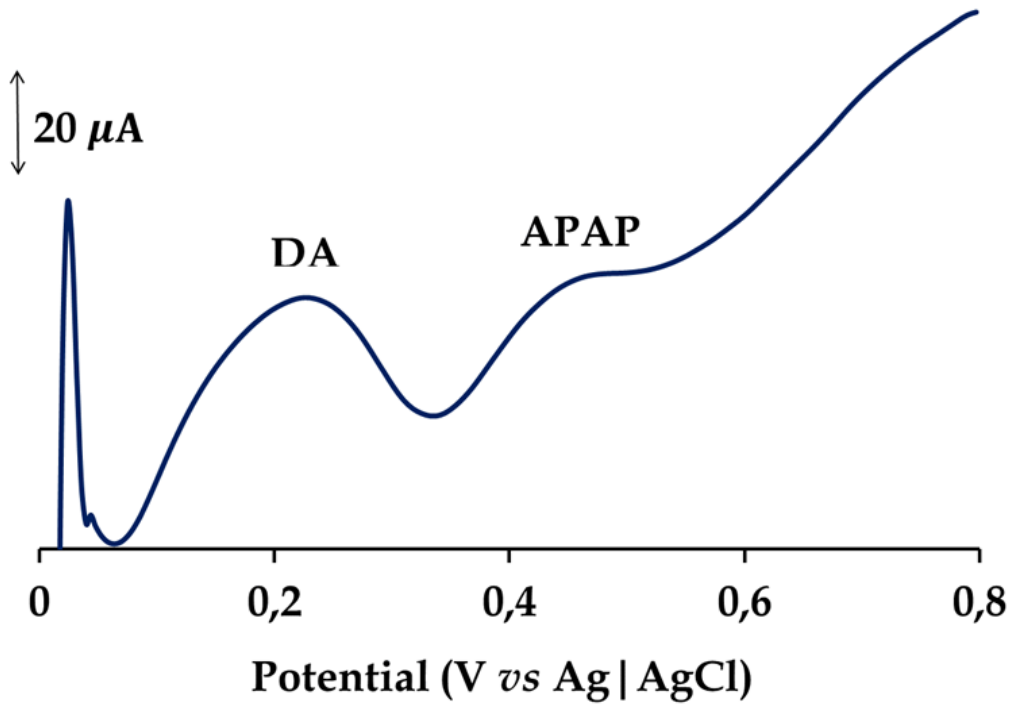

Fig. 3.25: *SWV analysis of 0.5 mM APAP in the presences of a sample matrix comprised of 0.5 mM APAP, DA and AA in PBS buffer using the CoPc-bo-f-MWCNTs GCE.*

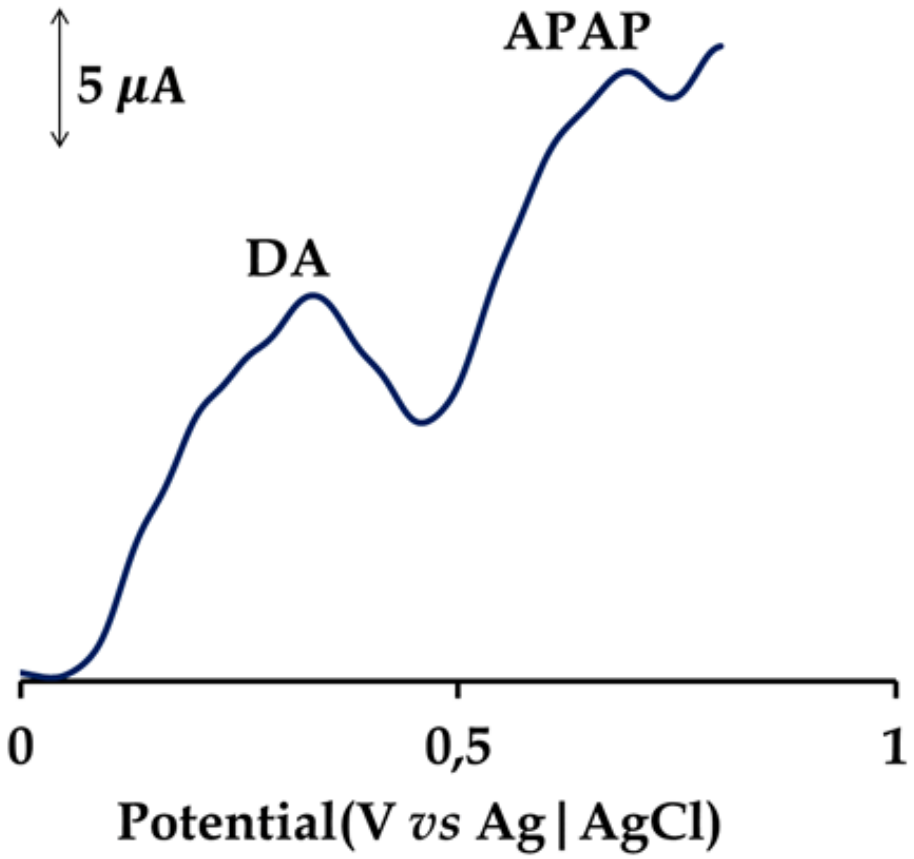

Fig. 3.26: *SWV analysis of 0.5 mM APAP in the presences of a sample matrix comprised of 0.5 mM APAP, DA and AA in PBS buffer using the CoPc-flav-f-MWCNTs GCE.*

3.4. References

1. Fekadu, S.; Alemayehu, E.; Dewil, R.; Van der Bruggen, B., *Science of the Total Environment* **2019,** *654*, 324-337.
2. Madikizela, L. M.; Ncube, S.; Chimuka, L., *Science of the Total Environment* **2018,** *636*, 477-486.
3. Madikizela, L. M.; Tavengwa, N. T.; Chimuka, L., *Journal of environmental management* **2017,** *193*, 211-220.
4. Cashman, A., *Water* **2014,** *6*, 1187-1203.
5. Matongo, S.; Birungi, G.; Moodley, B.; Ndungu, P., *Chemosphere* **2015,** *134*, 133-140.
6. Jiang, J.; Briedé, J. J.; Jennen, D. G.; Van Summeren, A.; Saritas-Brauers, K.; Schaart, G.; Kleinjans, J. C.; de Kok, T. M., *Toxicology letters* **2015,** *234*, 139-150.
7. Mazer, M.; Perrone, J., *Journal of Medical Toxicology* **2008,** *4*, 2-6.
8. Bosch, M. E.; Sánchez, A. R.; Rojas, F. S.; Ojeda, C. B., *Journal of pharmaceutical and biomedical analysis* **2006,** *42*, 291-321.
9. Agunbiade, F. O.; Moodley, B., *Environmental monitoring and assessment* **2014,** *186*, 7273-7291.
10. Archer, E.; Petrie, B.; Kasprzyk-Hordern, B.; Wolfaardt, G. M., *Chemosphere* **2017,** *174*, 437-446.
11. Radjenovic, J.; Petrovic, M.; Barceló, D., *Analytical and bioanalytical chemistry* **2007,** *387*, 1365-1377.
12. Guerra, P.; Kim, M.; Shah, A.; Alaee, M.; Smyth, S., *Science of the Total Environment* **2014,** *473*, 235-243.
13. Roberts, E.; Nunes, V. D.; Buckner, S.; Latchem, S.; Constanti, M.; Miller, P.; Doherty, M.; Zhang, W.; Birrell, F.; Porcheret, M., *Annals of the rheumatic diseases* **2016,** *75*, 552-559.
14. Murtaza, G.; Hussain, I.; Khan, S. A.; Shabbir, A.; Mahmood, A.; Asad, M. H. H. B.; Farzanal, K.; Malik, N. S., *Scientific research and Essays* **2011,** *6*, 417-421.
15. Rote, A. R.; Kumbhoje, P. A.; Bhambar, R. S., *Pharmaceutical methods* **2012,** *3*, 40-43.

16. El-Kommos, M. E.; Mohamed, N. A.; Abdel Hakiem, A. F., *Journal of liquid chromatography & related technologies* **2012,** *35*, 2188-2202.
17. Cunha, R. R.; Chaves, S. C.; Ribeiro, M. M.; Torres, L. M.; Muñoz, R. A.; Santos, W. T. D.; Richter, E. M., *Journal of Separation Science* **2015,** *38*, 1657-1662.
18. Ruengsitagoon, W.; Liawruangrath, S.; Townshend, A., *Talanta* **2006,** *69*, 976-983.
19. Burgot, G.; Auffret, F.; Burgot, J.-L., *Analytica chimica acta* **1997,** *343*, 125-128.
20. Su, S.; Chen, S.; Fan, C., *Green Energy & Environment* **2018,** *3*, 97-106.
21. Yang, B.; Fu, C.; Li, J.; Xu, G., *TrAC Trends in Analytical Chemistry* **2018,** *105*, 52-67.
22. Ghadimi, H.; Tehrani, R. M.; Ali, A. S. M.; Mohamed, N.; Ab Ghani, S., *Analytica chimica acta* **2013,** *765*, 70-76.
23. Adhikari, B.-R.; Govindhan, M.; Chen, A., *Electrochimica Acta* **2015,** *162*, 198-204.
24. Cheemalapati, S.; Palanisamy, S.; Mani, V.; Chen, S.-M., *Talanta* **2013,** *117*, 297-304.
25. Goyal, R. N.; Gupta, V. K.; Oyama, M.; Bachheti, N., *Electrochemistry communications* **2005,** *7*, 803-807.
26. Bouabi, Y. E.; Farahi, A.; Labjar, N.; El Hajjaji, S.; Bakasse, M.; El Mhammedi, M., *Materials Science and Engineering: C* **2016,** *58*, 70-77.
27. Mashazi, P. N.; Westbroek, P.; Ozoemena, K. I.; Nyokong, T., *Electrochimica acta* **2007,** *53*, 1858-1869.
28. Chohan, S.; Booysen, I. N.; Mambanda, A.; Akerman, M. P., *Journal of Coordination Chemistry* **2015,** *68*, 1829-1846.
29. Bedioui, F.; Griveau, S.; Nyokong, T.; Appleby, A. J.; Caro, C. A.; Gulppi, M.; Ochoa, G.; Zagal, J. H., *Physical Chemistry Chemical Physics* **2007,** *9*, 3383-3396.
30. Jin, X.; Liu, C.; Wang, X.; Huang, H.; Zhang, X.; Zhu, H., *Sensors and Actuators B: Chemical* **2015,** *216*, 141-149.
31. Zhang, X.-B.; Peng, J.; He, C.-L.; Shen, G.-L.; Yu, R.-Q., *Analytica chimica acta* **2006,** *567*, 189-195.
32. Lu, T.-L.; Tsai, Y.-C., *Sensors and Actuators B: Chemical* **2011,** *153*, 439-444.

33. Rivas, G. A.; Rubianes, M. D.; Rodríguez, M. C.; Ferreyra, N. F.; Luque, G. L.; Pedano, M. L.; Miscoria, S. A.; Parrado, C., *Talanta* **2007,** *74*, 291-307.
34. Chohan, S.; Booysen, I. N.; Mambanda, A., *Polyhedron* **2015,** *102*, 284-292.
35. Ribeiro, F. W. P.; de Souza Lucas, F. W.; Mascaro, L. H.; Morais, S.; da Silva Casciano, P. N.; de Lima-Neto, P.; Correia, A. N., *Electrochimica Acta* **2016,** *194*, 187-198.
36. Chohan, S.; Booysen, I. N.; Mambanda, A.; Akerman, M. P., *Inorganica Chimica Acta* **2016,** *447*, 183-191.
37. Zen, J.-M.; Kumar, A. S.; Chang, M.-R., *Electrochimica acta* **2000,** *45*, 1691-1700.
38. Shumba, M.; Centane, S.; Chindeka, F.; Nyokong, T., *Journal of Electroanalytical Chemistry* **2017,** *791*, 36-48.
39. Monk, P., *Fundamentals of Electroanalytical Chemistry, John Wiley and Sons Ltd., England* **2001**.
40. Maringa, A.; Antunes, E.; Nyokong, T., *Electrochimica Acta* **2014,** *121*, 93-101.
41. Mugadza, T.; Nyokong, T., *Electrochimica acta* **2010,** *55*, 2606-2613.
42. Macdonald, J. R.; Barsoukov, E., *History* **2005,** *1*, 1-13.
43. Ramadoss, A.; Kim, S. J., *Materials Chemistry and Physics* **2013,** *140*, 405-411.
44. Yuan, X.-Z. R.; Song, C.; Wang, H.; Zhang, J., *Electrochemical impedance spectroscopy in PEM fuel cells: fundamentals and applications*. Springer Science & Business Media: 2009.
45. Yoon, S.-B.; Jegal, J.-P.; Roh, K. C.; Kim, K.-B., *Journal of The Electrochemical Society* **2014,** *161*, H207-H213.
46. Khene, S.; Moeno, S.; Nyokong, T., *Polyhedron* **2011,** *30*, 2162-2170.
47. Maringa, A.; Mugadza, T.; Antunes, E.; Nyokong, T., *Journal of Electroanalytical Chemistry* **2013,** *700*, 86-92.
48. Pournaghi-Azar, M.; Sabzi, R., *Journal of Electroanalytical Chemistry* **2003,** *543*, 115-125.
49. Li, F.; Li, R.; Feng, Y.; Gong, T.; Zhang, M.; Wang, L.; Meng, T.; Jia, H.; Wang, H.; Zhang, Y., *Materials Science and Engineering: C* **2019,** *95*, 78-85.
50. Wang, L.; Meng, T.; Sun, J.; Wu, S.; Zhang, M.; Wang, H.; Zhang, Y., *Analytica chimica acta* **2019,** *1047*, 28-35.

51. Razmi, H.; Harasi, M., *Int. J. Electrochem. Sci* **2008,** *3*, 82-95.
52. Manjunatha, R.; Nagaraju, D. H.; Suresh, G. S.; Melo, J. S.; D'Souza, S. F.; Venkatesha, T. V., *Electrochimica acta* **2011,** *56*, 6619-6627.
53. Alam, A. U.; Qin, Y.; Howlader, M. M.; Hu, N.-X.; Deen, M. J., *Sensors and Actuators B: Chemical* **2018,** *254*, 896-909.
54. Kang, X.; Wang, J.; Wu, H.; Liu, J.; Aksay, I. A.; Lin, Y., *Talanta* **2010,** *81* (3), 754-759.
55. de Holanda, L. F.; Ribeiro, F. W. P.; Sousa, C. P.; da Silva Casciano, P. N.; de Lima-Neto, P.; Correia, A. N., *Journal of Electroanalytical Chemistry* **2016,** *772*, 9-16.

CHAPTER FOUR

Electrocatalytic determination of mercury cations at the interfaces of gold electrodes modified with self-assembled monolayers of cobalt phthalocyanines and electropolymerized 3-hexylthiophene films

4.1. Introduction

Elemental mercury and its chemical compounds are environmentally persistent pollutants which have shown to exhibit a wide range of toxicological profiles in humans and animals.[1, 2] In particular, mercury species are neurotoxins which tend to biodistribute to the brain; culminating into various neurodegenerative conditions.[3] Most recently, high concentrations of mercury have been reported in river surface water and sediments of the Umngcwini stream in the Republic of South Africa's Province of KwaZulu-Natal.[4, 5] Consequently, there have been accounts of livestock prematurely dying while quantitative analysis has shown that mercury has bio-accumulated in human hair of some residents living in the rural area along the Umngcwini stream.[6]

In fact, due to the adverse health effects of mercury poisoning, various national and international organisations have set very low mercury concentration limits in the lower ppm range as safety caps for water food commodities and various environment matrices. Mercury concentration above these limits, make the material extremely unsafe for general use. For example, the maximum concentrations of inorganic mercury in drinkable water are set at 2 and 6 μg L^{-1} by the US Environmental Protection Agency and World Health Organization, respectively.[7, 8] Therefore, advanced analytical methods such as atomic absorption spectroscopy (AAS),[9] inductively coupled plasma mass spectrometry (ICP-MS),[10] optical emission

spectroscopy (OES) have been developed for mercury qualitative and quantitative analysis.[11] However, due to high operations costs, the need for highly qualified technicians and time-consuming sample preparation methods; alternatives techniques that are fast, cost effective and portable are imperative for routine analysis.[12]

Electroanalytical techniques have received widespread interest in their potential for routine analysis of heavy metals, especially in the case of mercury.[13-17] Numerous electrochemical methods have been developed in that regard, most of which involves the pre-concentration of the analyte on the CME's interface followed by stripping it off the CME's surface. Anodic stripping voltammetry (ASV) has become the most prominent electroanalytical technique used for the detection of trace metal analysis. Immobilization of nanoparticles and polymeric films onto working electrodes have rendered CMEs with electrocatalytic activities during the stripping electroanalysis of mercury.[18-22]

Furthermore, metallophthalocyanines (MPcs) have been incorporated into conducting thin films for the molecular recognition of various inorganic and organic pollutants.[23-26] These electrochemical sensing capabilities of MPcs have been largely dependent on the redox properties of the central cation and the Pc ring.[27, 28] Current design strategies of MPc-based electrochemical sensors entail the use of substituents that can facilitate the selective detection of analytes.[29] For instance, in a recent research study, a glassy carbon electrode was modified by electrochemical grafting of azide groups to its surface and subsequent clicking of an asymmetric CoPc, *tris*-[(4-benzo[d]thiazol-2-ylthio)-4-(pent-4-yn-1-yloxy)phthalocyaninato)cobalt(II)].[30] This chemically modified GCE could be used to detect mercury in tap water with a high level of accuracy which was largely accounted to the selective binding of mercury ions to the thioether and benzothiazole sulphur atoms of the CoPc.

Herein, SAMs of tetrasubstituted furan or benzothiazole CoPcs onto the surfaces of individual gold working electrodes were formed. Subsequently, the electropolymerization of 3-hexylthiophene (3-HT) chains were conducted onto the CMEs. The resultant CMEs could electrocatalytically detect mercury cations in the presence of other divalent cations as well as in a river water sample while showing robustness and acceptable reproducibility**.** The introduction of the polymeric films is justified due to its inherent higher effective surface areas which can encourage higher analyte pre-concentration onto the respective CMEs while the sulphur atoms on the benzothiazole substituents of the CoPc ensure strong affinitive interactions with the mercury (Hg) ions due to the easy polarizability of S and Hg atoms in accord with the hard and soft acids and bases.[31-33]

4.2. Experimental

4.2.1. Materials

The following starting reagents: 4-nitrophthalonitrile, 2-furanmethanethiol, 2-hydroxymethylbenzothiazole and cobalt(II) chloride were purchased from Sigma-Aldrich. High purity metal salts: mercury(II) sulfate, zinc(II) acetate, lead(II) nitrate and lithium perchlorate as well as the monomer, 3-hexylthiophene (HT) were also attained. Basic catalysts: 1,8-diazabicyclo[*5.4.0*]undec-7-ene (DBU) and potassium carbonate as well as the electrochemical grade supporting electrolyte, tetrabutylammonium tetrafluoroborate ($TBABF_4$), were acquired from the same supplier as analytical grade chemicals and hence, were used without any purification.

Merck SA supplied the analytical, reagent and technical grade organic solvents as well as other materials including phosphorous pentoxide, molecular sieves (4 Å), silicon dioxide for column chromatography and silica plates for thin layer chromatography. To ensure anhydrous conditions during synthetic and selected electrochemical work, dimethylformamide (DMF) was dried and stored over molecular sieves whereas water was ultrapurified with the aid of an Elga Purelab

Ultra system. The derivatized phthalonitrile, 4-(furan-2-methylthio)phthalonitrile (**1**) and its corresponding CoPc, *β*-tetra(2-furanmethylthiophthalocyaninato)Cobalt(II) (**3**) (*viz*. CoPc-fur) were synthesized according to our previously reported work[34] whereas the derivatized 4-(benzothiazole-2-methoxy)phthalonitrile (**2**) has been synthesized and characterized accordingly.[35] After rigorous purification, the macrocyclic metal complexes were kept over P_2O_5.

*4.2.2. Synthetic procedure of tetra-4-(benzothiazole-2-methoxy) phthalocyaninato)Cobalt (II) (CoPc-benz) (**4**)*

A 1:4 mixture of cobalt(II) chloride (0.0279 g, 0.2145 mmol) and 4-(benzothiazole-2-methoxy) phthalonitrile (**2**) (0.252 g, 0.858 mmol) was dissolved in *n*-pentanol together with DBU. The reaction mixture was heated until reflux under nitrogen for 24 hours. After cooling the solution to room temperature, cold *n*-hexane was added to the solution dropwise to induce precipitation. The solution was filtered under reduced pressure and a green precipitate was obtained. The crude product was washed with diethyl ether, ethanol, water and hexane, respectively. The green product was purified *via* column chromatography with $CHCl_3$ and CH_3OH in a 10:1 volume-to-volume ratio. Yield: 23%, FT-IR (υ_{max}/ cm^{-1}): υ(C=N) 1604, *s*; υ(C-O-C) 1230, 1093, *s*. Molecular mass (*m/z*): Calculated: 1224.24. Found: 1223.15 $[M-H]^+$, 1224.16 $[M]^+$, 1225.15 $[M+H]^+$ and 1226.15 $[M+2H]^+$. UV-Vis (DMF, λ_{max} (ε, M^{-1} cm^{-1})): 675 nm (140), 607 nm (120),333 nm (70). CHNS for $C_{64}H_{36}CoN_{12}O_4S_4$(%): Calculated: C, 62.79; H, 2.96; N, 13.73; S, 10.48. Experimental: C, 62.44; H, 2.51; N, 13.69; S, 10.08.

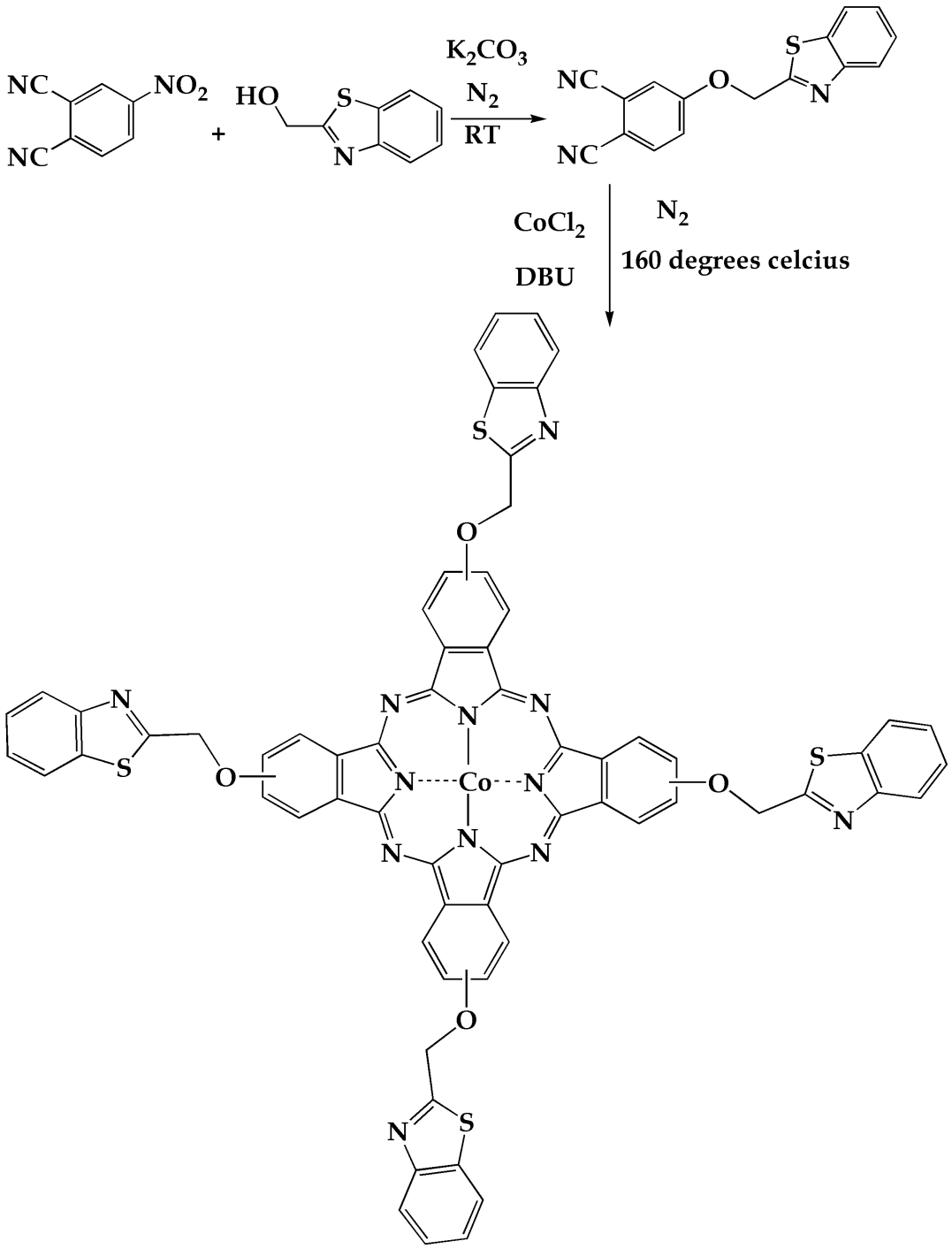

Scheme 4.1: *Synthetic pathway of* ***4****.*

4.2.3. General electrode modification techniques

The gold electrode was cleaned by immersing it thrice in a hot solution of hydrogen peroxide and sulfuric acid in a 1:3 volume-to-volume ratio for short intervals. Thereafter, the bare gold electrode was polished on a Buehler-felt pad using 0.5 μm alumina paste and washed with ultrapure water. Afterwards, the electrode was sonicated in an ultrasonic bath for 5 minutes in acetone and rinsed again with ultrapure water to remove off any residual materials trapped on the electrode surface. Self-assembled monolayers of the respective CoPcs (*i.e.* CoPc-furan or CoPc-benzothiazole) were formed by dipping the gold electrode into a 1 mM DMF solution of the separate CoPcs for 24 hrs. This was followed by electropolymerization of 3-hexylthiophene molecules onto the CMEs, according to a previously reported method.[36]

4.2.4. Anodic stripping voltammetric procedure

A distinct *in-situ* gold modified electrode was immersed in a voltammetric cell containing 5 mL (pH 1.5) of 3.37 x 10^{-3} M Hg(II) solution where Hg(II) was chemically pre-concentrated for 5 minutes in an open circuit under efficient stirring. A cathodic potential of -0.4 V was immediately applied to each CME for 120 s to reduce Hg(II) into elemental Hg atoms. Subsequently, the electrode was transferred into another electrochemical cell containing 5 mL of supporting electrolyte (0.1 M HCl and 0.4 M NaCl). Next, the anodic stripping voltammograms were recorded in an unstirred solution of the supporting electrolyte in the potential range of 0 - 0.4 V with a step potential of 4 mV, modulation amplitude of 50 mV and a frequency of 25 Hz. The electrode surface was regenerated after each measurement by first immersing it in a stirred solution of 0.1 M HNO_3 and then applying a conditioning potential of 0.7 V for a conditioning time of 30 s.

4.3. Results and discussion

4.3.1. *Synthesis and spectral characterization of* **4**

Cyclotetramerization of **2** was conducted in the presence of DBU and $CoCl_2$, under a nitrogen atmosphere which afforded the formation of **4**, see **Scheme 4.1**. Beside exhibiting good solubility in high boiling point aprotic solvents, the metal complex was soluble in volatile organic solvents such as THF and $CHCl_3$. The FT-IR spectrum of **4** showed a disappearance of the medium intensity nitrile stretch found originally at 2225 cm^{-1} in the infrared spectrum of **2**, which supports that the cyclotetramerization reaction has occurred. Furthermore, the FT-IR spectrum of **4** displayed a υ(C=N) signal at 1604 cm^{-1} of the benzothiazole moiety as well as ether stretches υ(C-O-C) found at 1314 and 1231 cm^{-1}. The corresponding strong vibrational bands were observed at 1600 cm^{-1} for υ (C=N), at 1314 and 1255 cm^{-1} for υ (C-O-C), see **Fig. 4.2**. The UV-Vis spectrum displayed characteristics absorptions bands in the regions of 300 - 400 nm and 600 – 700 nm which can be readily assigned to the *B*- and *Q*-bands, respectively, see **Fig. 4.3**. Also, elemental analysis data of **4** was consistent with its calculated elementary composition. Indicatively, TOF-mass spectrometry provided a fragmentation pattern of the metal complex corresponding to selected deprotonated and protonated species as well as the molecular ion peak, see **Fig. 4.4**.

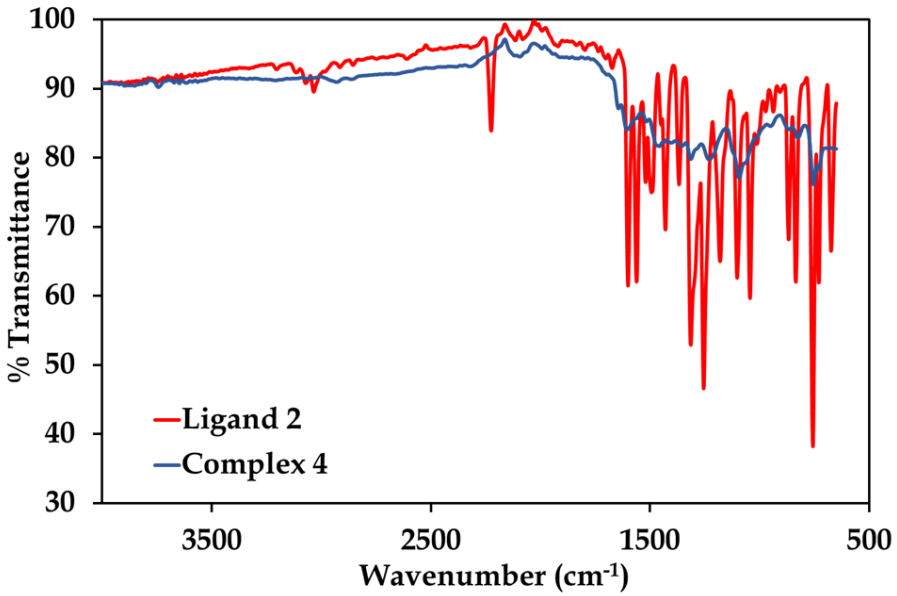

Fig. 4.2: *Overlay IR spectra of ligand* **2** *and complex* **4**

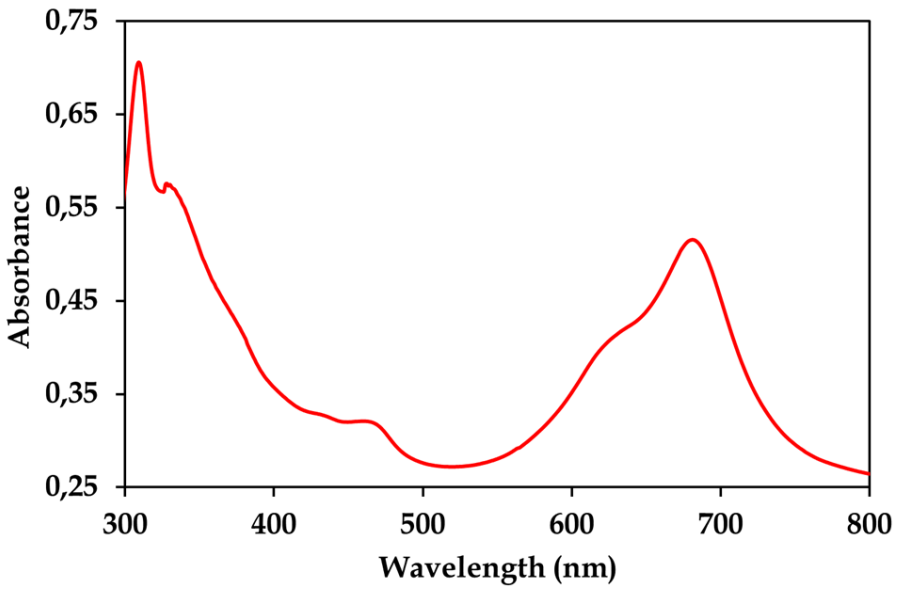

Fig. 4.3: *UV-Vis spectrum of complex* ***4***

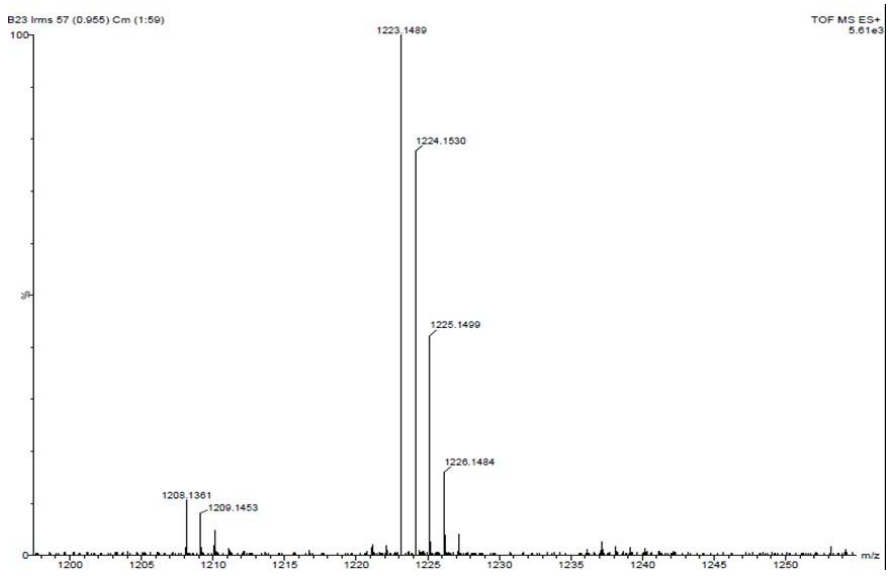

Fig. 4.4: *Low resolution TOF-mass spectrum of* ***4***

4.3.2. Scanning electron microscopy (SEM) and energy dispersive x-ray (EDX) analysis

Scanning electron microscopy (SEM) was used to elucidate structural features of the SAMs. SAMs formation were achieved by immersing the gold-coated glasses into respective 2.0 molar concentrated solutions of the individual CoPcs for 72 hrs to facilitate good SAMs formation and better coverages. Visually, it is apparent that the bare gold coated glass has a smooth morphology while semi-crystalline materials are observed on the SAM-modified glasses, see **Fig. 4.5**(**A**) - (**C**). Of particular interest, the SEM micrographs of the glasses containing SAMs illustrate clusters which clearly support the intrinsic aggregation of their individual molecules.[37] The EDX spectra revealed the presence of an elemental composition of Co, Au, S, N, C and O for both of the SAM-modified glasses which ascertain the adsorption of the respective CoPcs onto the gold substrates, see **Fig. 4.5**(**D**) and (**E**). In contrast, only Au was detected in the EDX spectrum of the bare gold-sputtered glass.

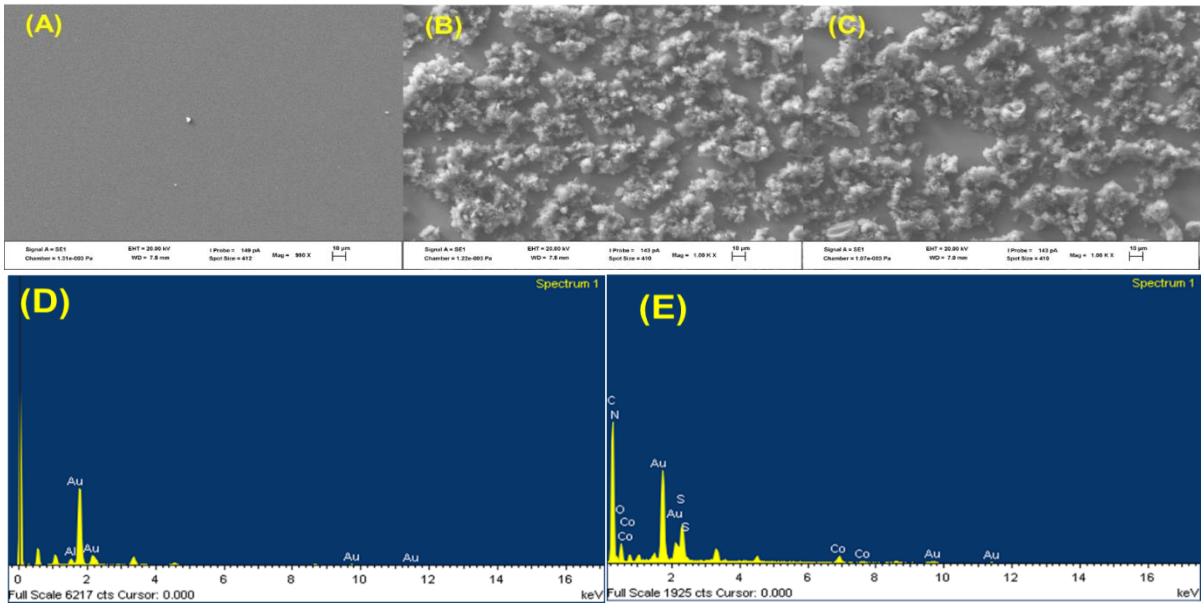

Fig. 4.5: *(**A**) Bare gold-sputtered glass, (**B**) SAM-**3** gold-sputtered glass and (**C**) SAMs-**4** gold-sputtered glass, (**D**) EDX spectrum of bare gold-sputtered glass, (**E**) EDX spectrum for SAMs-**3** gold-sputtered glass.*

4.3.3. Electrocatalytic responses of chemically modified electrodes (CMEs)

Fig. 4.6 illustrates the differential pulse anodic stripping voltammograms (DPASVs) of 3.37 x 10^{-3} M Hg(II) using the bare Au electrode and the respective CMEs in 0.1 M HCl and 0.4 M NaCl as a supporting electrolyte. The DPASV of each modified gold electrode displays two peaks which are observed in the regions of *ca* 0.05 and 0.25 V, respectively. Similar trends have been reported for electrochemical detection of mercuric ion in various acidic media by squarewave anodic stripping voltammetry, where a coalesced peak is observed that is accounted to elemental mercury being stripped off to its oxidation (+I) and (+II).[38] An additional peak occurred due to the oxidation of anions which are adsorbed on the surfaces of the different working electrodes. Consequently, the 1st peak is due to a mixture of oxidative stripping processes of the metal to its Hg_2^{2+} and Hg^{2+} cations while the 2nd peak is attributed to adsorption of anions to the CMEs. DPASVs of the background electrolyte (HCl and NaCl) solution provided insight into the native nature of the peak. It is evident that the chloride ions underwent oxidation, see **Fig. 4.7**. The standard oxidation potential of chloride ion to chlorine gas is known to be approximately 1.36 V. In fact, Patil *et al.* reported oxidation of chloride ion on a platinum rotating electrode in the vicinity of 1.80 V.[39] Later, it will be shown that the 2nd peak is only apparent at elevated concentrations of the mercury salt and for this reason, the 2nd peak found in the DPASVs are not discussed.

Noticeably, the bare gold electrode induced a wide and intense peak whereas the SAM-modified electrode produced a minute peak accompanied by a shoulder which indicate that electrodeposition of mercury occurred more readily on the former than the latter CME. The asymmetry and broadness of the first oxidative redox peak produced from the bare Au electrode point to the two metal-based oxidative processes overlapping. Upon using the Poly(3-HT) CME, a sharp first peak with a tailing shoulder was rendered. Moreover, the higher oxidation peak current could be attributed to the favourable coordination affinity between mercury and the sulphur

atoms of the polymeric film; leading to a higher concentrations of mercury cations being anodically stripped off the CME surfaces.

The SAMs-**3**|Poly(3-HT)-Au electrode proved to be the most favourable CME based on its better resolved and dominating first oxidation peak current attributable to the electrocatalytic synergy between the MPc-based SAM and the polymeric film. The synergism between the constituents' catalytic effects is promoted by the sulphur atoms of both the metal complex and the polymer which allow for a combined higher surface-active area and an improved cathodic deposition of Hg(II). Subsequently, the stripping process of Hg(0) to Hg(I) and Hg(II) is electrocatalyzed by the Co(II)/Co(III) redox couples of the respective CoPcs since these redox potentials occur in the vicinity as the individual Hg^{+}, Hg^{2+} peaks.[34] However, for the Au electrode where the electropolymerization was first performed followed by SAM formation, sluggish responses were produced which is tentatively ascribed to the SAM blocking some sulphur atoms of the polymeric film; resulting in a depreciated uptake of Hg. Similar electroanalytical trends were observed when using **4**. Of all the tested CMEs derived from the SAMs of 4, the SAMs-**4**|Poly(3-HT) Au electrode yielded the best $\mathbf{I}_{pa}$ and $\mathbf{E}_{pa}$ data, see **Fig. 4.8.**

Table 1: *Stripping anodic currents and potentials (V vs Ag|AgCl) when using the bare Au electrode and the modified gold electrodes containing the respective CoPcs.*

	Complex 3		**Complex 4**	
Au Electrode	$\mathbf{I}_{pa}$ (μA)	$\mathbf{E}_{pa}$ (**V**)	$\mathbf{I}_{pa}$ (μA)	$\mathbf{E}_{pa}$ (**V**)
Bare	250	0.020	234	0.0159
SAMs	160	0.012	473	0.119
SAMs|Poly(3-HT)	400	0.032	600	0.087
Poly(3-HT)	320	0.040	497	0.091
Poly(3-HT)|SAMs	260	0.047	366	0.051

Where I_{pa} :oxidation peak currents of 1st redox signal

E_{pa} : oxidation peak potentials of 1st redox signal

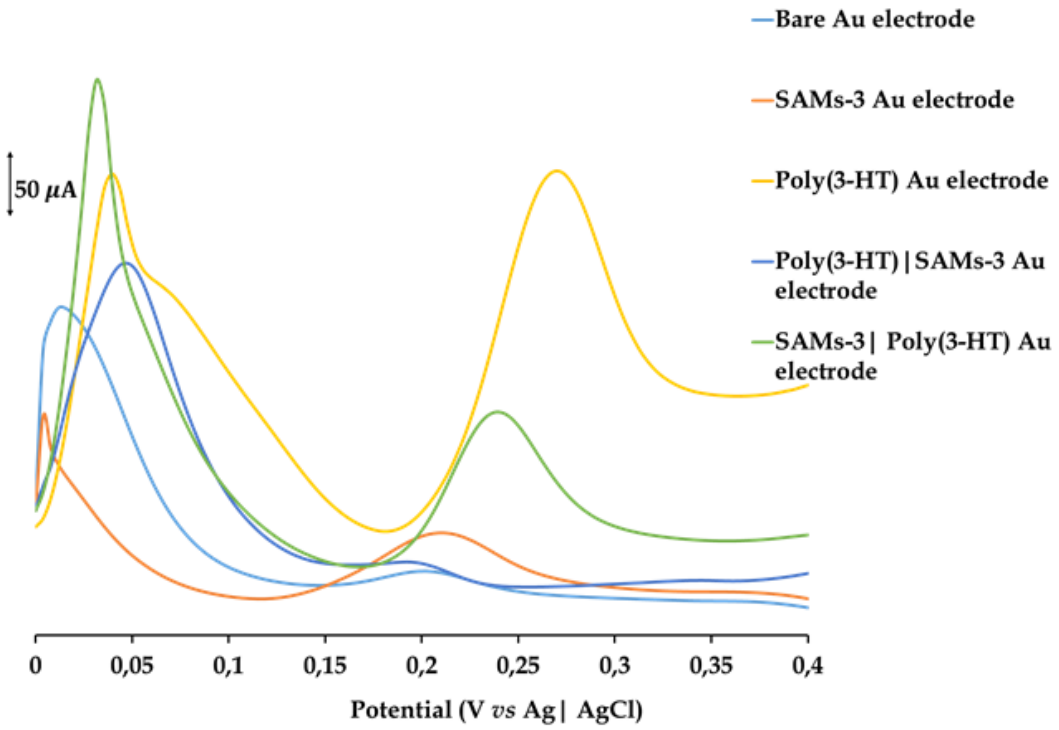

Fig. 4.6: *DPASVs obtained using bare, SAMs-**3**, Poly(3-HT), Poly(3-HT) | SAMs-**3** and SAMs-**3** | Poly(3-HT)-Au electrodes in aqueous solution of 3.37 x 10^{-3} M Hg^{2+} prepared in 0.1 M HCl and 0.4 M NaCl.*

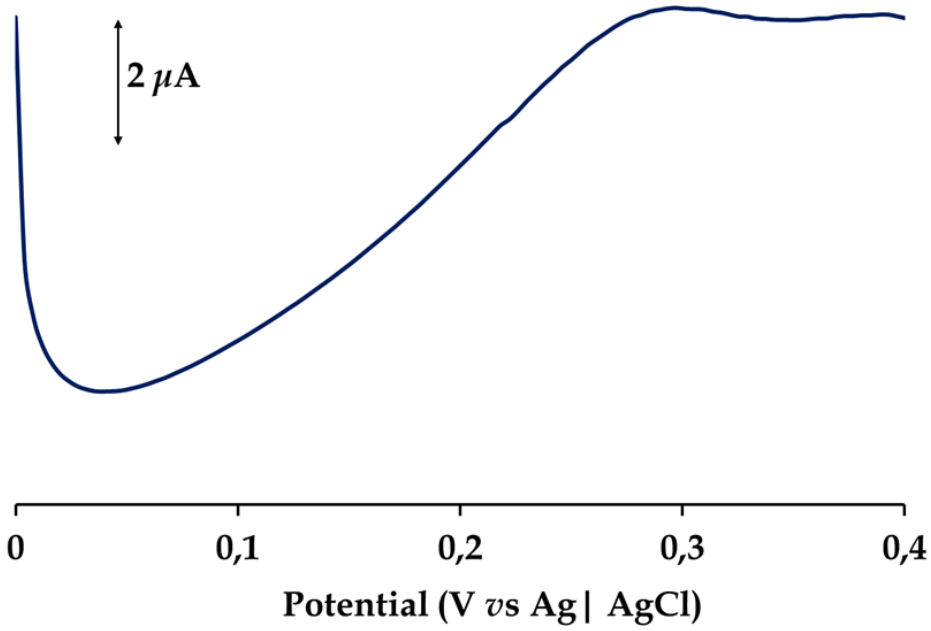

Fig. 4.7: *Differential pulse anodic stripping voltammogram (DPASV) of the electrolyte solution*

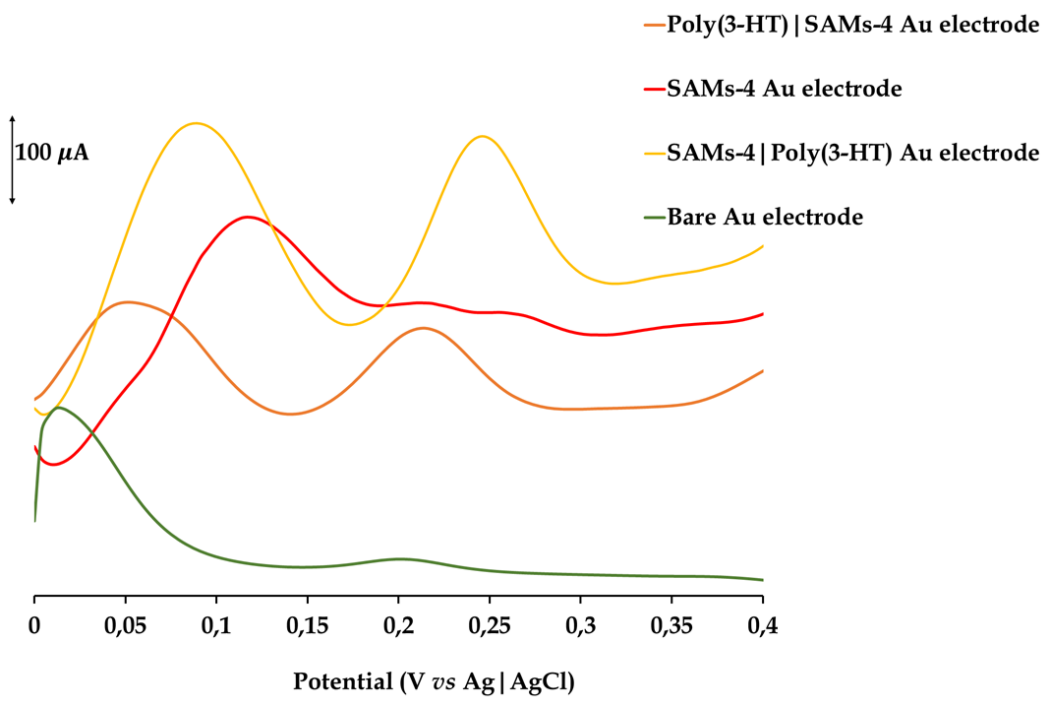

Fig.4.8: *Differential pulse anodic stripping voltammograms (DPASVs) obtained using bare, SAMs-**4**, Poly(3-HT), Poly(3-HT) | SAMs-**4** and SAMs-**4** | Poly(3-HT) Au electrodes in aqueous solution of 3.37x10-3 M Hg^{2+} prepared in 0.1 M HCl and 0.4 M NaCl*

4.3.4. Characterization of modified electrodes

4.3.4.1. Self-assembled monolayer (SAM) characterization

The dual SAM- and electropolymerized-modified gold electrodes were probed in various redox probes. Firstly, **Figs. 4.9 (A)** and **(B)** show the CVs produced using the SAMs-**3**/**4** | Poly(3-HT) CMEs and unmodified Au electrodes in 1 mM Na_2SO_4 prepared in a pH 4 buffer solution. It is apparent from the CVs that there is a sharp peak at *ca* 0.169 V for the bare Au electrode which is the result of the exposed gold undergoing redox reactions. However, when using the CMEs, negligible peak currents were obtained at much higher positive potentials, which emphasizes the degrees of impermeability for the SAM-modified Au electrodes due to the ubiquitous ions of the supporting electrolyte; thereby confirming the SAMs formations.

Figs. 4.10 (A) and (**B**) show the cyclic voltammograms (CVs) obtained using the bare Au electrode and the SAMs-**3**/**4**|Poly(3-HT) CMEs in 1 mM $CuSO_4$ prepared in pH 4 buffer solution. The underpotential deposition (UPD) of Cu on the bare Au electrode easily formed at 0.22 V *vs* Ag|AgCl. However, this corresponding redox process was significantly inhibited by the CMEs which supports the formation of SAMs on the substrate.

The ion barrier factor (Γ_{IBF}) can be used to evaluate the compactness of the SAM bonded to a substrate's interface. In particular, an ion barrier factor of 1 indicates that the SAM covers the entire surface area of the substrate and that no exposed substrate is available where a selected redox probe can undergo redox reactions. Hence, a SAM with an ideal ion barrier is considered as an impermeable film for the redox probe. The ion barrier is calculated by comparing the total current under the redox peak of a SAM-modified electrode [$I_{pa(SAM)}$] to that of the bare electrode [$I_{pa(Bare)}$], **Eq.** (**4**). Ion barrier values of 0.97 and 0.98 were attained which are close to 1, indicating nearly full coverages of the corresponding gold surfaces by the respective SAMs:[40]

$$\Gamma_{IBF} = 1 - \frac{I_{pa}(SAM)}{I_{pa}(Bare)} \qquad (4)$$

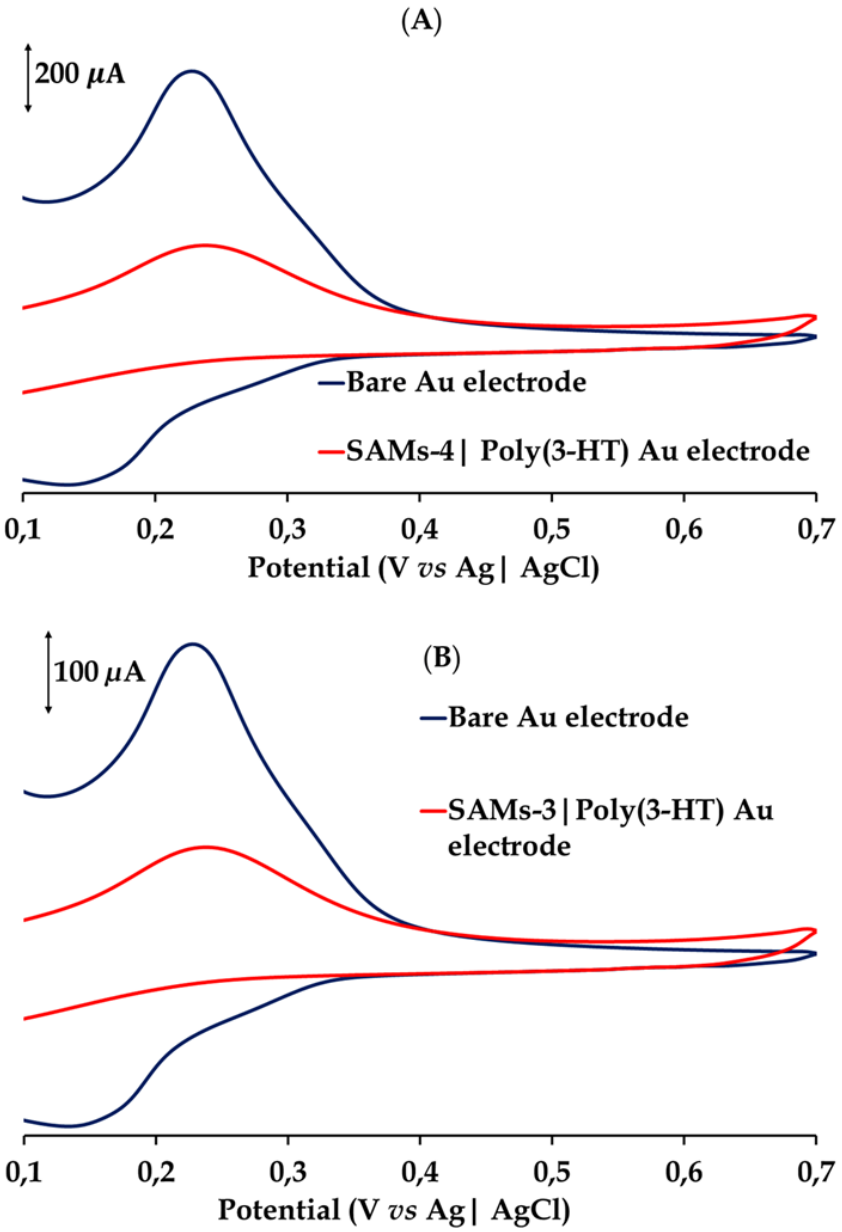

Fig. 4.9: *(**A**) and (**B**) CVs of SAM-**4/3** | Poly(3-HT)-Au electrode and the unmodified Au electrode recorded in 1 mM $CuSO_4$ in pH 4 buffer solution.*

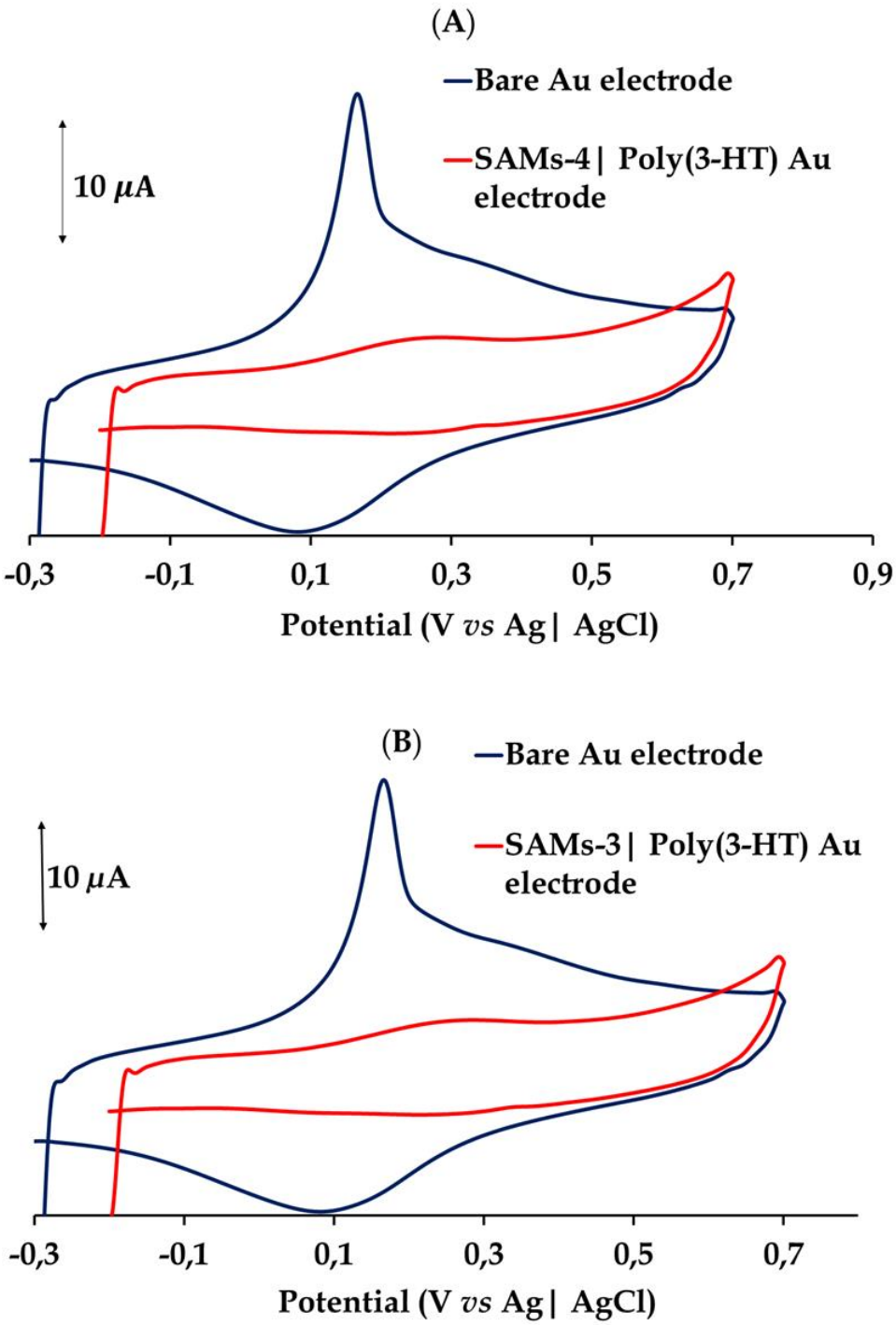

Fig. 4.10: *(**A**) and (**B**) CVs of SAM-**4/3** | Poly(3-HT)-Au electrode and the unmodified Au electrode recorded in 1 mM Na_2SO_4 in pH buffer solution.*

4.3.4.2. Effective surface area and surface coverage

The effective surface area of a CME plays a pivotal role in addressing the electrocatalytic deficiencies of its corresponding bare working electrode where the electron-mediating thin film of a CME typically promotes better sensitivity of the analyte's redox signals.[41] **Figs. 4.11** (**A**) and **4.12** (**A**) show respective CVs at different scan rates using the SAM-**4**|Poly(3-HT) and SAM-**3**|Poly(3-HT) Au electrodes in a 5 mM solution of $K_3[Fe(CN)_6]$ prepared in 0.1 M KCl. The individual effective surface areas of the CMEs were calculated using the Randles-Sevcik equation,[42] **Eq. 3**:

$$I_{pa} = 2.69\ x\ 10^5 A D^{1/2} n^{3/2} v^{1/2} C \qquad (\mathbf{5})$$

where A is the effective surface area, D is the diffusion coefficient of $K_3[Fe(CN_6)]$, v is the scan rate, C is the bulk concentration of $K_3[Fe(CN)_6]$, n is the number of electrons transferred (n = 1). A plot of square root of scan rates *vs* oxidation peak currents are shown in **Figs. 4.11**(**B**) and **4.12**(**B**)**,** the slopes of the $I_{pa}\ vs\ v^{1/2}$ plots was used in **Eq. 5** to calculate the effective surface areas. The relating effective surface areas were found to be 2.656 cm^2 and 2.847 cm^2 for the SAM-**4** |Poly(3-HT) and SAM-**3** |Poly(3-HT) Au electrodes, respectively. These values are approximately five times higher than the area (0.503 cm^2) of the bare Au electrode. These drastic increases in surface areas upon modification are attributed to the synergetic effects of both the polymer and the individual SAMs, whereby each contains sulphur atoms leading to more accessible sites for the coordination of the heavy metal pollutant.

The surface coverage (Γ)of each CME was equally evaluated and calculated as the moles per unit area. Using the effective surface areas obtained using equation (**5**) and the total charge under the oxidation peak currents, the surface coverages were calculated using **Eq.** (**6**):[42]

$$\Gamma = \frac{Q}{nFA} \qquad (\mathbf{6})$$

where Γ is the surface coverage, *n* is the number of transferred electrons, F is the Faraday constant and A is the effective surface. Respective values of 6.4 x 10^{-9} mol cm^{-2} and 1.02 x 10^{-9} mol cm^{-2} for the SAM-**4**|Poly(3-HT) and SAM-**3**|Poly(3-HT) Au electrodes were obtained. These surface coverage values are sufficiently higher than the 1x10^{-10} mol cm^{-2} which correspond to a Pc molecule lying flat onto the surface of the substrate.[43] In addition, a better surface coverage translates into an increased number of electrocatalytic sites which leads to enhanced sensitivity.

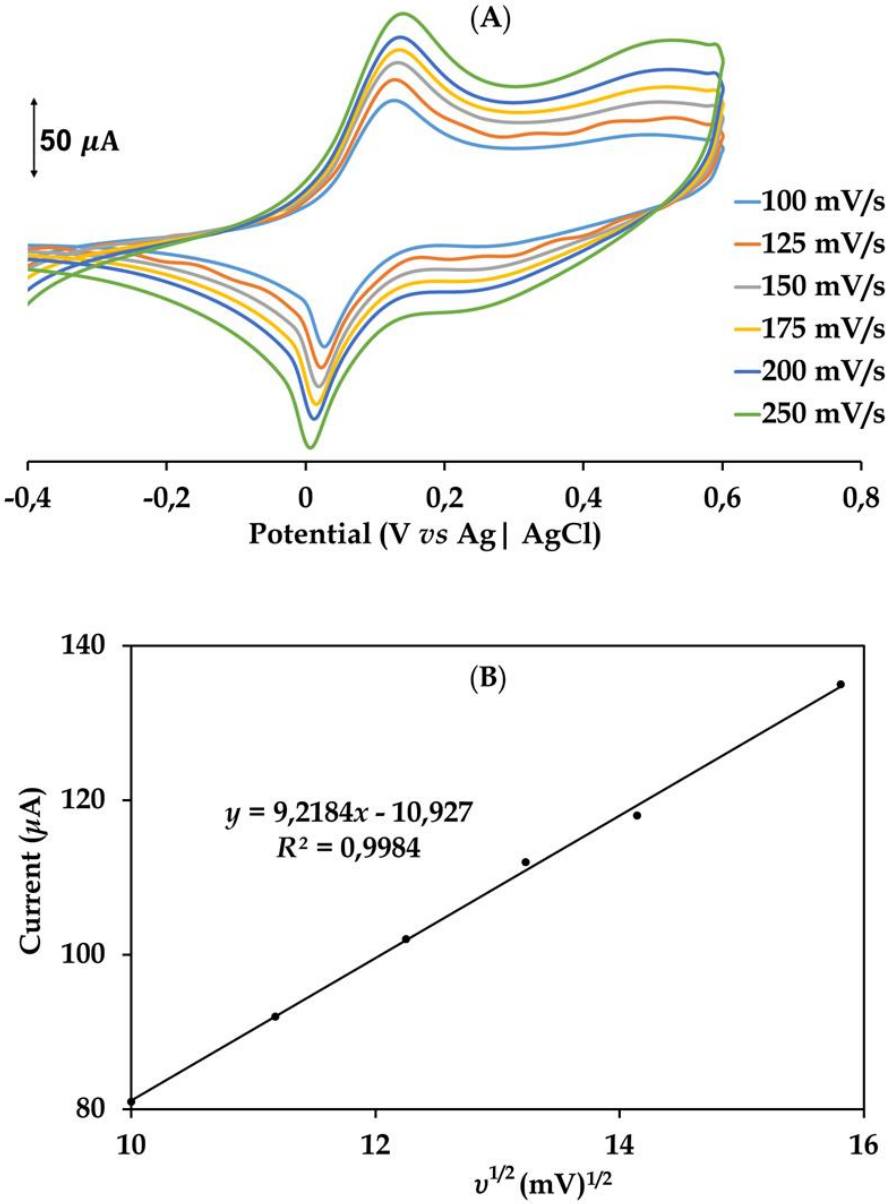

Fig. 4.11: *(**A**) CVs curves in aqueous solution of 5.0 mM $K_3[Fe(CN_6)]$ containing 0.1 M KCl(aq) using the SAM-**4**|Poly(3-HT)-Au electrode at different scan rates (100, 125, 150, 175, 200 and 250 mV/s). (**B**) Plot of I_{pa} vs square root of scan rate.*

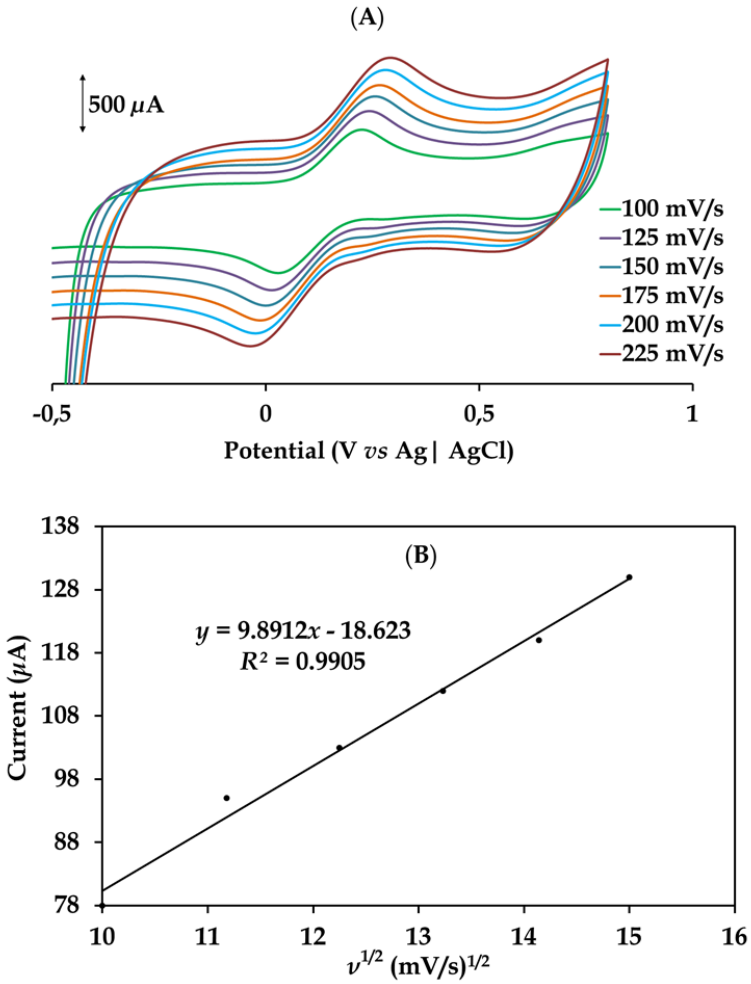

Fig. 4.11: *(**A**) CVs curves in aqueous solution of 5.0 mM $K_3[Fe(CN_6)]$ containing 0.1 M KCl(aq) using the SAM-**3** | Poly(3-HT)-Au electrode at different scan rates (100, 125, 150, 175, 200 and 225 mV/s). (**B**) Plot of I_{pa} vs square root of scan rate*

4.3.4.3. Electrochemical impedance spectroscopy (EIS)

EIS data were gathered to provide more understanding into the nature of the electron transfer behaviors of the CMEs.[44] A frequency range of 0.1 Hz to 100 kHz was applied when the EIS experiments were conducted in a standardized aqueous solution of potassium ferricyanide in 0.1 M KCl as a supporting electrolyte. The EIS data was expressed as a Nyquist plot which offer insights into the impedance across the electrode, immobilized thin films and electrolyte, see **Fig. 4.12**.

Furthermore, the Nyquist plots attained charge transfer resistance (R_{ct}) which is estimated as the diameter of the semi-circle appearing at higher frequencies while the Warburg impedance (Z_w) occurs at lower frequencies. The modelled Randles equivalent circuit for all the electrodes contained the following circuit elements: electrolyte resistance (R_s), charge transfer resistance (R_{ct}), constant phase element (CPE) and the Warburg impedance (Z_w). The inclusion of the non-ideal capacitor, the CPE is motivated by the surface roughness of both the bare and the CMEs. The EIS data was validated by the low errors attained between the experimental and fitted data.

The R_{ct} values were found to be 690 Ω and 586 Ω for the respective SAMs-**4**|Poly(3-HT) and SAMs-**3**|Poly(3-HT) Au electrodes. Contrary to the R_{ct} values of the CMEs, the bare gold electrode has a significantly higher R_{ct} value of 1.38 kΩ, emphasizing the faster electron exchange rates of the CMEs. The *n*-values are in the range of 0.61 - 0.86 ($n < 1$) which show the non-capacitive nature of the electrodes.[45] In fact, the Bode plots (see **Fig. 4.13**) concurs with Nyquist plots in that the CMEs and the bare electrode are non-capacitors given by the phase shifts angles which are less than 90^0.

Table 2: *Summary of EIS data collected in a 5 mM $[Fe(CN)_6]^{3-/4}$ using the bare and CMEs. Error values are shown in brackets.*

Au electrode	R_s (Ω)	R_{ct} (Ω)	Z_w (*m*S)	CPE (*m*S)	^an
Bare	82.9 (0.65)	1380 (3.4)	0.635 (3.4)	0.063(4.0)	0.852
SAMs-3|Poly(3-HT)	78.6(0.86)	263(5.5)	0.383(1.2)	0.110(12)	0.681
SAMs-4|Poly(3-HT)	77.6 (0.74)	690 (3.4)	0.726 (2.0)	0.138(4.8)	0.613

[^an] is the exponent related to the depression angle.

Values in brackets are percentage errors obtained from fitting the experimental Nyquist plots

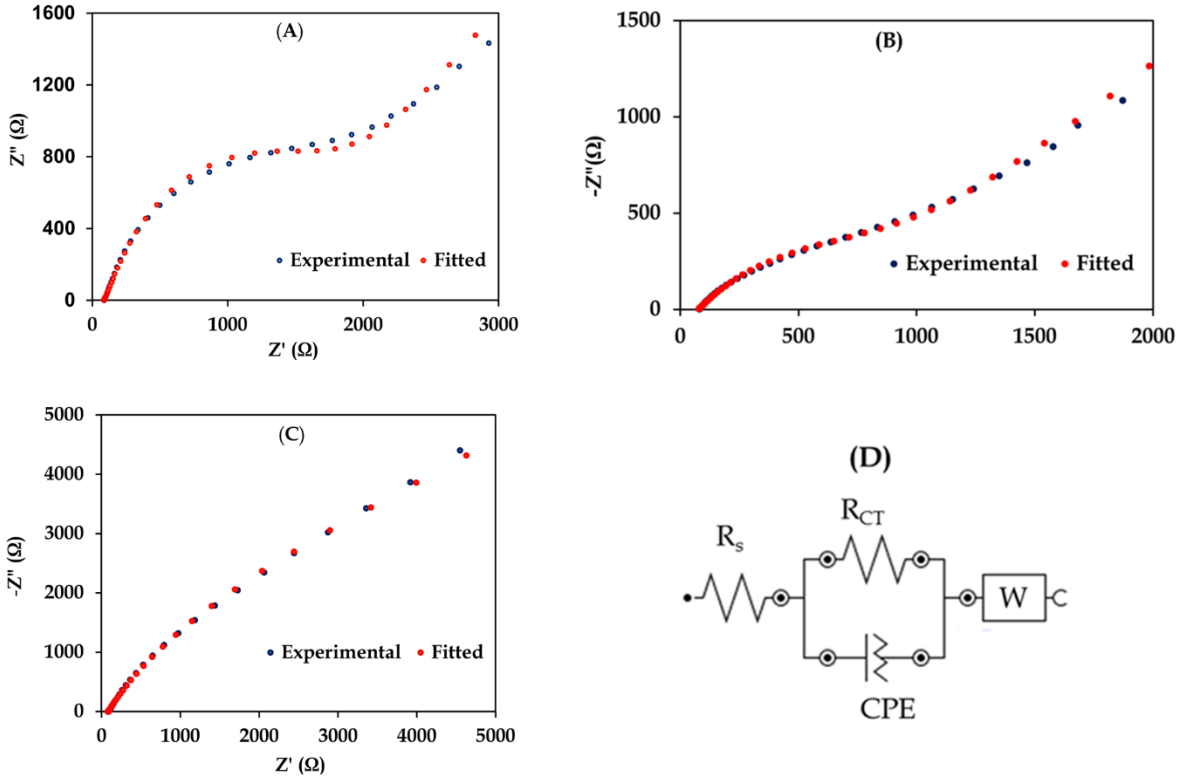

Fig. 4.12: *Nyquist plots attained in solution of 5 mM [Fe(CN)$_6$] prepared in PBS using (**A**) the bare, (**B**) the SAMs-**4** | Poly(3-HT) and the (**C**) SAMs-**3** | Poly(3-HT) Au electrodes. (**D**) Equivalent circuit used to fit the EIS data.*

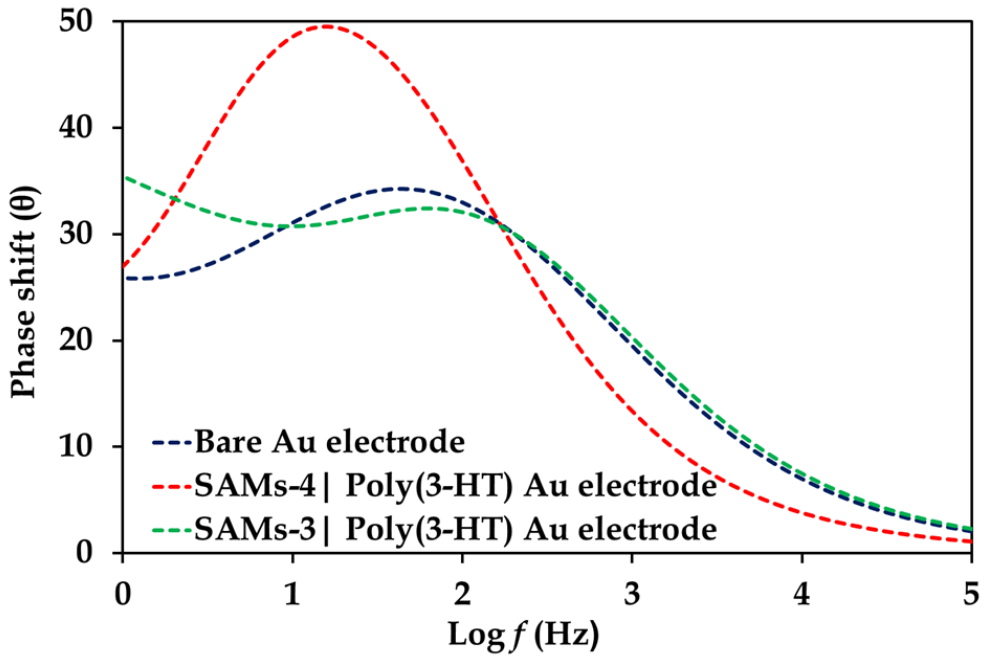

Fig. 4.13: *Bode plots generated with the respective CMEs*

4.3.5. Voltammetry studies

Electrochemical properties of **4** were investigated using CV and SWV techniques in a $TBABF_4$/DMF medium, using a platinum working electrode, see **Figs. 4.14** (**A**) and (**B**). CV and SWV measurements showed four redox couples that are assigned to metal-centred and Pc ring-based redox processes. The redox couples **II** and **III** displayed a narrower peak to peak separations values (ΔE values) compared to that of the standard ferrocene ($\Delta E = 100$ mV) using a Pt working electrode and the same experimental conditions. Therefore, redox processes **II** and **III** are quasi-reversible whereas redox couples **I** and **III** are respective irreversible reductive and oxidative processes.[46] The derived electrochemical data is shown in **Table 3** and is in agreement with previously reported data. Hence, the redox couples **I** to **IV** were assigned according to literature trends, see **Table 3.** Due to л – л stackings between MPc monomers, aggregation is a common phenomenon which gives rise to additional peaks within voltammograms of **4**. Linear relationships were attained in all the

Randles-Svcek plots of each redox couple; indicating that the mass-transport occurs entirely *via* diffusion, see **Fig. 4.15**.[47]

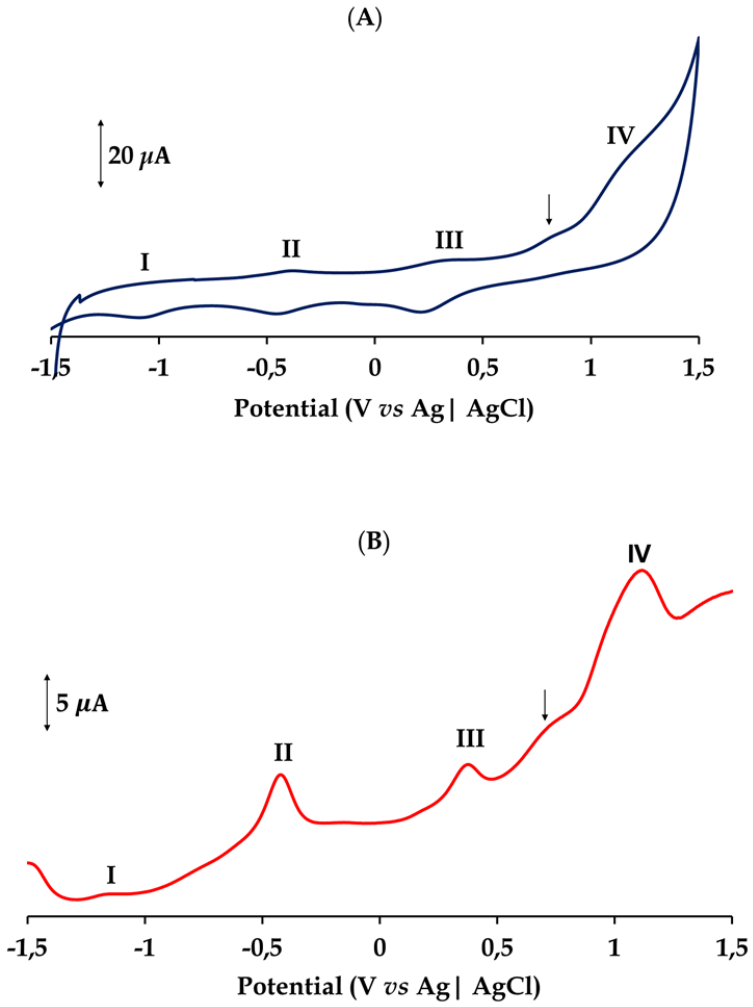

Fig. 4.14: *CV (**A**) and SWV (**B**) of **4** at 100 mV/s. The arrows indicate aggregation peaks*

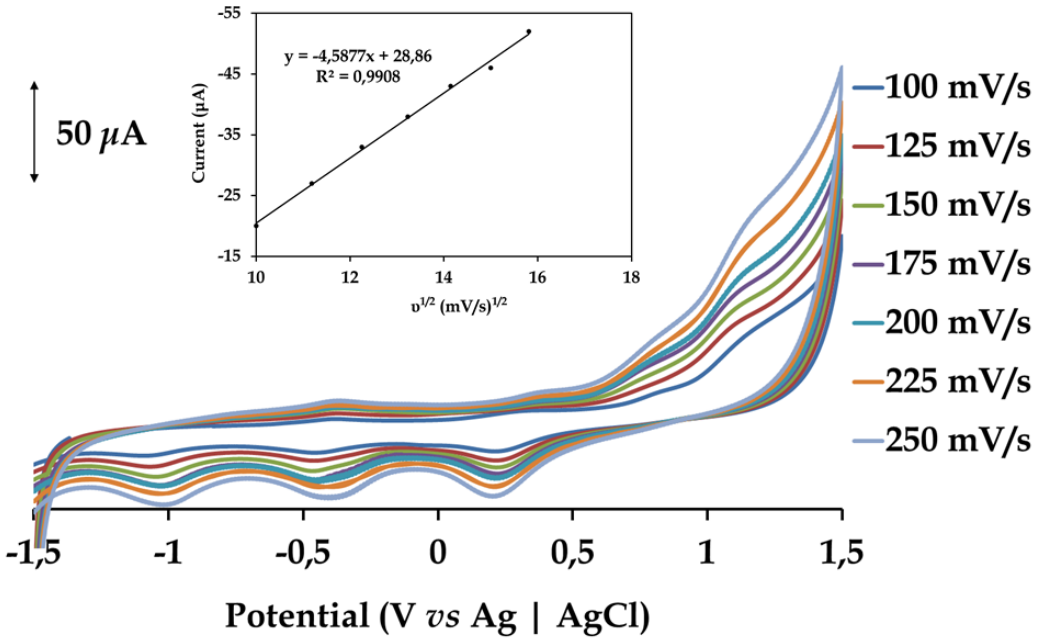

Fig. 4.15: *Overlays CV of 4 at incrementing scan rates. The insert shows a Randles-Svcek plot of redox couple IIIwhere the Ipc is plotted against the square root of scan rate*

Table 3: *Electrochemical data of CoPc-benzothiazole in comparison with other CoPcs with substituents containing sulphur atoms.*

CoPc (Solvent)	**Parameters**	**IV Pc^{-2}/Pc^{-3}**	**III Co^{II}/Co^{III}**	**II Co^{I}/Co^{II}**	**I Pc^{-2}/Pc^{-1}**	**References**
CoPc-benz (DMF)	E (V)	E_{pa} = 1.14	$E_{1/2}$= 0.28	$E_{1/2}$= -0.42	E_{pc} = -1.09	This work
	$\Delta E_p(mV)$	-	91	70	-	
CoPc-4-methoxyphenylthiazole-2-thio (DMSO)	$E_{1/2}$ (V)	-	0.62	-0.27	-1.02	[48]
	$\Delta E_p(mV)$	-	106	70	90	
CoPc-2-methyl-5-benzothiazole (DMSO)	$E_{1/2}$ (V)	1.04	0.53	-0.30	-1.23	**[49]**
	$\Delta E_p(mV)$	-	68	66	70	
CoPc-hydroxyethyl-thio (DMSO)	$E_{1/2}$ (V)	1.00	0.43	-0.37	-1.29	[50]
	ΔE_p(mV)	-	60	70	72	
CoPc-dimethoxyphenylthio (DMSO)	$E_{1/2}$ (V)	1.00	0.28	-0.52	-1.48	[51]
	$\Delta E_p(mV)$	-	65	100	72	

4.3.6. Optimization of the instrumental and chemical parameters

4.3.6.1. Supporting electrolyte

Different electrochemical parameters were studied in order to assess under which optimization conditions the highest sensitivity is attained for the first oxidation peak and therefore Hg_2^{2+}, Hg^{2+} determination. As previously reported,[52] hydrochloric acid had been found to be the ideal supporting electrolyte for mercury electrocatalysis. The rationale behind this is that mercuric chloro complexes form in solution, which in return promotes the oxidation of mercury at lower stripping oxidation potentials as well as minimizing background currents while enhancing the reduction peak currents.[53, 54] Jonavoski and Hrastnik reported that adding NaCl also shifted the Hg (II) signal towards negative potentials, hence an electrolyte solution containing 0.1 M HCl and 0.4 M NaCl was chosen as the best electrolyte for further investigations.[52]

4.3.6.2. Accumulation potential

The deposition potential was investigated in the range of -0.1 to +1.0 V. The stripping signal increased slightly as the deposition potential became more negative in the range of -0.1 to -0.4 V peaking at -0.4 V. At more cathodic potential, the signal started dissipating due to the competing hydrogen evolution reaction. During application of a high positive potential of +1.0 V, the second lowest peak current was attained, see **Fig. 4.16** (**A**). Hence, a deposition potential of -0.4 V was chosen as an optimum accumulation potential for further electrochemical experiments for SAMs-**3**|Poly(3-HT) Au electrode. Similar trends were observed for the SAMs-**4**|Poly(3-HT) gold electrode where a deposition potential of -0.2 V provided the superior stripping currents and was chosen for further electroanalytical experiments, see **Fig. 4.17** (**A**).

4.3.6.3. Accumulation time

Accumulation time was investigated using each of the *in-situ* modified gold electrodes as depicted in **Figs. 4.16 (B)** and **4.17** (**B**) in the range of 0 – 220 s. The stripping signal increased steadily before reaching a maximum at 120 and 180 s for SAMs-**3**|Poly(3-HT) and the SAMs-**4**|Poly(3-HT) gold electrodes, respectively. At prolonged accumulation periods, the peak currents decreased substantially which could be caused by the saturation of the binding sites. Thus, individual deposition times of 120 and 180 s were chosen for subsequent analysis.

4.3.6.4. The effect of pH

The effect of pH on the stripping currents for the adsorbed metal were studied in the pH range of 1 - 8. It is well documented that the pH of the buffer solution plays a significant influence on the stripping current of the metal ion of interest.[55] As seen in **Figs. 4.16** (**C**) and **4.17** (**C**), the responses gradually decreased as the pH increased. The best pH value was found to be 1.5 and used for further investigations. Evidently, this is in accordance with the Latimer diagram of mercury in acidic media which show that mercury cations are thermodynamically stable at low pH.

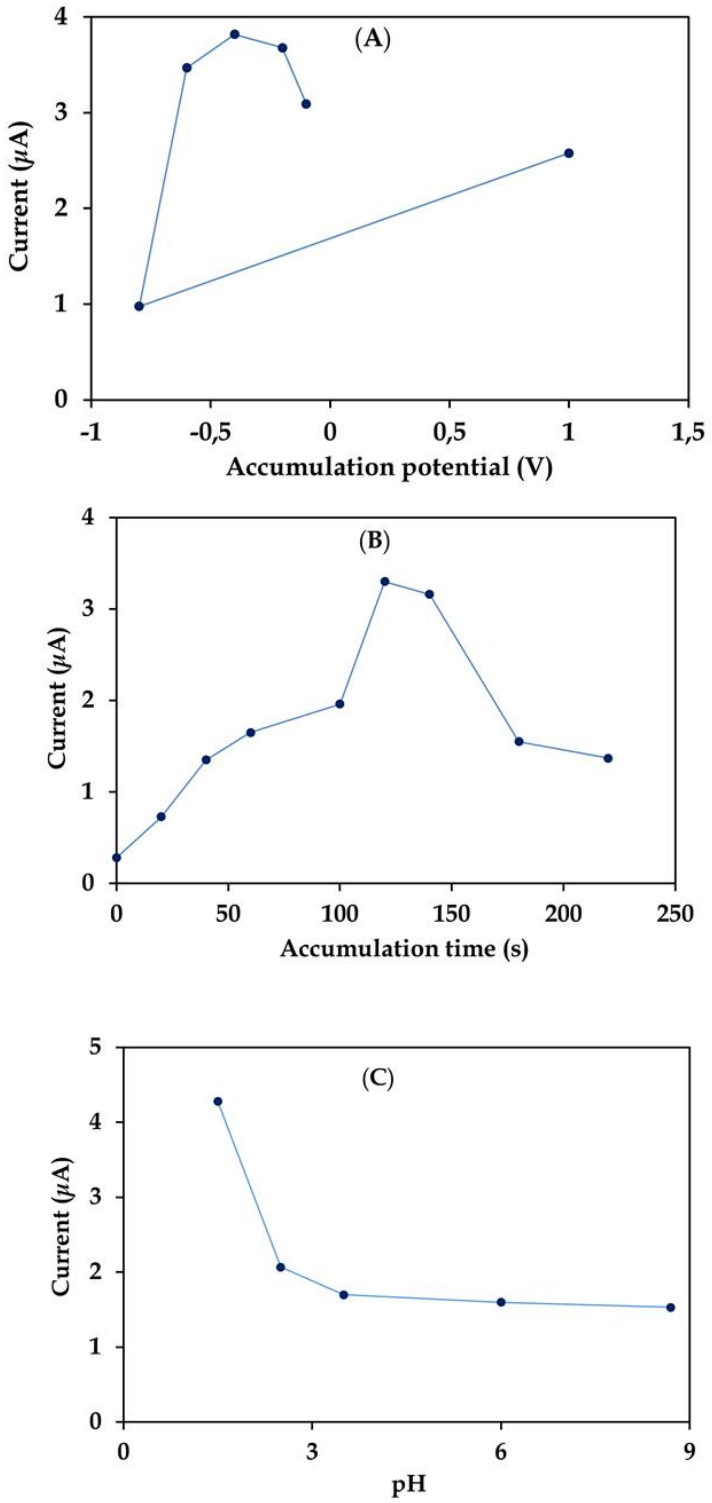

Fig. 4.16: *Optimization parameters of the SAMs-**4** | Poly(3-HT) on the DPASV peak currents of 3.37 x 10^{-3} M Hg (II) in 0.1 M HCl and 0.4 M NaCl: (**A**) accumulation potential, (**B**) accumulation time and (**C**) pH studies.*

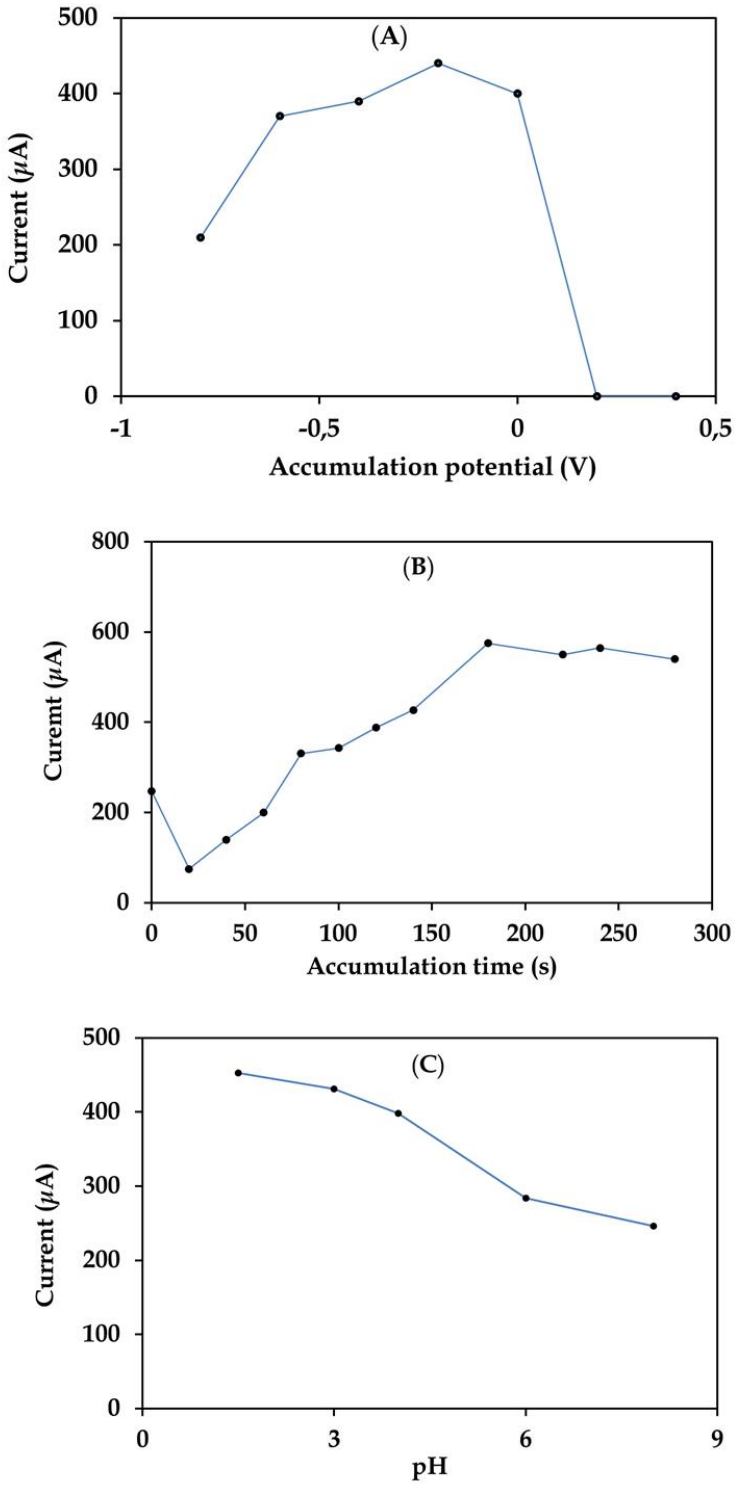

Fig. 4.17: *Optimization parameters of the SAMs-**3** | Poly(3-HT) on the DPASV peak currents of 3.37 x 10^{-3} M Hg (II) in 0.1 M HCl and 0.4 M NaCl: (**A**) accumulation potential, (**B**) accumulation time and (**C**) pH studies.*

4.3.7. Analytical performances for detection of Hg(I) and -(II) cations

DPASV responses of Hg(II) standardized solutions were monitored using the SAM-**3**|Poly(3-HT) or the SAM-**4**|Poly(3-HT) Au electrodes. Linear responses were obtained in the concentration ranges of 4.21 x 10^{-5} – 3.37 x 10^{-3} M and 3.37 x 10^{-4} – 3.37 x 10^{-3} M, respectively. Shifts in the stripping potentials were observed despite rigorous pre-conditioning between each accumulation step. The latter was accounted to supporting electrolyte effects where the mercury stripping potentials can shift as the chloride concentration of the sample solution is varied.[38] In addition, nearly reproducible DPASVs were attained for the blank solution between each electrocatalytic run. Furthermore, the broadness of the peaks is ascribed to $Hg^{2+}$and Hg_2^{2+} being collectively stripped off the corresponding CMEs. The respective voltammograms and their subsequent calibration graphs are shown in **Figs. 4.18** and **4.19**. Linear responses were obtained with regressions of R^2=0.9906 and R^2=0.9781 for the SAMs-**3**|Poly(3-HT) and SAMs-**4**|Poly(3-HT) Au electrodes, respectively. Calibrations curves were expressed by the following equations:

$$I = 112558\,M + 47.565,\ r^2 = 0.9936 \quad (\mathbf{6})$$

$$I = 109647\,M + 57.921\,,\ r^2 = 0.9683 \quad (\mathbf{7})$$

The limit of detection (LOD) values was determined using the equation LOD = $3s_x/m$, where s_x is the standard deviation of the blank/electrolyte and m is the slope of the calibration). LOD values of 1.48 x 10^{-5} and 4.06 x 10^{-5} M were attained for the SAMs-**3**|Poly(3-HT) and SAMs-**4**|Poly(3-HT) CMEs, respectively. In comparison to other gold modified electrodes and other methods, it is clear that the *in-situ* prepared Au electrodes achieved modest detection limits, see **Table 3**.

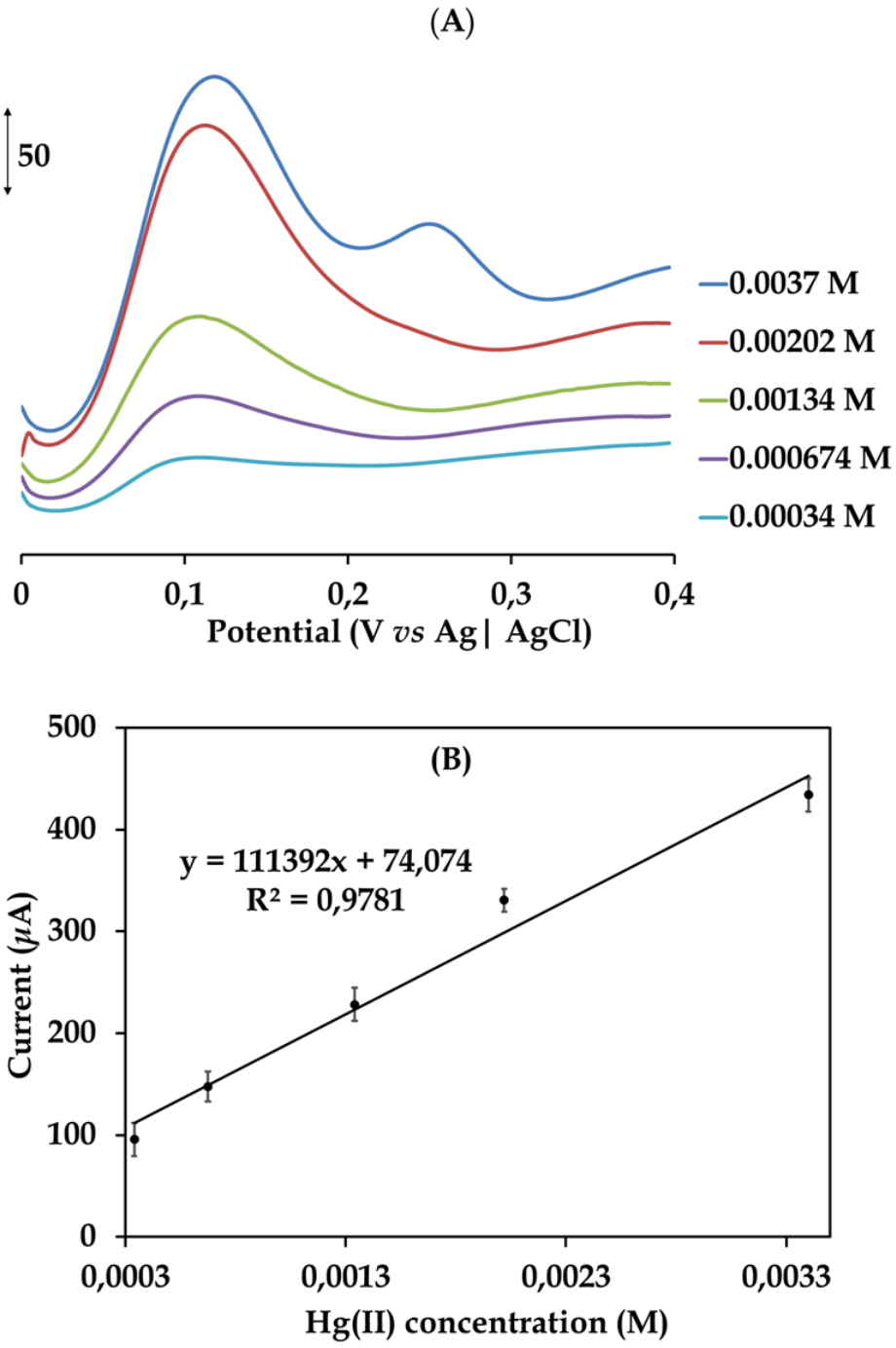

Fig. 4.18: *(**A**) DPASVs recorded in varying concentration of Hg(II) prepared in 0.1 M HCl and 0.4 M NaCl using the CoPc-**4** | Poly(3-HT) gold electrode. (**B**): Calibration curve of the current response against Hg(II) concentration.*

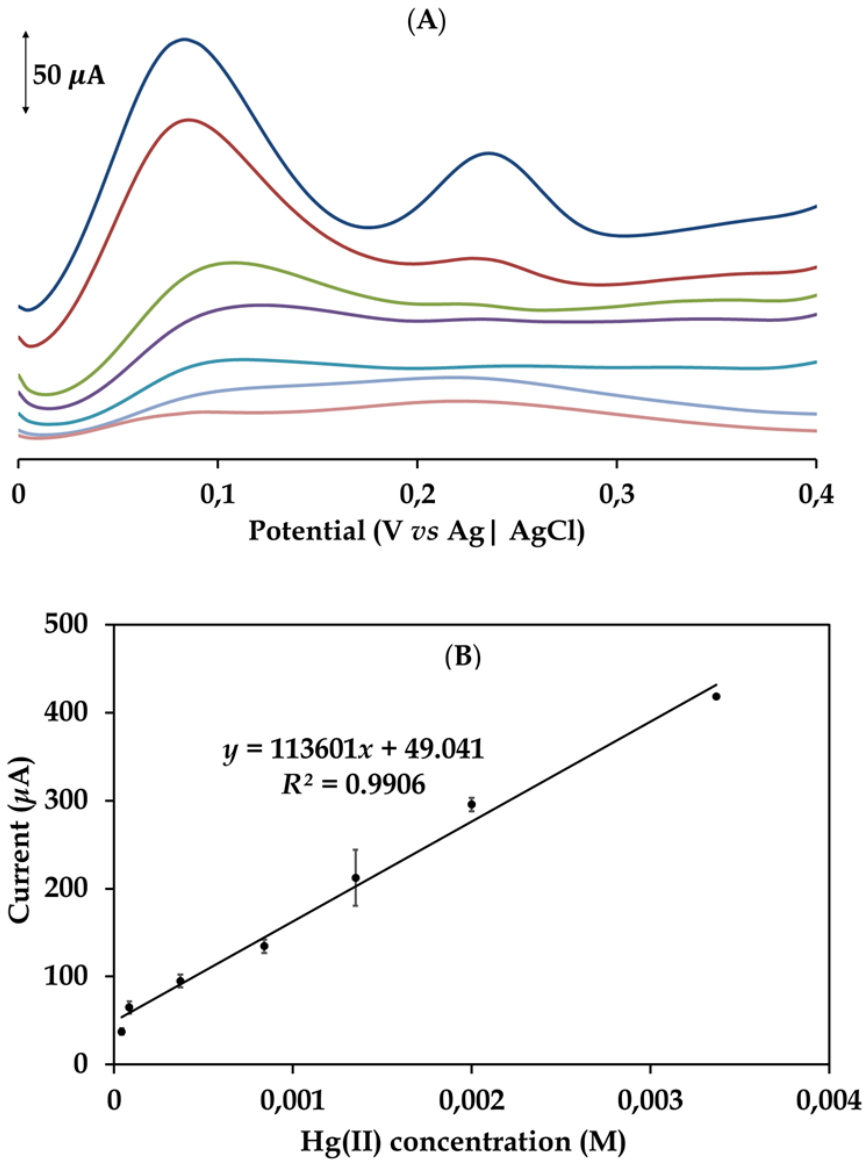

Fig. 4.19: *(**A**) DPASVs recorded in varying concentration of Hg(II) prepared in 0.1 M HCl and 0.4 M NaCl using the CoPc-**3** | Poly(3-HT) gold electrode. (**B**): Calibration curve of the current response against Hg(II) concentration.*

Table 3: *Comparisons of detection limits and linear ranges of various electrochemical detection techniques of Hg^{2+}.*

Electrode	Detection method	Limit of detection	Linear range (M)	References
AuAc-Chit	DPASV	0.8×10^{-14} M	10^{-14} – 10^{-7} M	56
Clicked-CoPc/GCE	DPASV	81.94×10^{-9} M	0 - 0.03×10^{-3} M	**30**
FePc/Si-NP/GCE	DPASV	2.28 μg.L-1	10-100 μg. L^{-1}	**26**
SWCNT-PhSH/Au electrode	SWASV	3×10^{-9} M	5 – 90×10^{-9} M	57
PTO/Au electrode	DPASV	60×10^{-15} M	0.21 – 1×10^{-9} M	58
SPGE-HT	SWASV	0.25 μg. L^{-1}	5 – 400 μg. L^{-1}	59
PXO/PIGE	DPASV	0.043 μg. L^{-1}	0.13 - 20.5 μg. L^{-1}	60
PMBT/AuNPs/SWCNTs/GCE	DPASV	80×10^{-15} M	0.4 – 96 x 10^{-9} M	55
SAMs-**3**|Poly(3-HT)-Au electrode	DPASV	1.48×10^{-5} M	4.21 x 10^{-5} – 3.37 x 10^{-3} M	TW
SAMs-**4**|Poly(3-HT)-Au electrode	DPASV	4.06×10^{-5} M	3.37 x 10^{-4} – 3.37 x 10^{-3} M	TW

Acronyms:
AuAc-Chit: gold atomic cluster chitosan
SWCNT-PhSH: single wall carbon nanotubes thiolphenol
PTO: Polythymine oligonucleotide
SPGE-HT: Screen printed gold electrode- High temperature
PXO/PIGE: Polyxylenol/paraffin impregnated graphite electrode
PMBT/AuNPs/SWCNTs/GCE: Poly(2-mercaptobenzothiazole/Gold nanoparticles/Single-walled carbon nanotubes

4.3.8. Interference studies

Selectivity of the CMEs in the presence of other divalent cations and anions including Pb^{2+}, Cu^{2+}, Zn^{2+}, SO_4^{2-}, NO_3^- and Cl^- were investigated on their possible interfering capabilities in the determination of Hg^{2+}. A mass-per-volume concentration of 1.0 g L^{-1} for each metal salt, *viz.* $HgSO_4$, $Pb(NO_3)_2$,$CuSO_4$ and $ZnCl_2$ in 0.1 M HCl and 0.4 M NaCl revealed distinctive peaks with the exception of the non-redox active Zn^{2+} and the anions, see **Figs. 4.20** and **4.21**. As reiterated before, the broadness of the mercury peak signal is accounted to the Hg_2^{2+} and Hg^{2+} species accumulating on the individual CME interfaces.[26] The discrimination against other interferents could be rationalized on the fact that the pre-concentration step allows for better binding of mercury species to the sulphur atoms of both the polymeric films and the different CoPc SAMs.

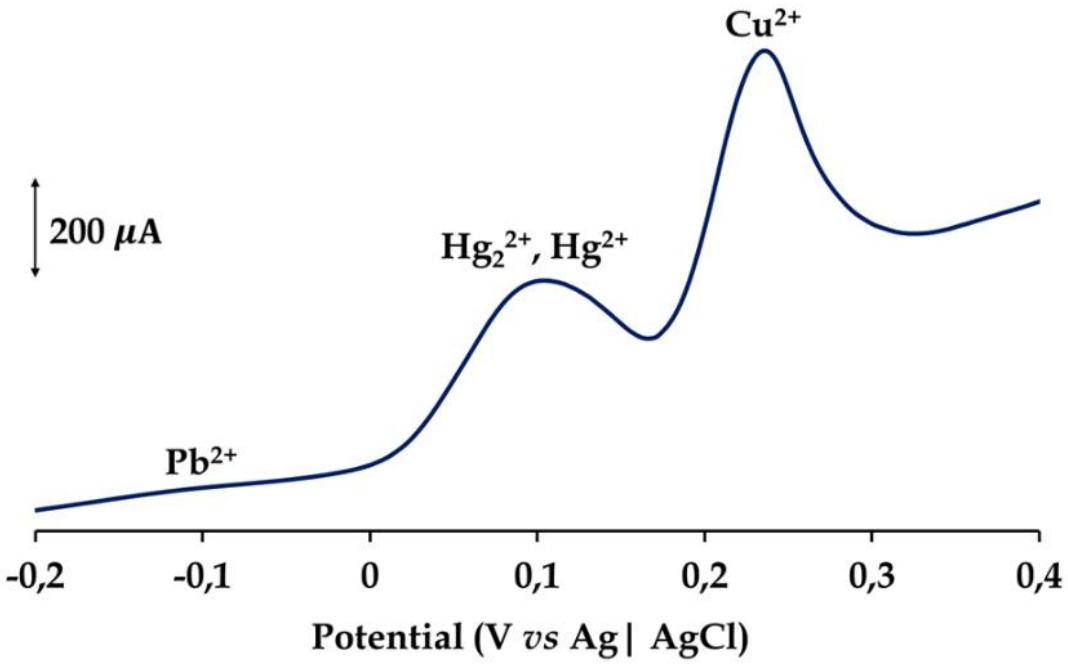

Fig. 4.20: *DPASV analysis of a sample matrix containing equal mass concentration of* 1.0 g L^{-1} *of* Hg^{2+}, Cu^{2+}, Pb^{2+} *and* Zn^{2+} *prepared in 0.1 M HCl and 0.4 M NaCl buffer solution using SAMs-***3** | *Poly(3-HT) Au electrode.*

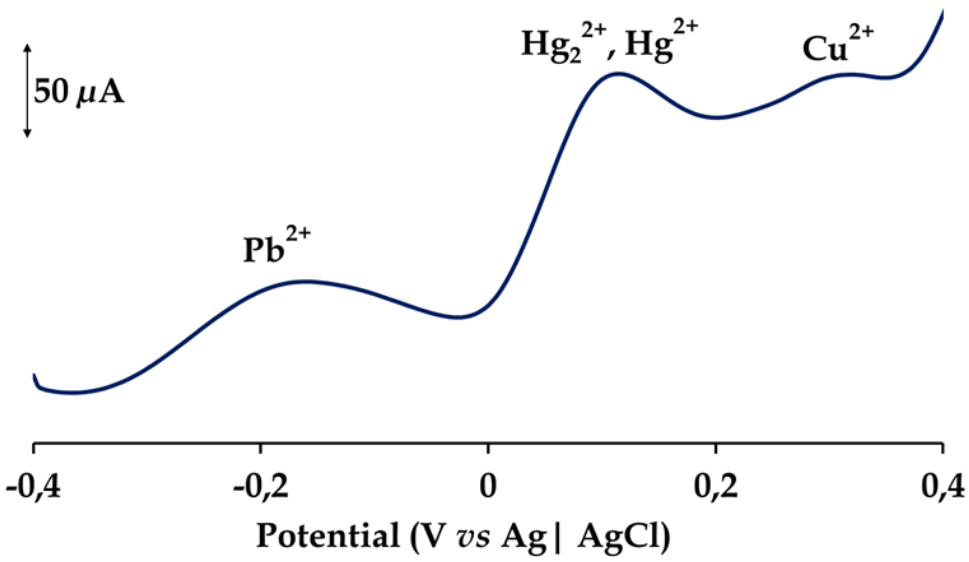

Fig. 4.21: *DPASV analysis of a sample matrix containing equal mass concentration of* $1g.L^{-1}$ *of* $Hg^{2+}, Cu^{2+}, Pb^{2+}$ *and* Zn^{2+} *prepared in 0.1 M HCl and 0.4 M NaCl buffer solution using SAMs-***4**| *Poly(3-HT) Au electrode.*

4.3.9. Analysis of real water sample

The fabricated SAMs-**3**|Poly(3-HT) Au electrode was tested for practical determination of Hg^{2+} in a water sample collected along the Umngcwini stream, which joins the Umgeni river, a major water source for the Province of KwaZulu-Natal. The water sample was firstly acidified with HCl to attain a 0.1 M HCl electrolyte solution. The analysis of the water sample proved to be below the LOD obtained and hence, the water sample was then spiked with $3.37x10^{-5}$ M and a standard addition technique was used to determine the concentration of Hg^{2+}. As shown in **Fig. 4.22**, four successive additions of $6.75\ x\ 10^{-4}$ M were added to the spiked sample and measured at optimized parameters.

The concentration was found to be $3.5\ x\ 10^{-5}(\pm 0.4)$ M with a good recovery of 104% for SAMs-**3**|Poly(3-HT) Au electrode, confirming the applicability of the method in the real sample. However, the SAMs-**4**| Poly(3-HT) Au electrode did not afford reproducible data which is accounted to surface fouling originating from

unknown interfering components in the sample matrix and thus, this CME was not considered further for data analysis. In contrast, the surface of the SAMs-**3**|Poly(3-HT) Au electrode could be readily regenerated after each stripping run by immersing it in a stirring solution containing 0.1 M HNO_3 and thereafter conditioning it at 0.7 V for 30 s. In particular, the regenerated active surface of the SAMs-**3**|Poly(3-HT) Au electrode showed good reproducible responses of Hg(II) with a relative standard deviation (RSD) of 8.92% calculated after 5 consecutive measurements. Similarly, the repeatability estimated over 6 measurements gave an RSD value of 8.45% for the same CME. The fact that the RSD values of the SAMs-**3**|Poly(3-HT) Au electrode falls outside the expected 95% data confidence interval for an analytically practical method, suggests that that this CME could also be subjected to minor surface fouling and supporting electrolyte effects.

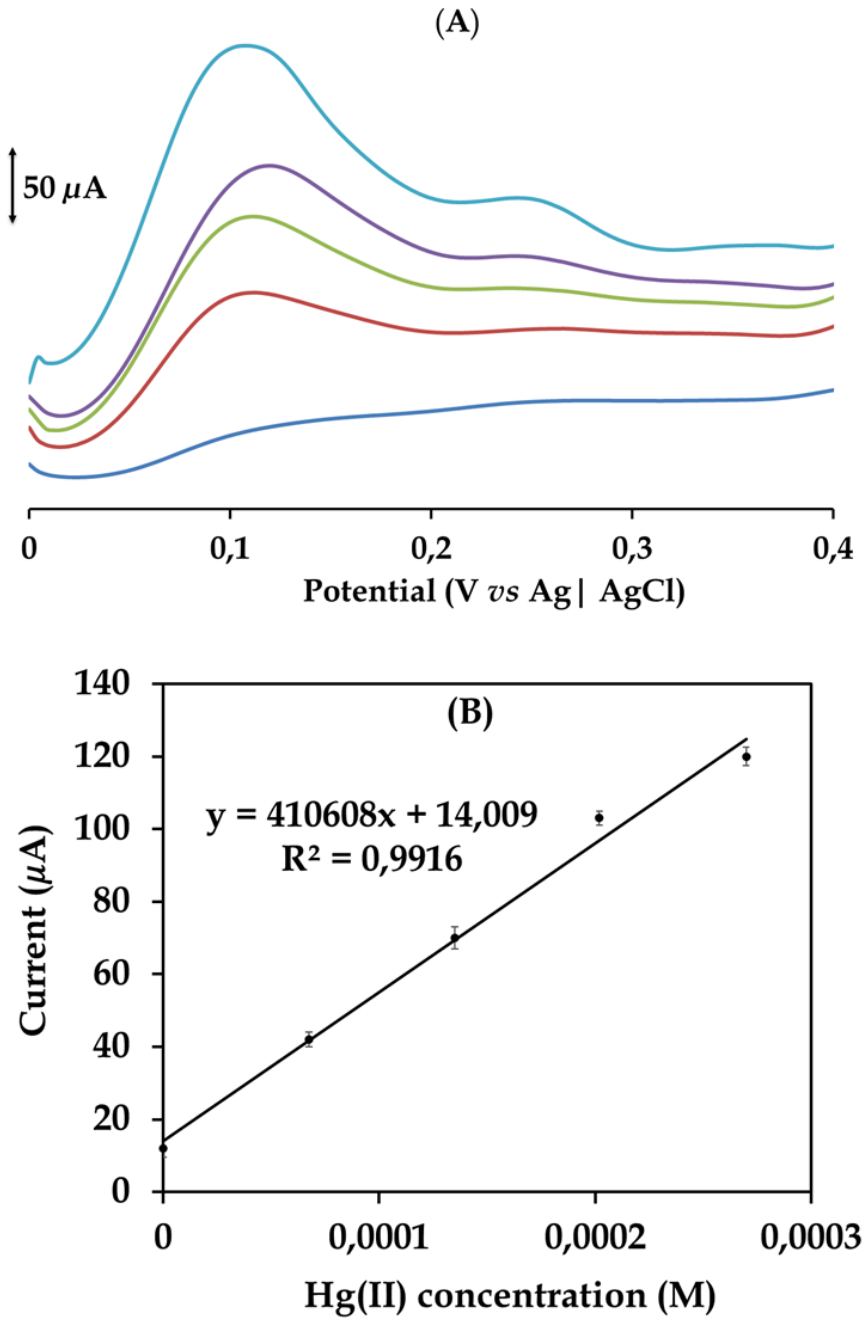

Fig. 4.22: *(**A**) DPASV responses of SAMs-**3** | Poly(3-HT) Au electrode for Hg(II) spiked river water and 4 standard additions of* $6.75x10^{-4}$ M *of Hg(II). (**B**) Standard addition plot.*

4.4. References

1. Kim, K. H.; Kabir, E.; Jahan, S. A., *J. Hazardous. Materials.* **2016,** *306*, 376-385.
2. Knobeloch, L.; Anderson, H. A.; Imm, P.; Peters, D.; Smith, A., *Environmental Research* **2005,** *97*, 220-227.
3. Bernhoft, R. A., *Journal of environmental and public health* **2012,** *2012*.
4. SABC News-City of Durban warns of high levels of mercury in the Umngcwini stream. https://www.sabcnews.com/sabcnews/city-of-durban-warns-against-high-levels-of-mercury-in-the-umngcwini-stream/ (accessed Nov 10, 2020).
5. Vetrimurugan, E.; Shruti, V.; Jonathan, M.; Roy, P. D.; Sarkar, S.; Rawlins, B.; Villegas, L. E. C., *Marine pollution bulletin* **2019,** *149*, 110555.
6. Carte Blanche-Mercury Madness. www.youtube.com/watch?v=tsnS9M-yl9c (accessed Nov 10, 2020).
7. National Primary Drinking Water Regulations | Ground Water and Drinking Water | US EPA. https://www.epa.gov/ground-water-and-drinking-water/national-primary-drinking-water-regulations (accessed Oct7, 2020).
8. *Guidelines for Drinking-water Quality FIRST ADDENDUM TO THIRD EDITION Volume 1 Recommendations WHO Library Cataloguing-in-Publication Data*; 9241546964; 2006.
9. Gao, Y.; Shi, Z.; Long, Z.; Wu, P.; Zheng, C.; Hou, X., Determination and speciation of mercury in environmental and biological samples by analytical atomic spectrometry. Elsevier: 2012; Vol. 103, pp 1-14.
10. dos Santos, J. S.; de la Guárdia, M.; Pastor, A.; dos Santos, M. L. P., *Talanta* **2009,** *80* (1), 207-211.
11. De Wuilloud, J. C. A.; Wuilloud, R. G.; Silva, M. F.; Olsina, R. A.; Martinez, L. D., *Spectrochimica Acta - Part B Atomic Spectroscopy* **2002,** *57* (2), 365-374.
12. Wang, J., *Analytical Electrochemistry, Third Edition*. 2006; p 1-250.
13. Yang, N.; Wan, Q.; Yu, J., *Sensors and Actuators, B: Chemical* **2005,** *110*, 246-251.
14. Fu, X. C.; Chen, X.; Guo, Z.; Kong, L. T.; Wang, J.; Liu, J. H.; Huang, X. J., *Electrochimica Acta* **2010,** *56*, 463-469.
15. Kempegowda, R. G.; Malingappa, P., *Electrochemistry Communications* **2012,** *25*, 83-86.

16. Keawkim, K.; Chuanuwatanakul, S.; Chailapakul, O.; Motomizu, S., *Food Control* **2013,** *31*, 14-21.
17. Zhang, Y.; Li, C.; Su, Y.; Mu, W.; Han, X., *Inorganic Chemistry Communications* **2020,** *111*, 107672-107672.
18. Bonfil, Y.; Brand, M.; Kirowa-Eisner, E., *Analytica Chimica Acta* **2000,** *424*, 65-76.
19. Munoz, R. A. A.; Felix, F. S.; Augelli, M. A.; Pavesi, T.; Angnes, L., *Analytica Chimica Acta* **2006,** *571*, 93-98.
20. Abollino, O.; Giacomino, A.; Malandrino, M.; Piscionieri, G.; Mentasti, E., *Electroanalysis* **2008,** *20*, 75-83.
21. Janegitz, B. C.; Figueiredo-Filho, L. C. S.; Marcolino-Junior, L. H.; Souza, S. P. N.; Pereira-Filho, E. R.; Fatibello-Filho, O., *Journal of Electroanalytical Chemistry* **2011,** *660*, 209-216.
22. Yoo, K.-S.; Woo, S.-B.; Jyoung, J.-Y. *Trace Mercury Determination by Differential Pulse Anodic Stripping Voltammetry Using Polythiophene-Quinoline/Glassy Carbon Modified Electrode*; 2003; pp 27-27.
23. Nyokong, T.; Khene, S., Modification of Electrode Surfaces with Metallo Phthalocyanine Nanomaterial Hybrids. In *Electrochemistry of N4 Macrocyclic Metal Complexes*, Springer: 2016; pp 225-275.
24. Damos, F. S.; Luz, R. d. C. S.; Tanaka, A. A., Electroanalysis of Hydrazine and Related Compounds by Oxidation Promoted with MN4 Macrocyclics. In *Electrochemistry of N4 Macrocyclic Metal Complexes*, Springer: 2016; pp 201-223.
25. Sajjan, V. A.; Aralekallu, S.; Nemakal, M.; Palanna, M.; Prabhu, C. K.; Sannegowda, L. K., *Inorganica Chimica Acta* **2020**, 119564.
26. Gounden, D.; Khene, S.; Nombona, N., *Chemical Papers* **2018,** *72*, 3043-3056.
27. Chohan, S.; Booysen, I. N.; Mambanda, A.; Akerman, M. P., *Journal of Coordination Chemistry* **2015,** *68*, 1829-1846.
28. Ozoemena, K., *Sensors* **2006,** *6*, 874-891.
29. Rojas, C.; Arancibia, V.; Gómez, M.; Nagles, E., *Sensors and Actuators B: Chemical* **2013,** *185*, 560-567.
30. Fomo, G.; Nwaji, N.; Nyokong, T., *Journal of Electroanalytical Chemistry* **2018,** *813*, 58-66.

31. Saman, N.; Johari, K.; Mat, H., *Microporous and Mesoporous Materials* **2014,** *194*, 38-45.
32. Wajima, T.; Sugawara, K., *Fuel Processing Technology* **2011,** *92*, 1322-1327.
33. Martín-Yerga, D.; González-García, M. B.; Costa-García, A., *Talanta* **2013,** *116*, 1091-1104.
34. Chohan, S.; Booysen, I. N.; Mambanda, A.; Akerman, M. P., *Inorganica Chimica Acta* **2016,** *447*, 183-191.
35. Kantize, K.; Vuyelwa , N.; Booysen, I. N.; Mambanda, A., *Polyhedron* **2021,***203*, 115235
36. Tamer, U.; Oymak, T.; Ertaş, N., *Electroanalysis* **2007,** *19*, 2565-2570.
37. Coates, M.; Antunes, E.; Nyokong, T., *Journal of Porphyrins and Phthalocyanines* **2010,** *14*, 568-581.
38. Sánchez, J.; Castillo, E.; Corredor, P.; Ágreda, J., *Portugaliae Electrochimica Acta* **2011,** *29*, 197-210.
39. Patil, R. S.; Juvekar, V. A.; Naik, V. M., *Industrial & engineering chemistry research* **2011,** *50*, 12946-12959.
40. Makinde, Z. O.; Louzada, M.; Mashazi, P.; Nyokong, T.; Khene, S., *Applied Surface Science* **2017,** *425*, 702-712.
41. Chung, T.; Wang, J.; Wang, J.; Cao, B.; Li, Y.; Pang, S., *Journal of Neural Engineering* **2015,** *12*, 056018.
42. Shumba, M.; Centane, S.; Chindeka, F.; Nyokong, T., *Journal of Electroanalytical Chemistry* **2017,** *791*, 36-48.
43. Mugadza, T.; Nyokong, T., *Electrochimica Acta* **2010,** *55*, 2606-2613.
44. Bredar, A. R.; Chown, A. L.; Burton, A. R.; Farnum, B. H., *ACS Applied Energy Materials* **2020,** *3*, 66-98.
45. Yoon, S.-B.; Jegal, J.-P.; Roh, K. C.; Kim, K.-B., *Journal of The Electrochemical Society* **2014,** *161*, H207.
46. Köksoy, B.; Soyer, O.; Orman, E. B.; Özkaya, A. R.; Bulut, M., *Dyes and Pigments* **2015,** *118*, 166-175.
47. Brown, K. L.; Danforth, R.; Bleitz, E.; Hwang, Y.; Rens, D., *International Journal of Electrochemical Science* **2020,** *15*, 10707-10721.

48. Demir, F.; Yenilmez, H. Y.; Koca, A.; Bayır, Z. A., *Journal of Electroanalytical Chemistry* **2019,** *832*, 254-265.
49. Demirbaş, Ü.; Akyüz, D.; Bayrak, R.; Barut, B.; Koca, A.; Kantekin, H.; Değirmencioğlu, İ., *Synthetic Metals* **2017,** *231*, 112-119.
50. Osmanbaş, Ö. A.; Koca, A.; Özçeşmeci, I.; Okur, A. I.; Gül, A., *Electrochimica Acta* **2008,** *53*, 4969-4980.
51. Arici, M.; Arican, D.; Uğur, A. L.; Erdoğmuş, A.; Koca, A., *Electrochimica Acta* **2013,** *87*, 554-566.
52. Jovanovski, V.; Hrastnik, N. I.; Hočevar, S. B., *Electrochemistry Communications* **2015,** *57*, 1-4.
53. Giacomino, A.; Abollino, O.; Malandrino, M.; Mentasti, E., *Talanta* **2008,** *75*, 266-273.
54. Bernalte, E.; Sánchez, C. M.; Gil, E. P., *Analytica Chimica Acta* **2011,** *689*, 60-64.
55. Fu, X. C.; Wu, J.; Nie, L.; Xie, C. G.; Liu, J. H.; Huang, X. J., *Analytica Chimica Acta* **2012,** *720*, 29-37.
56. Aneesh, P. K.; Nambiar, S. R.; Rao, T. P.; Ajayaghosh, A., *Physical Chemistry Chemical Physics* **2014,** *16*, 8529-8535.
57. Wei, J.; Yang, D.; Chen, H.; Gao, Y.; Li, H., *Sensors and Actuators, B: Chemical* **2014,** *190*, 968-974.
58. Wu, J.; Li, L.; Shen, B.; Cheng, G.; He, P.; Fang, Y., *Electroanalysis* **2010,** *22*, 479-482.
59. Squissato, A. L.; Rocha, D. P.; Almeida, E. S.; Richter, E. M.; Munoz, R. A. A., *Electroanalysis* **2018,** *30*, 20-23.
60. Manikandan, R.; Deepa, P. N.; Narayanan, S. S., *Ionics* **2019,** *25*, 1387-1394.

CHAPTER FIVE

Electrocatalytic determination of nevirapine using a platinum electrode modified with a polymeric CoPc-nafion-carbon nanotube composite

5.1. Introduction

Human immunodeficiency virus (HIV) infection and the acquired immunodeficiency syndromes (AIDS) are serious threats to global health and the subsequent consequences linked to it. Since the discovery of HIV, massive efforts have been concentrated on finding the cure. Various drugs have been approved for the treatment. These drugs fall under six categories: 1) Nucleotide reverse transcriptase inhibitors (NtRTIs), 2) Nucleoside reverse transcriptase inhibitors (NRTIs), 3) Non-nucleoside reverse transcriptase inhibitors (NN-RTIs), 4) Protease inhibitors (PIs), 5) entry inhibitors (EIs), and 6) Integrase inhibitors (INIs).[1] Nevirapine (NVP), is classified as a non-nucleoside reverse transcriptase inhibitor (NN-RTIs) and is often used in tandem with other reverse transcriptase inhibitors to give effective treatment.[2] Nevirapine (NVP) inhibits the transcription of RNA into DNA by binding at a different site away from the active site of the reverse transcriptase enzyme.[3]

The Republic of South Africa (RSA) has an estimated 7.5 million people living with HIV. Its health care system administers over one of the largest antiretroviral therapy (ART) program in the world which has been credited for a significant decrease in the rate of new infections especially in respect to the mother-to-child transmission rates.[4] The widespread use, as well as the challenges related to the safe disposal of domestic wastes in most metropolitan cities qualify antiretroviral drugs (ARVDs) as a subclass of emerging contaminants of concern, whose possible contamination of the

water resources poses a health and safety risk to the end-users.[5] Recently, there have been reports on the occurrence of NVP in river water, sampled near the cities of Johannesburg and Durban.[6, 7] The prevalence of residual pharmaceutical compounds is linked to their incomplete removal at the waste water treatment facilities, where the influent wastes which are of diversified origins, including medical wastes are directed to.

Various analytical techniques have been developed for the accurate quantitative determination of NVP in tablet formulations and human blood plasma, including high-performance liquid chromatography (HPLC),[8, 9] gas chromatography-mass spectrometry (GC-MS),[10] UV-Vis spectrometry,[11] liquid chromatography coupled to tandem mass spectrometry (LC-MS/MS),[2] and voltammetry techniques.[12-14] In recent years, electrochemical techniques have attracted the attention of many researchers largely because they are affordable, sensitive, accurate and fast alternatives for the determination of various analytes. There are reports in the literature on the voltammetric determination of NVP using chemically modified electrodes (CME) including nanoparticles immobilized on GCE,[12, 15] electrodes modified with CNTs [16] and polymer-based electrodes.[16, 17]

Literature trends illustrate that working CMEs modified with thin films of MPcs in combination with other highly conductive materials can synergistically lower the redox overpotentials of most reactions as well as enhancing their Faradaic currents.[18-20] In particular, conductance of the films encompassing MPcs have been improved by graphitic based material (*viz.* graphene sheet, tubes and quantum dots) and metallic nanoparticles.[18, 27, 28] The inclusion of these conductivity-promoting materials, enables swift electron transfer between the adsorbed analytes within the thin film and the electrode surface which can render lower overpotential during analyte detection. In addition, CMEs based on composites of MPcs and other nanoconjugates offer higher electroactive surface areas for enhanced immobilization of analytes compared to bare substrates. Consequently, the modified surfaces of these

conducting thin films exhibit more accessible catalytic sites that facilitate analyte preconcentration on CME surfaces.

Herein, the modification of a platinum electrode *via* drop-casting of a suspension mixture of coumarin substituted CoPcs and carboxylic acid functionalized multiwalled carbon nanotubes followed by the drying of the resultant modified electrode at room temperature is reported. Thereafter, a classical electron-mediating polymeric film, nafion (Naf) was drop casted on the CME interface. Incorporation of the carbon nanotubes in the immobilized thin films is rationalized by their intrinsic properties which include mechanical and chemical stabilities as well as electrical conductivity while Naf is a perfluorinated sulphonated cation exchanger with high permeability to cations and has desirable chemical robustness.[21]

5.2. Experimental

5.2.1. Materials

Starting organic and inorganic precursors: 7-hydroxy-4-trifluoromethyl coumarin, 4-nitrophthalonitrile and cobalt(II) chloride were procured from Sigma-Aldrich. The basic catalysts: 1,8-diazabicyclo[*5.4.0*]undec-7-ene (DBU) and potassium carbonate used to synthesize the compounds as well as the electrochemical grade supporting electrolyte, tetrabutylammonium tetrafluoroborate ($TBABF_4$), carboxylic acid functionalized multiwalled carbon nanotubes (*f*-MWCNTs) and nafion (Naf) perfluorinated resin solution were acquired from the same company.

Organic solvents as well as other materials including phosphorous pentoxide, molecular sieves (4 Å), silicon dioxide for column chromatography and silica plates for thin layer chromatography were all purchased from Merck SA. Dimethylformamide (DMF) was dried and stored over molecular sieves whereas water was ultrapurified *via* an Elga Purelab Ultra system. The derivatized phthalonitrile, 4-(4-trifluoromethyl)-coumarin-7-oxy) phthalonitrile and its

corresponding CoPc, β-tetra(7-oxy-4-trifluoromethylcoumarinphthalocyaninato)Cobalt(II) *viz*. CoPc-cou were synthesized according to previously reported work.[22]

5.2.2. Electrode modification

The platinum electrode surface was refreshed on a Buehler-felt pad using the 0.5 μm alumina paste and washed thereafter with ultrapure water. Subsequently, the electrode was sonicated in an ultrasonic bath in acetone for 5 min and rinsed again with ultrapure water. Various chemically modified electrodes were prepared to assess which modifiers promote superior electrocatalytic activity.

A 1 *m*M solution of CoPc-cou in dried DMF was electropolymerized onto a Pt surface to afford the CoPc-cou-Pt electrode.[22] This CME was modified further by the drop-dry method using a 5% Nafion (Naf-5) solution to obtain the CoPc-cou/Naf-5/Pt electrode. In addition, it was dried at room temperature. Three variant analogues of CoPc-cou/Naf-5/Pt electrodes were also fabricated. For example, when the bare Pt electrode was modified with Naf-5 alone using the drop-dry method (at room temperature), a Naf-5/Pt CME was formed. Similarly, a CoPc-cou-f-MWCNTs/Naf-5/Pt electrode was fabricated sequentially. The CoPc-cou was premixed with 0.5 *m*g of CoPc and 1 *m*g of *f*-MWCNTs in dry DMF under ultrasonication for one hour to render the nanoconjugate mixture. Subsequently, the mixture was drop casted onto a bare Pt electrode and was allowed to dry at room temperature. To ensure the robustness of the nanoconjugate film, it was further immobilized by drop-casting with Naf-5 at room temperature. The fourth CME (f-MWCNTs-Naf-5/Pt) was fabricated from a film of f-MWCNTs which had been dispersed in a Naf-5 solution. The suspension was ultrasonicated for 30 minutes and immobilization onto the Pt electrode surface followed by drying at ambient temperature to form the electrode.

5.3. Results and discussion

5.3.1. Electrochemical responsiveness of the CMEs

To evaluate the analytical sensitivity and electrocatalytic oxidation behavior towards NVP, the oxidation peak currents (I_{pa}), and the oxidation potentials E_{pa} were measured from their respective cyclic voltammograms (CVs) of 100 μM in a 0.1 M phosphate buffer saline (PBS) using the bare and the four CMEs, see **Fig. 5.1** and **Table 1**.

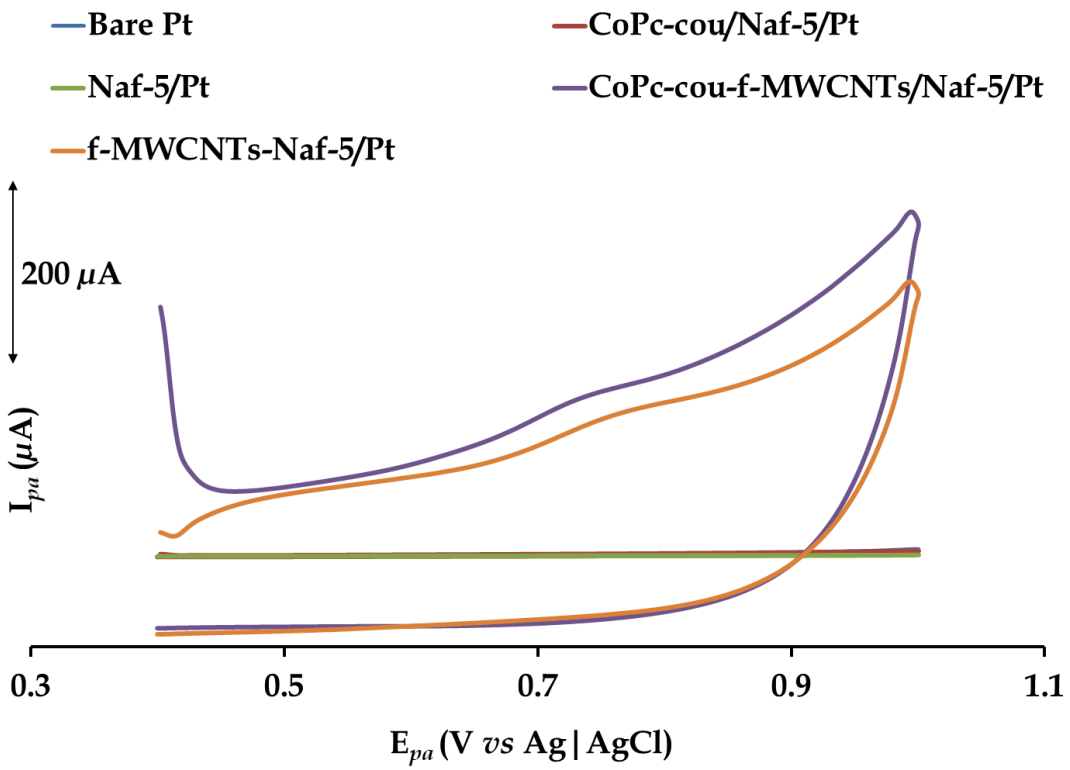

Fig. 5.1: *CVs obtained using bare Pt, CoPc-cou/Naf-5/Pt, Naf-5/Pt, CoPc-cou-f-MWCNTs/Naf-5/Pt and f-MWCNTs-Naf-5/Pt in aqueous solution of 100 μM NVP in 0.1 M PBS (pH = 12).*

Table 1: *Nevirapine peak currents and redox potentials (V vs Ag|AgCl) obtained using the different electrodes.*

Pt electrode	$\mathbf{I}_{pa}$ (μA)	$\mathbf{E}_{pa}$
Bare Pt	0.20	0.83
Naf-5/Pt	3.02	0.82
CoPc-cou/Naf-5/Pt	0.47	0.79
f-MWCNTs- Naf-5/Pt	150	0.74
CoPc-cou-*f*-MWCNTs/Naf-5/Pt	172	0.69

From **Figure 5.1**, it is evident that the values of I_{pa} for NVP by the bare electrode and the CMEs containing only the polymeric Naf-5 or CoPc-cou were negligibly low (< 5 μA, refer to **Table 1**) and the analyte was oxidized irreversibly as a result of the slow electron-transfer capabilities of their surfaces. However, the inclusion of either the *f*-MWCNTs constituents in the framework of the *f*-MWCNTs-Naf-5/Pt or CoPc-cou-*f*-MWCNTs/Naf-5/Pt afforded I_{pa} values that were 100-fold higher than the bare or the other two CMEs. Moreover, the oxidation of NVP occurred at lower E_{pa} values than the bare or the other two CMEs. The best electroanalytical response for the oxidation of NVP was recorded by the CoPc-cou-*f*-MWCNTs/Naf-5/Pt. It afforded superior electrocatalytic currents and lower redox potentials. This remarkable trend is attributed to a synergetic effect between the CoPc-cou-*f*-MWCNTs nanoconjugate constituents and Nafion (5%) which facilitates electron-mediation between the bulk analyte solution and the Pt substrate. This led to the use of CoPc-cou-*f*-MWCNTs/Naf-5/Pt only for further investigations on the catalytic oxidation behaviour towards NVP except for some sections where it shall be stated.

5.3.2. The effect of pH

The I_{pa} values for the electro-oxidation of NVP by the CoPc-cou-*f*-MWCNTs/Naf-5/Pt were extracted from the CVs (refer to **Fig. 5.2 (A)**) recorded for a 100 μM NVP solution at different pHs (6 – 12). A plot of the I_{pa} versus pH is presented in **Fig. 2B**. The I_{pa} values show a gradually increasing trend between pH 6 – 10, before increasing sharply at pH 12 and beyond. At the same time, E_{pa} values tandemly shifted to lower values. Furthermore, for pHs ≤ 6, no voltammetric oxidation signals could be detected. The electro-oxidation of NVP was optimum at a pH of 12 and further studies on the electrocatalytic behavior of the CME were performed at this pH.

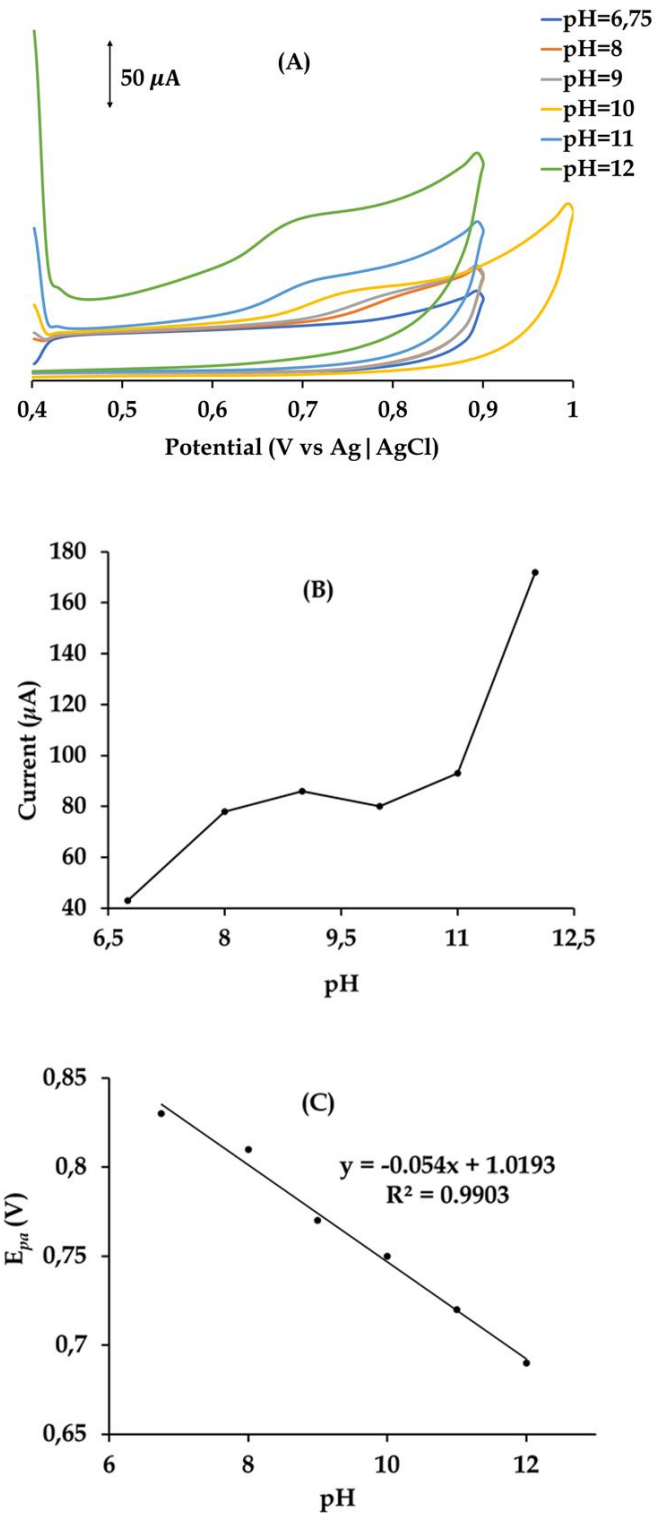

Fig. 5.2: *(**A**) CVs of 100 μM NVP in PBS with different pH values at CoPc-cou-f-MWCNTs/Naf-5/Pt, (**B**) Plot of I_{pa} vs pH, (**C**) Plot of E_{pa} vs pH.*

The oxidation of NVP at high pH values is known to proceed with the loss of two electrons ($2e^-$) and two protons ($2H^+$) as shown in **Scheme 1**.[16] The suppression of the oxidation of NVP in acidic media (pHs ≤ 6) is in line with the shifting of the equilibrium towards the left, as the $[H^+]_{medium}$ increases at the lower pH ranges. Nernst's plot *of* E_{pa} *vs* pH yielded a slope of 0.054 V, see **Fig. 5.2 (C)** which was closer to the theoretical value of 0.06 V for the oxidation reactions proceeding with loss of an equal number of electrons and protons (and $2e^-/2H^+$).[16]

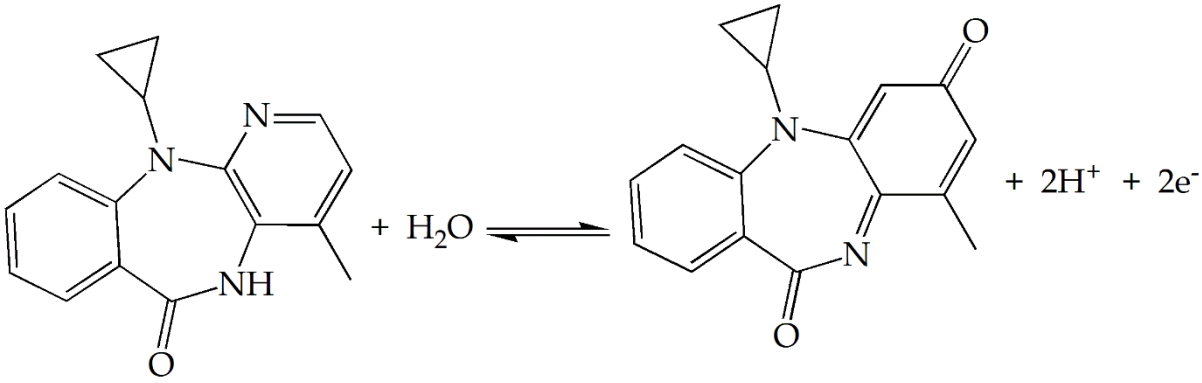

Scheme 1: *Redox interconversion of NVP* ***at pH 12.***

5.3.3. The effect of scan rate

To further elucidate the mechanism of NVP oxidation, the effect of scan rate was explored in the range of 25 to 250 mV/s in PBS (0.1 M, pH 12) buffer containing 100 μM NVP, see **Fig. 5.3 (A).** The plots of peak currents with square root of scan rates or scan rates gave linear relationships, indicating that both diffusion and adsorption mass transport processes were occurring, see **Figs. 5.3 (B)** and **5.3 (C)**. The value of the slope of the plot of the logarithm of peak currents ($Log\ I_{pa}$) and the logarithm of scan rate ($Log\ v$) was determined to be 0.602 which is within range of 0.5 and 1; further corroborating that both adsorption and diffusion mass transport processes are playing an integral part in the NVP oxidation mechanism, see **Fig. 5.3 (D)**.[17] However, the higher regression value attained in **Fig. 3C**, indicates that the oxidation process is controlled largely by adsorption. As described by the Laviron method,[23] the

relationship between the peak potentials (E_{pa}) and the logarithm of scan rates (Log υ) of irreversible systems is described by the following equation:

$$E_{pa} = E^0 + \left(2.303\frac{RT}{(1-\alpha)nF}\right)\text{Log}\left(\frac{RTk^0}{(1-\alpha)nF}\right) + \left(2.303\frac{RT}{(1-\alpha)nF}\right)\text{Log}\,\upsilon \qquad (\mathbf{1})$$

In the equation, α is the charge-transfer coefficient, υ is the scan rate, n is the number of transferred electrons and k^0 is the standard rate constant of the reaction. From the slope of E_{pa} *vs* Log v (**Fig. 5.3 (E)**), the value of α was found to be 0.545 which is close to the α equals 0.5 for irreversible systems. Furthermore, the Tafel slopes were calculated from the plot of peak potentials (E_{pa}) *vs* logarithm of scan rates ($Log\ \upsilon$) as defined by equation (**1**). The Tafel slope value of 130 mV was determined and is higher than the typical range of 30-120 mV/decade and affirms the strong interaction between the substrate and the thin film on the electrode.[24] In light of the above-mentioned mechanistic data, the facile diffusion of NVP occurs to the CME interface, where it undergoes adsorption and subsequent electro-oxidation. NVP adsorption to the CME surface could be governed by complementary intermolecular interactions between its functional groups and those of the coumarin moieties appended onto the CoPc core, the sulfonic groups of Nafion conducting polymer and the carboxylic acid groups of the *f*-MWCNTs.

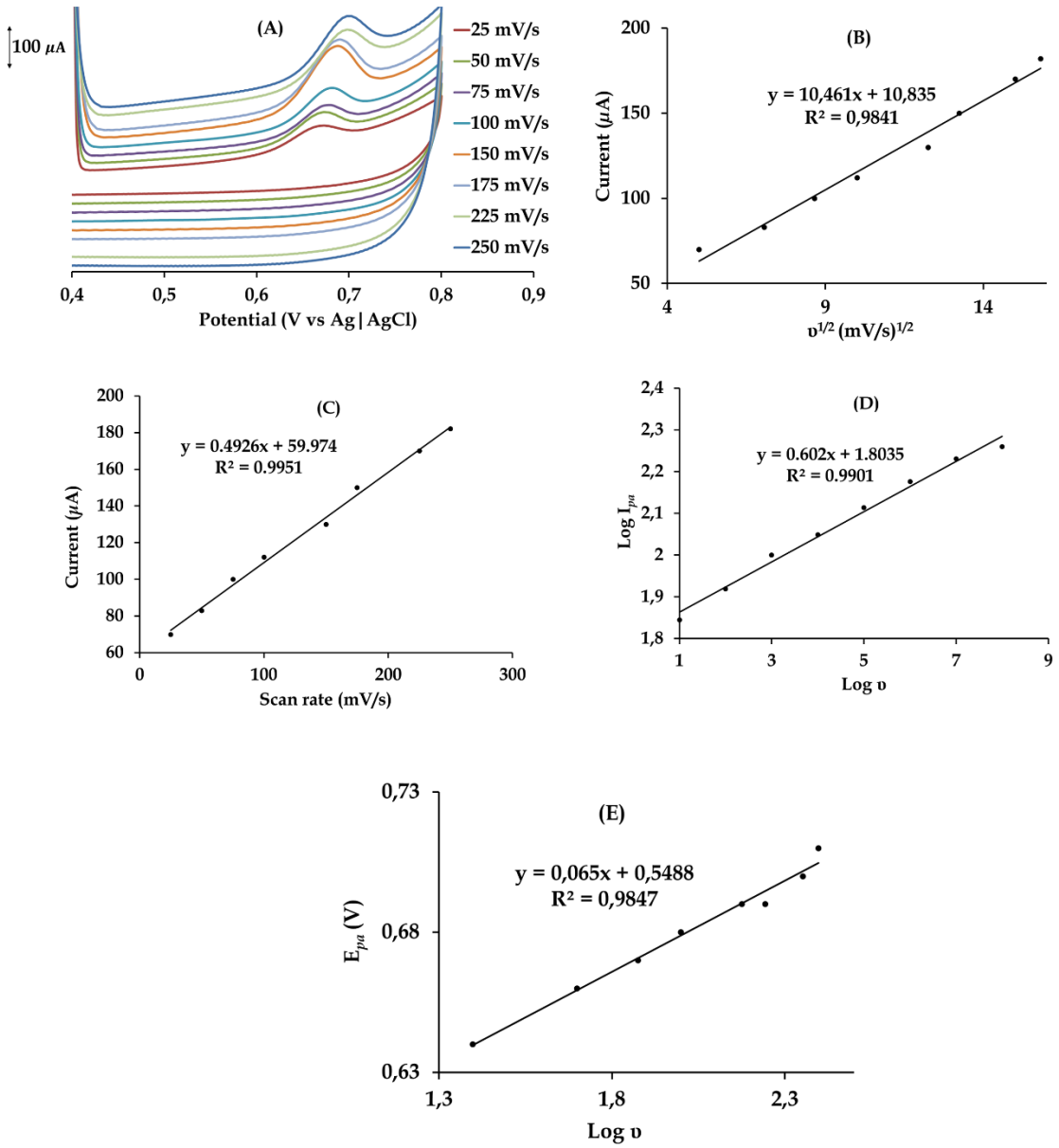

Fig. 5.3: *(**A**) CVs of CoPc-cou-f-MWCNTs/Naf-5/Pt in the presence of 100 μM NVP at various scan rates in PBS (pH = 12), (**B**) The plot of I_{pa} t vs square root of scan rate, (**C**) Anodic peak current vs scan rate, (**D**) The plot of Log I_{pa} vs Log υ and (**E**) The plot of E_{pa} vs Log υ.*

5.3.4. Surface area and coverage

The surface area of a CME is an important factor in assessing its electrocatalytic efficacy. Therefore, a redox probe solution of $K_3[Fe(CN)_6]$ was used to determine the effective surface area of the formed CME. CVs of CoPc-cou-*f*-MWCNTs/Naf-5/Pt at different scan rates, and conducted in 5 *m*M $K_3[Fe(CN)_6]$ which was prepared in an aqueous solution of 0.1 M KCl are depicted in **Fig. 5.4 (A)**. The effective surface area of the fabricated CME was determined using the Randles-Sevcik equation (**Equation 2**):[25]

$$I_{pa} = 2.69\ x\ 10^5 AD^{1/2}n^{3/2}v^{1/2}C \qquad (2)$$

where A is the effective surface area, D is the diffusion coefficient of $K_3[Fe(CN)_6]$, υ is the scan rate, C is the bulk molar concentration of $K_3[Fe(CN)_6]$, n is the number of electrons transferred (n = 1). The slope of the plot of the oxidation peak currents against the square root of scan rates was used to calculate the effective surface area, see **Fig. 4 (B)**. The relative effective surface area was found to be 12.88 cm^2 for the CME, and this value is significantly higher than that of the bare Pt electrode. The results further affirm successful modification of the surface of bare electrode, to attain a CME with more available adsorption sites for the analyte.

To further ascertain the modification of the electrode, the surface coverage of the CME was calculated using the effective surface area obtained above and the total charge under the peak using equation (3):

$$\Gamma = \frac{Q}{nFA} \qquad (3)$$

where Γ is the surface coverage, n is the number of transferred electrons, F is the Faraday constant and A is the effective surface (cm^2). The surface coverage value $3.41x10^{-10}$ mol cm^{-2} is above the value of $1x10^{-10}$ mol cm^{-2} of a Pc molecule lying flat on the electrode.[26]

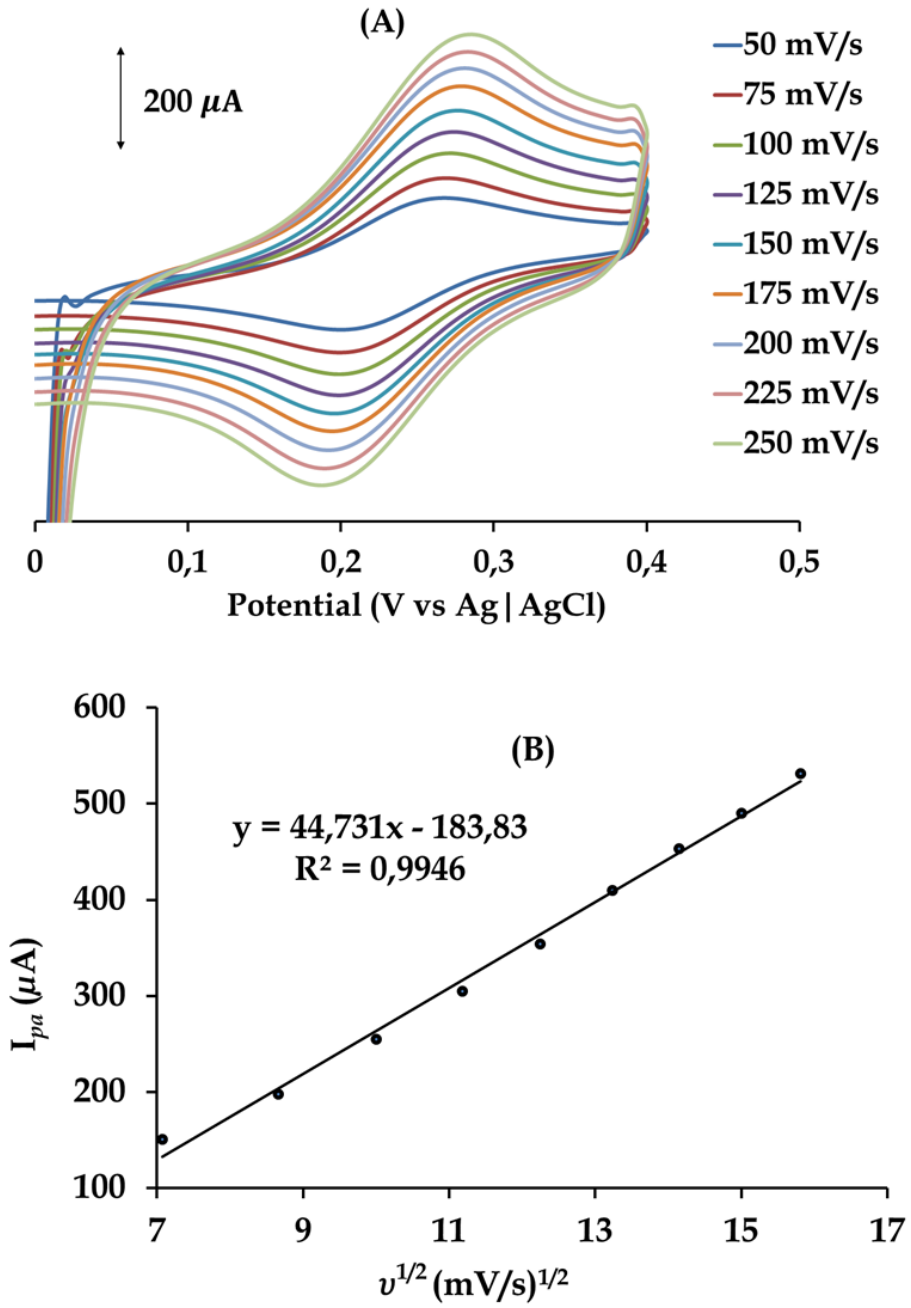

Fig. 5.4: (**A**) *CVs conducted in 5.0 mM* $K_3[Fe(CN)_6]$ *prepared 0.1 M KCl(aq) at pH 12 using the* CoPc-cou-*f*-MWCNTs/Naf-5/Pt *at different scan rates (50, 75, 100, 125, 150, 175, 200, 225, and 250 mV/s). (**B**) Plot of* I_{pa} *vs square root of scan rate.*

5.3.5. Electrochemical impedance spectroscopy

The EIS experiments were conducted in a 5 mM $[Fe(CN)_6]^{3-/4}$ at a frequency range of 0.1 Hz to 100 kHz using the bare, CoPc-cou *f*-MWCNTs/Pt and CoPc-cou-*f*-MWCNTs/Naf-5/Pt electrodes. Results are summarised in **Table 2**. The electrical circuit fitting the impedance spectra is shown in **Fig. 5.5 (D)**. The presence of both the kinetic (R_{ct}) and diffusion (Z_w) parameters refer to mixed electrode reactions. All the impedance spectra are composed of a depressed semi-circle except for the unmodified Pt electrode in the high frequency and a straight line in the low-frequency range, see **Figs. 5.5 (A) – (C)**. It is well documented that the high-frequency arc is due to the charge transfer limitations and is directly measured as the semi-circle diameter whereas the straight-line encompasses diffusion systems.[27, 28]

The values as summarized in Table 2 show an excellent charge transfer capability at the interfaces of the CoPc-cou-*f*-MWCNTs/Naf-5/Pt. Its charge transfer resistance (R_{ct} value of 195 Ω) is about 5 times lower than that of the bare electrode (R_{ct} value of 1.01 k Ω). The higher charge transfer kinetics of the former electrode is undoubtedly facilitated by the synergism emanating from the combined electrochemical properties of the CoPc core, *f*-MWCNTs and Naf-5 polymer of the nanohybrid modifier of the electrode. oThe aforementioned trend further corroborates the electrocatalytic data monitored by cyclic voltammetry in **Fig. 5.1**.

It is also worthy to note that the values of *n* (an exponent-related to the depression angle for all CMEs) are less than 1, indicating the non-homogeneity of the surfaces of the CMEs.[29] Bode plots showed phase angle of ~ 70 º for the bare Pt electrode and respective angles of ~ 2 º and ~ 3 º for CoPc-cou-*f*-MWCNTs/Pt and CoPc-cou-*f*-MWCNTs-Naf-5/Pt electrodes, see **Fig. 5.6**. This further confirmed the non-capacitive nature of the electrodes given their phase angles being less than 90 º for an ideal capacitor.

Table 2: *Summary of EIS data collected in a 5 mM $[Fe(CN)_6]^{3-/4}$ using the bare and modified working electrodes. Error values are shown in brackets*

Pt	R_s (Ω)	R_{ct} (Ω)	Z_w (*m*S)	CPE (*m*S)	[a]*n*
Bare	15.1 (0.6)	1010 (0.5)	0.8 (1.5)	-	-
CoPc-cou-*f*-MWCNTs	25.1 (0.4)	329 (6.5)	9.88 (4.4)	2.1 (1.3)	0.6 (0.5)
CoPc-cou-*f*-MWCNTs/Naf-5	20.2 (0.6)	195 (4.5)	4.56 (6.8)	0.6 (1.1)	0.7 (0.4)

[a]*n is the exponent related to the depression angle.*

Values in brackets are percentage errors obtained from fitting the experimental Nyquist plot

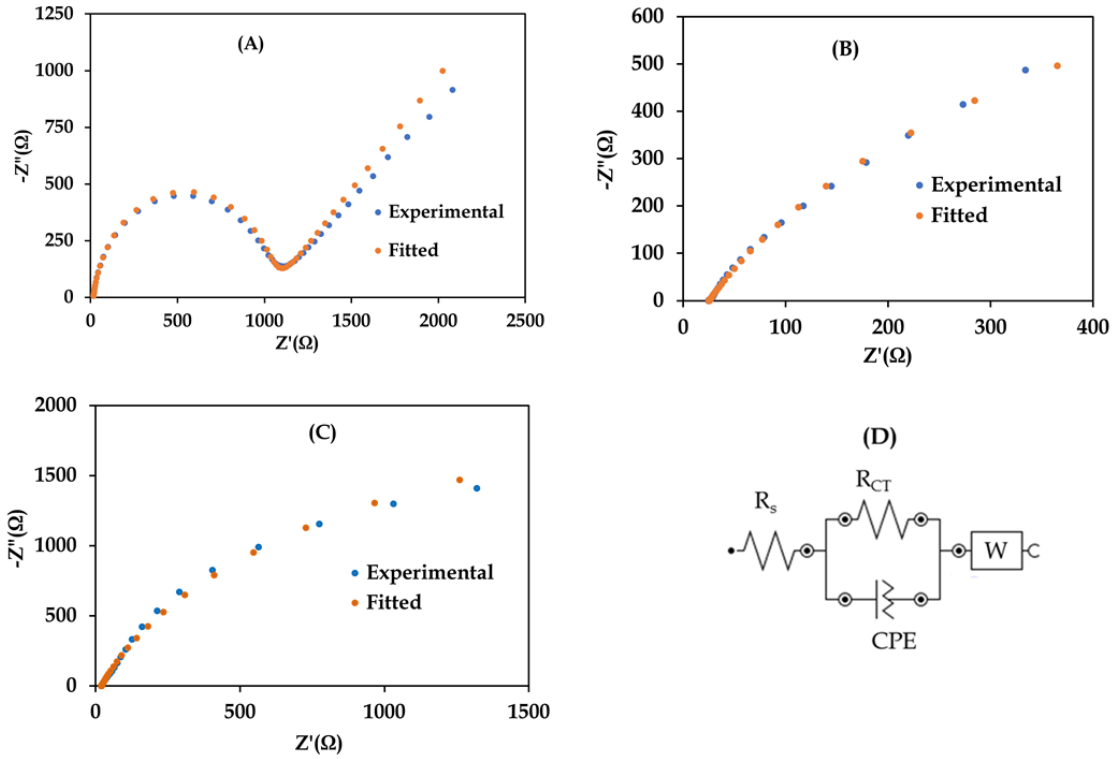

Fig. 5.5: *Nyquist plots attained in solution of 5 mM $[Fe(CN)_6]$ prepared in PBS using (**A**) bare Pt electrode, (**B**) CoPc-cou-f-MWCNTs/Pt electrode and (**C**) CoPc-cou-f-MWCNTs/Naf-5/Pt electrode. (**D**) The equivalent circuit used to fit the EIS data.*

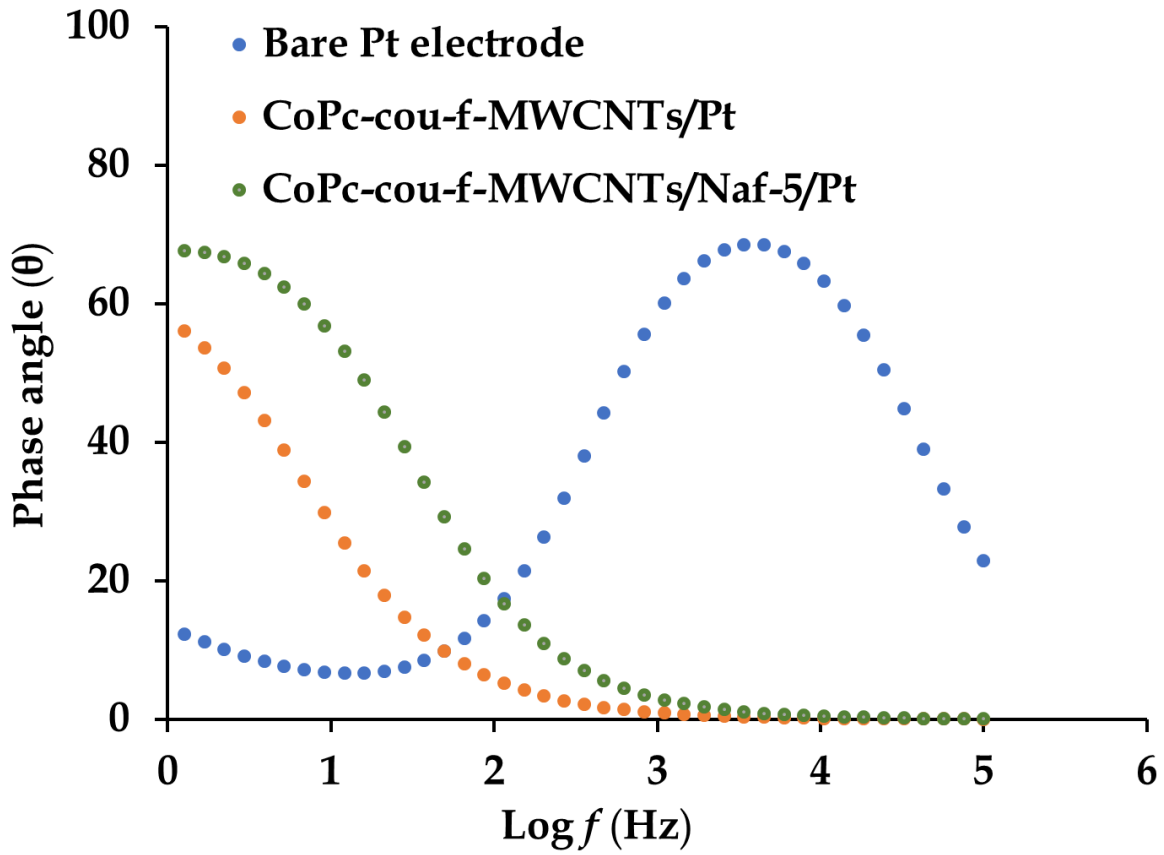

Fig. 5.6: *Bode plots generated with the respective working electrodes.*

5.3.6. Redox reactions kinetics

Single-step chronoamperometry was used to determine the electrocatalytic rate constant in 100 μM NVP in PBS (pH = 12) when using the CoPc-cou-*f*-MWCNTs/Naf-5/Pt under diffusion-controlled experimental conditions, see **Fig. 5.7 (A).** The chronoamperomogram of the CME was obtained by applying overpotentials with respect to the E_{pa} value of NVP attained during their corresponding CVs at an interval time of 7 – 15 s. The rate constant for the oxidation reaction of NVP was determined using the following equation, Eq. (**4**):[30]

$$\frac{I_c}{I_b} = \gamma^{1/2}\pi^{1/2} = \pi^{\frac{1}{2}}(kCt)^{1/2} \qquad (4)$$

Where I_c and I_b are currents in the presence and absence of NVP, k is the catalytic rate constant ($M^{-1}\ s^{-1}$), C is the bulk concentration of Nevirapine, and t time elapsed in seconds. From the plot of I_c/I_b vs $t^{1/2}$, the diffusion-controlled rate constants were calculated, see **Fig. 5.7 (B)**. The diffusion rate constant obtained was found to be $9.68x10^5\ M^{-1}\ s^{-1}$ which is superior compared to other reported diffusion-controlled rate constants for NVP and a bio-analyte, dopamine.[14, 31, 32] In fact, NVP and dopamine detection follow similar oxidative mechanisms and the fabricated CME illustrated faster electron transfer kinetics ($> 10^2\ M^{-1}\ s^{-1}$), than the modified electrodes used for the oxidation of dopamine.[31, 32] Moreover, rate constants of the same order were attained for the CME and a GCE modified with a nanohybrid comprised of TiO_2 nanoparticles and graphene nanoribbons.[14] Therefore, it is evident that the constituents of the electron-mediating thin film of CoPc-cou-*f*-MWCNTs/Naf-5/Pt enhances the diffusion of NVP as well as its adsorption and subsequent oxidation.

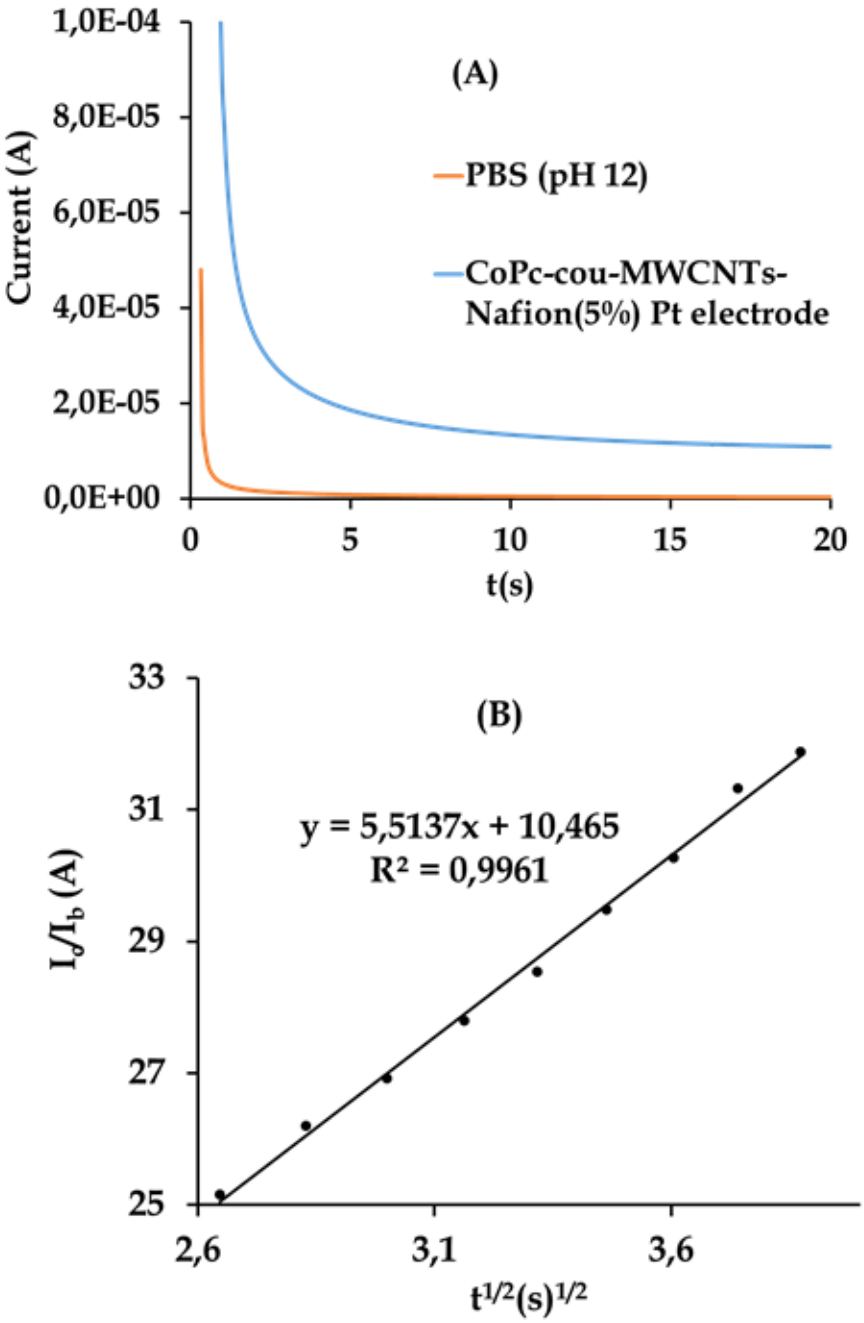

Fig. 5.7: *(**A**) Chronoamperograms acquired in a pH 12 PBS buffer and a 100 µM NVP prepared in pH 12 PBS buffer using the* CoPc-cou-*f*-MWCNTs/Naf-5/Pt. *(**B**) Plot of* $\frac{I_c}{I_b}$ *vs* $t^{1/2}$.

The electrocatalytic oxidation of NVP under conditions of convective transfer generated by the rotating disk electrode, set at variable rotation speeds (ω) was conducted to determine the heterogeneous electron transfer rate constant, *k*. The linear sweep voltammograms (LSVs) at 10 mV/s are shown in **Fig. 5.8 (A)**. A linear graph was obtained when the limiting current (I_L) data was plotted against $\omega^{1/2}$ according to the Levich equation:[33]

$$I_L = 0.62nFAD^{2/3}\nu^{-1/6}\omega^{1/2}C_0 \qquad (\mathbf{5})$$

where *D* is the diffusion coefficient of the NVP, A the electrode area, ν the kinematic viscosity, ω is rotation rate and C_0 the bulk concentration of the analyte. Thus, under the set conditions of the experiment mass transfer of NVP to the surface of the disk electrode was dominated by convection currents. Fitting the data to the Koutecky-Levich equation[34] enabled the calculation of *k* (M^{-1} s^{-1}) for the electrocatalytic oxidation of NVP at the RDE

$$\frac{1}{I_L} = \frac{1}{nFAC_o k\Gamma} + \frac{1}{0.62nFAD^{2/3}\upsilon^{-1/2}C_o\omega^{1/2}} \qquad (\mathbf{6})$$

When the inverse of the plateau currents, $(I_L)^{-1}$ was plotted against the inverse of the rotation speed of the electrode, $(\omega^{-1/2})$, a straight line was obtained, see **Fig. 5.8** (**C**). The *y*-intercept of the plot yielded the rate constant of 2.02 x 10^2 M^{-1} s^{-1} for the oxidation NVP which is less than the diffusion-controlled rate constant attained with the same CME. The lower convection-controlled rate constant is attributed to higher convection rates rendering surface fouling where the rapidly accumulating analyte and its oxidized specie saturate the electrocatalytic sites of the CME.

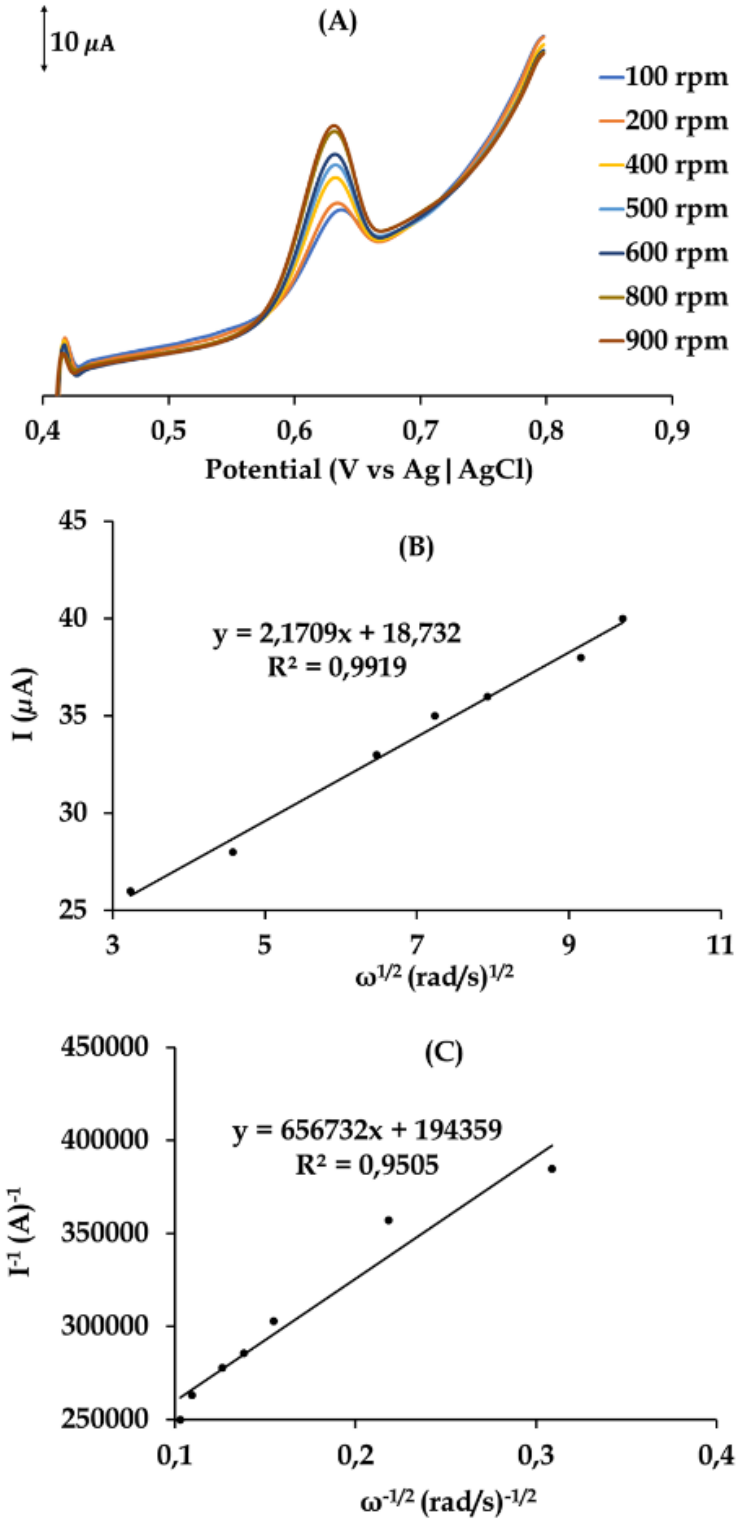

Fig. 5.8: (**A**): *LSVs attained at a scan rate of 10 mV/s using the* CoPc-cou-*f*-MWCNTs/Naf-5/Pt *for a sample of 30 μM NVP prepared pH 12 PBS. (**B**) The Levich plot. (**C**) The Koutecky-Levich plot.*

5.3.7. Analytical application of the CME

Under the optimized conditions, CoPc-cou-*f*-MWCNTs/Naf-5/Pt was evaluated for its performance and results are presented in **Table 3** together with data by other electrochemical detection techniques of NVP. Linear sweep voltammetry and chronoamperometry techniques were comparatively used to generate calibration curves for NVP. **Fig. 5.9 (A)** showed linear sweep voltammogram responses obtained at a fixed rotation speed of 100 rpm and scan rate of 10 mV/s with NVP aliquots of variable concentrations. Progressive increases in the NVP concentration resulted in a linear increase in the electrocatalytic oxidation currents according to equation (**7**):

$$I = 1.9958[NVP]_{\mu M} + 19.021,\ R^2 = 0.981 \quad (7)$$

The calibration curve was linear over a wide concentration range from 0.6 nM to 30 μM in PBS at pH 12 with a regression coefficient of R^2=0.981, see **Fig. 5.9 (B)**. Using the standard deviation of 10 repetitive measurements of a blank electrolyte solution (S_x), the limit of detection (LOD) was calculated from the calibration graph according to LOD = $3S_x/m$ and was determined to be 0.21 nM.

Fig. 5.10 (A) shows the chronoamperometric responses obtained at varying concentration levels of NVP. The CoPc-cou-*f*-MWCNTs/Naf-5/Pt afforded a broad linear calibration equation **(8)**,

$$I = 0{,}5859[NVP]_{\mu M} + 4.7531,\ R^2 = 0.982 \quad (8)$$

The concentration was linear within the range from 4 nM to 30 μM in PBS at pH 12 with a regression coefficient of R^2=0.9849, see **Fig. 5.10 (B)**. An LOD value of 2.5 nM was obtained using the above equation where S_x was the standard deviation of 8 repetitive measurements of PBS (pH = 12) and *m* was the slope of the calibration curve. The linear sweep voltammetry data afforded a broader linear range of detection as well as a lower detection limit which can be rationalized based on the lower rotational speed used as well as lower scan rate, which allowed for the better migration of NVP species to the electrode interface. Consequently, this electroanalytical technique was chosen for subsequent analysis. Also, comparative

analysis of CoPc-cou-*f*-MWCNTs/Naf-5/Pt with other reported CMEs used for the electrocatalytic detection of NVP indicates that CoPc-cou-*f*-MWCNTs/Naf-5/Pt has a higher sensitivity.

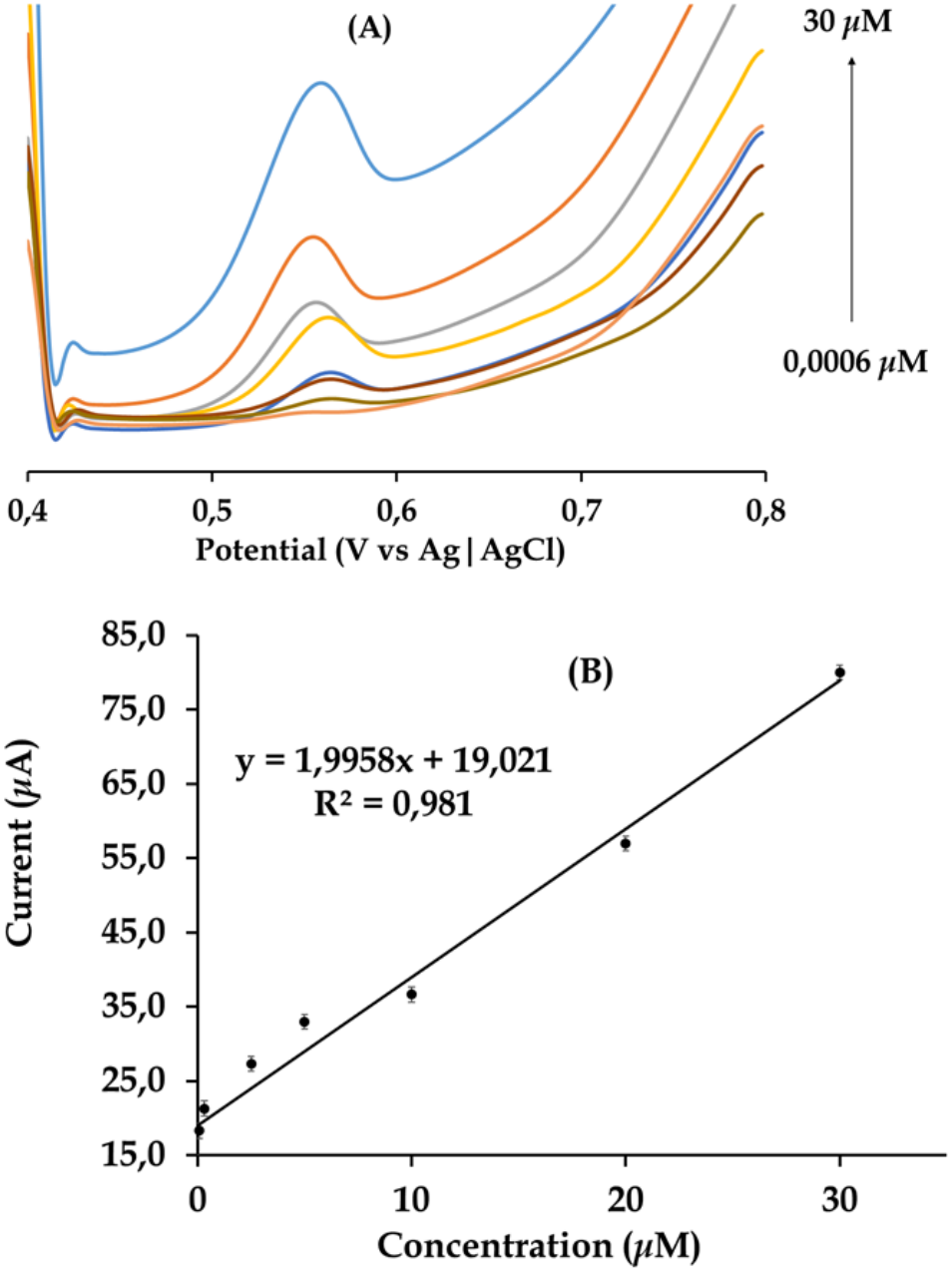

Fig. 5.9: *(**A**) Linear sweep voltammograms (LSVs) recorded in varying concentrations of NVP prepared in PBS (pH = 12) using the CoPc-cou-f-MWCNTs/Naf-5/Pt. (**B**) Calibration curve of the current response against NVP concentration*

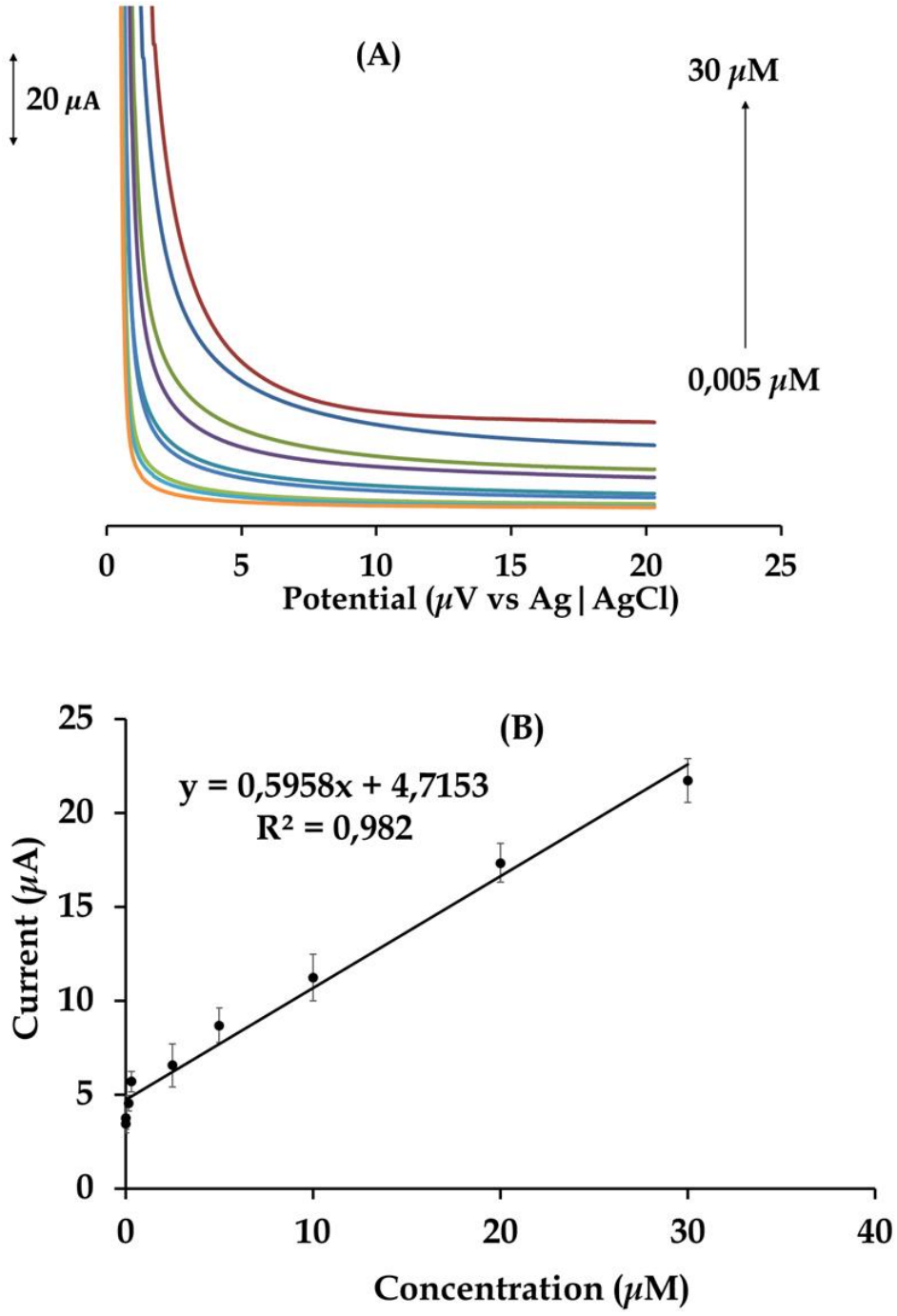

Fig. 5.10: **(A)** *Chronoamperomograms recorded at a varying concentration of NVP prepared in PBS (pH=12) using the* CoPc-cou-*f*-MWCNTs/Naf-5/Pt. ***(B)*** *Calibration curve of the current response against NVP concentration.*

Table 3: *Comparisons of NVP detection limits and linear ranges of various CMEs.*

Electrode	Detection method	Limit of detection	Linear range (μM)	References
AuNPs/p(MB)/MWCNTs/GCE	DPASV	0.1-50 μM	0.056	[16]
Ura/CPE	DPV	0.1-70 μM	0.05	[21]
CuO-CNPs-GCE	LSV	0.1-100 μM	0.066	[12]
TiO_2/GNR/GCE	DPV	0.020-0.14 μM	0.043	[14]
Ag-PtNPs/MWCNTs/GCE	DPV	0.76-3.81 μM	0.021	[35]
Pd@rGO/MoS_2 QDs GCE	DPV	0.1-80 μM	0.05	[36]
CP-Bi_2O_3	DPV	0.050-50 μM	0.110	[37]
Hg/GCE	ASV	0.01-0.14 ppm	0.003	[38]
CoPc-cou-*f*-MWCNTs/Naf-5/Pt	LSV CA	0.0006-30 μM 0.004-30 μM	0.000212 (μM) 0.0025 (μM)	This work

AuNPs/p(MB)/f-MWCNTs: gold nanoparticles/poly methylene blue/functionalized multiwalled carbon nanotubes
Ura/CPE: Uracil/ Carbon paste electrode
CuO-CNPs: Copper oxide – Carbon nanoparticles
TiO_2/GNR: Titanium oxide/Graphene nanoribbons
Ag-PtNPs/MWCNTs: Silver-Platinum nanoparticles/ multiwalled carbon nanotubes
Pd@rGO/MoS_2 QDs: Palladium at reduced graphene oxide/molybdenum disulfide quantum dots.
CP-Bi_2O_3: Carbon Paste-Bismuth(III) oxide.
Hg: Thin film layer of mercury

5.3.8. Interferences studies

To evaluate the selectivity of the CoPc-cou-*f*-MWCNTs/Naf-5/Pt, different organic molecules including Ascorbic acid (AA), Cysteine, Dopamine (DA), Metronidazole (MB) and Uric acid (UA) were tested for their possible signal suppression during detection of NVP by the CME under the optimised conditions of analysis. **Fig. 5.11** show current responses of NVP (10 μM) in the presence of a 100-fold excess concentration of each of the above-mentioned interferents. Noticably, the NVP oxidation peak is more intense and well resolved from those of the interferents and occurs at a lower positive oxidation potential compared to the solution without interferences (**Fig. 5.9 (A)**). The better sensitivity and selectivity of CoPc-cou-*f*-MWCNTs/Naf-5/Pt for NVP in the matrix background these interferents could be ascribed to the higher affinity of NVP for the Naf-5 constituents through electrostatic attractions between the N atoms of NVP and the cationic exchange sites of Naf-5. The aforementioned intermolecular interactions could be further consolidated by hydrogen-bonding originating from the coumarin groups of the CoPc molecules and the carboxylic acid groups of the *f*-MWCNTs with the analyte's amine hydrogen.

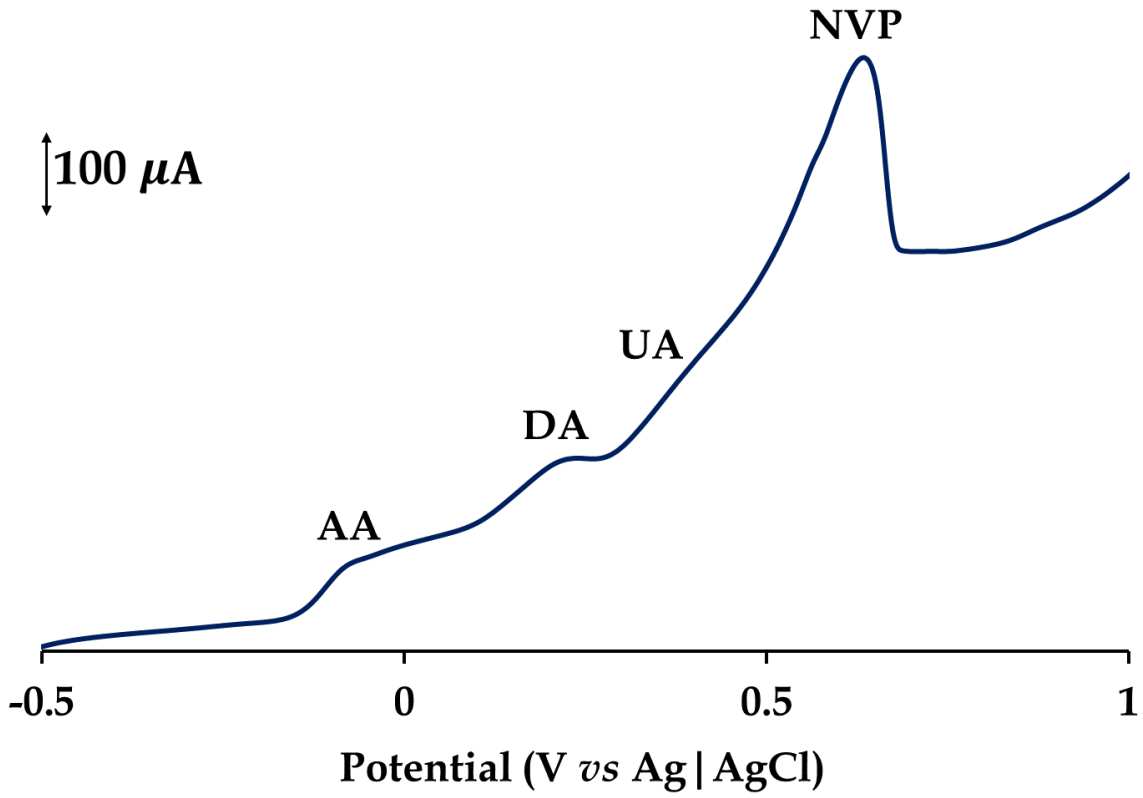

Fig. 5.11*: LSV of a sample matrix containing* 10 μM *NVP and 100* μM *dopamine, uric acid, metronidazole, cysteine, and ascorbic acid prepared in PBS (pH = 12) solution using CoPc-cou-f-MWCNTs/Naf-5/Pt.*

5.3.9. LSV determination of NVP in the pre-spiked and equilibrated river water spiked sample

Using LSV, the CoPc-cou-*f*-MWCNTs/Naf-5/Pt was tested for practicability for the determination of NVP in river water, which had been collected from the Msunduzi river at the Camps Drift site in Pietermaritzburg. The river water sample (500 mL) was filtered, and a phosphate buffer tablet was added to each, and the pH adjusted to 12. It was pre-spiked with NVP so that it had a final concentration of 1.75 μM. Several aliquots (10 cm^3) of the pre-spiked river water samples along with an unspiked duplicate were left to age at room temperature for one day. LSV of the unspiked duplicate river water samples at the CoPc-cou-*f*-MWCNTs/Naf-5/Pt electrode yielded undiscernible current responses, which was an indication that the concentration of NVP in the river water was below the LOD. A measurable current

response for NVP was obtained for the pre-spiked (1.75 μM NVP) and the equilibrated river water sample. Subsequently, incremental aliquots of 2.00, 4.00, 6.00 and 8.00 cm^3 of the 2.5 μM NVP standard were transferred to 4 x 10 cm^3 portions of the 10.00 cm^3 pre-spiked and pre-equilibrated river water samples. The respective LSV current responses of the spiked samples are shown in **Fig. 5.12(A)**. The calibration graph for the standard additions of NVP to the pre-spiked river water at the CoPc-cou-*f*-MWCNTs/Naf-5/Pt electrode is presented in **Fig. 5.12 (B)**. Using the slope, the aliquot volume of the river water and the concentration of the NVP standard solution, the concentration of NVP in the pre-spiked water was estimated to be 1.88 μM, which translated to a 110% recovery by the developed sensor.

The reproducibility of the fabrication of the CoPc-cou-*f*-MWCNTs/Naf-5/Pt electrode was tested whilst analyzing river water spiked with 30 μM NVP by the LSV method. Five different CoPc-cou-*f*-MWCNTs/Naf-5/Pt CMEs were prepared, and their LSV responses of the NVP were recorded. The percent relative standard deviation (%RSD) for the measurements by each of the five reproduced electrodes was found to be 4.22. Thus, the fabrication of the sensing film of the CoPc-cou-*f*-MWCNTs/Naf-5 Pt electrode for the catalytic oxidation of NVP in river water could be reproduced with good precision. The reproducibility of the CME was tested by recording the linear sweep currents for river water pre-spiked with 30 μM NVP from 6 consecutive runs using one of the fabricated electrodes. The %RSD for the currents was found to be 4.63. The fabricated electrode demonstrated good precision of reproducibility for the measurement NVP in river water samples.

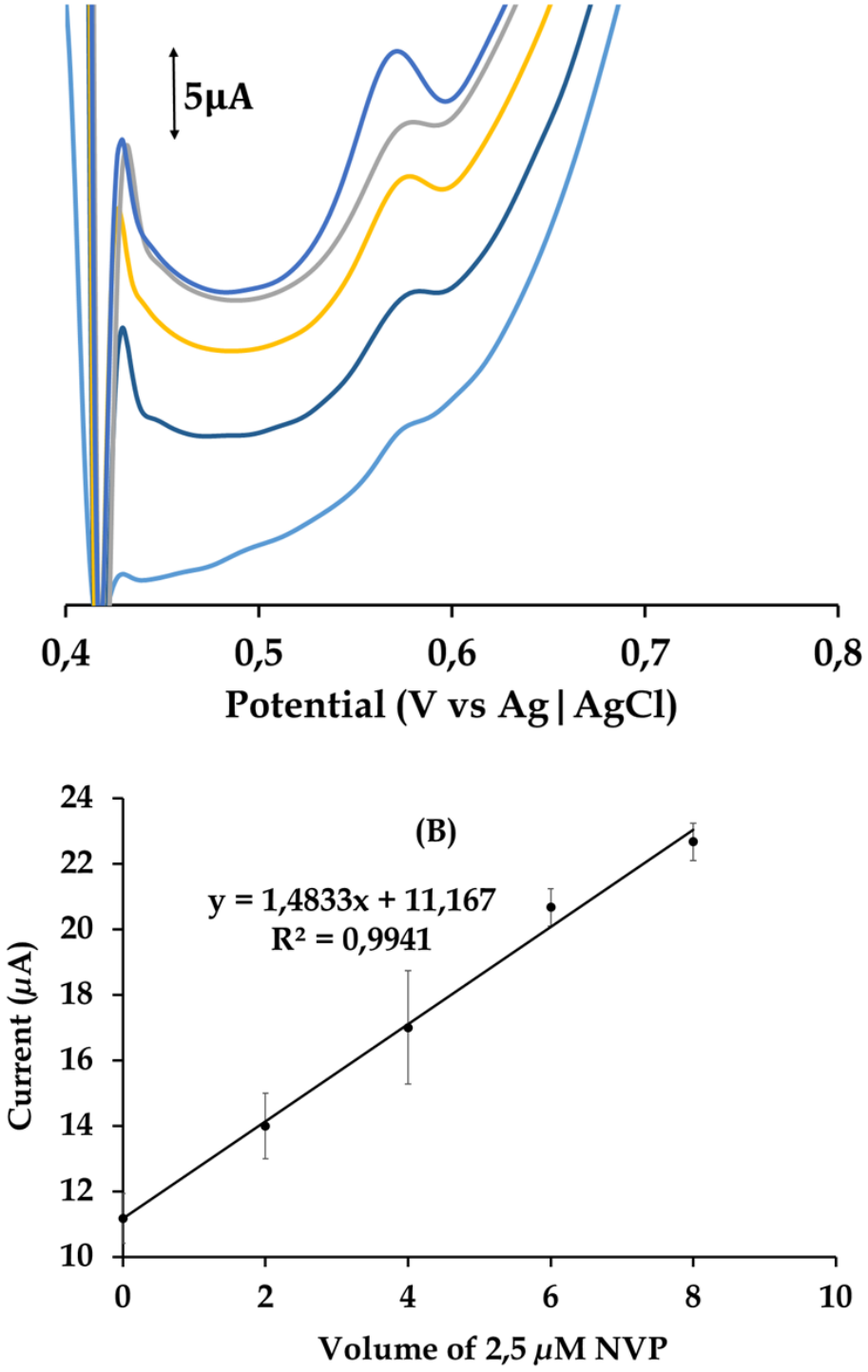

Fig. 5.12: *(**A**) LSV responses of* CoPc-cou-*f*-MWCNTs/Naf-5/Pt for 10.00 cm^3 of *pre-spiked river water (*1.75 *µ*M *NVP) after addition of 2.00, 4.00, 6.00 and 8.00 mL of the 2.5 µ*M *NVP calibrating standards. (**B**) Standard addition plot.*

5.4. References

1. Bozal, B.; Uslu, B.; Özkan, S. A., *International Journal of Electrochemistry* **2011,** *2011*, 1-17.
2. Kumar, V. R.; Reddy, B. P. B.; Kumar, B. R.; Sreekanth, K.; Babu, K. N., *Journal of Chromatography B: Analytical Technologies in the Biomedical and Life Sciences* **2013,** *921-922*, 9-14.
3. Castro, A. A.; Cordoves, A. I. P.; Farias, P. A. M., *Analytical Chemistry Insights* **2013,** *8*, 21-28.
4. UNAIDS https://www.unaids.org/en/regionscountries/countries/southafrica (accessed 25-04-2021).
5. Swanepoel, C.; Bouwman, H.; Pieters, R.; Bezuidenhout, C., PRESENCE, CONCENTRATIONS AND POTENTIAL IMPLICATIONS OF HIV-ANTI-RETROVIRALS IN SELECTED WATER RESOURCES IN SOUTH AFRICA. Water Research Commission of South Africa: 2015.
6. Abafe, O. A.; Späth, J.; Fick, J.; Jansson, S.; Buckley, C.; Stark, A.; Pietruschka, B.; Martincigh, B. S., *Chemosphere* **2018,** *200*, 660-670.
7. Rimayi, C.; Odusanya, D.; Weiss, J. M.; de Boer, J.; Chimuka, L., *Science of the Total Environment* **2018,** *627*, 1008-1017.
8. Safari, M.; Shamsipur, M.; Zohrabi, P.; Ebrahimzadeh, H., *Journal of Pharmaceutical and Biomedical Analysis* **2019,** *166*, 95-104.
9. Rezk, N. L.; Tidwell, R. R.; Kashuba, A. D. M., *Journal of Chromatography B: Analytical Technologies in the Biomedical and Life Sciences* **2002,** *774*, 79-88.
10. Vogel, M.; Bertram, N.; Wasmuth, J. C.; Emmelkamp, J.; Rockstroh, J. K.; Reichel, C., *Journal of Chromatographic Science* **2010,** *48*, 91-94.
11. Rangapriya, M.; Rajendran, N. N., *International Journal of Pharma Sciences and Research* **2014,** *5*, 656-664.
12. Shahrokhian, S.; Kohansal, R.; Ghalkhani, M.; Amini, M. K., *Electroanalysis* **2015,** *27*, 1989-1997.
13. Teradal, N. L.; Seetharamappa, J., *Electroanalysis* **2015,** *27*, 2007-2016.
14. Apath, D.; Moyo, M.; Shumba, M., *Journal of Chemistry* **2020,** *2020*.

15. Tiwari, P.; Nirala, N. R.; Prakash, R., *ChemistrySelect* **2018,** *3*, 5341-5347.
16. Gholivand, M. B.; Ahmadi, E.; Haseli, M., *Analytical Biochemistry* **2017,** *527*, 4-12.
17. Massumi, S.; Ahmadi, E.; Akbari, A.; Gholivand, M. B., *Journal of Electroanalytical Chemistry* **2020,** *876*, 114508-114508.
18. Kantize, K.; Booysen, I. N.; Mambanda, A., *Journal of Electroanalytical Chemistry* **2019,** *850*, 113391-113391.
19. Koçak, Ç. C.; Nas, A.; Kantekin, H.; Dursun, Z., *Talanta* **2018,** *184*, 452-460.
20. Winiarski, J. P.; de Barros, M. R.; Wecker, G. S.; Nagurniak, G. R.; Parreira, R. L. T.; Affeldt, R. F.; Peralta, R. A.; Jost, C. L., *Journal of Materials Chemistry C* **2020,** *8*, 6839-6850.
21. Fan, Y.; Liu, J. H.; Lu, H. T.; Zhang, Q., *Colloids and Surfaces B: Biointerfaces* **2011,** *85*, 289-292.
22. Chohan, S.; Booysen, I. N.; Mambanda, A.; Akerman, M. P., *Journal of Coordination Chemistry* **2015,** *68*, 1829-1846.
23. Ahmadi, E.; Gholivand, M. B., *Analytical Methods* **2019,** *11* (36), 4659-4667.
24. Mugadza, T.; Nyokong, T., *Polyhedron* **2011,** *30* (11), 1820-1829.
25. Shumba, M.; Centane, S.; Chindeka, F.; Nyokong, T., *Journal of Electroanalytical Chemistry* **2017,** *791*, 36-48.
26. Chohan, S.; Booysen, I. N.; Mambanda, A.; Akerman, M. P., *Inorganica Chimica Acta* **2016,** *447*, 183-191.
27. Oliveira, S. C. B.; Oliveira-Brett, A. M., *Electrochimica Acta* **2010,** *55*, 4599-4605.
28. Sekar, N.; Ramasamy, R. P., *Journal of Microbial and Biochemical. Technology. S* **2013,** *6*.
29. Zhang, J., *Electrochemical impedance spectroscopy in PEM Fuel Cells*. Springer: 2009.
30. Mugadza, T.; Arslanolu, Y.; Nyokong, T., *Electrochimica Acta* **2012,** *68*, 44-51.
31. Ngwenya, V.; Booysen, I. N.; Mambanda, A., *Journal of Coordination Chemistry* **2019,** *72*, 1131-1145.
32. Daneshinejad, H.; Chamjangali, M. A.; Goudarzi, N.; Roudbari, A., *Materials Science and Engineering: C* **2016,** *58*, 532-540.
33. Kumar, M. K.; Prataap, R. V.; Mohan, S.; Jha, S. K., *Microchimica Acta* **2016,** *183*, 1759-1768.

34. Akinbulu, I. A.; Khene, S.; Nyokong, T., *Thin solid films* **2010,** *519*, 911-918.
35. Okumu, F. O.; Silwana, B.; Matoetoe, M. C., *Electroanalysis* **2020,** *32*, 3000-3008.
36. Tiwari, P.; Nirala, N. R.; Prakash, R., *ChemistrySelect* **2018,** *3*, 5341-5347.
37. Teradal, N. L.; Seetharamappa, J., *Electroanalysis* **2015,** *27*, 2007-2016.
38. Aguiar Castro, A.; Queiroz Aucelio, R.; Adrian Rey, N.; Monsores Miguel, E.; Augusto Mardini Farias, P., *Combinatorial chemistry & high throughput screening* **2011,** *14*, 22-27.

CHAPTER SIX

Conclusions and Future work

6.1. Conclusions

The need to find alternatives to traditional analytical techniques which often are laborious, expensive, demand highly trained technicians, has led to the emergence of electroanalytical techniques. These techniques are sought after due to their fast detection times, no sample extraction needed, easily portable as well as their affordability which makes them attractive for routine water quality control. On the other hand, they have been a growing concern of new class of pollutants which are characterised by widespread use, lack of information pertaining their occurrence, environmental fate after disposal, including their potential ecological effects. These compounds are classified as emerging pollutants and they are pharmaceuticals. In order to address these challenges, new class of nano materials are purposely designed for use in cost-effective analytic techniques which can rapidly detect and determine the concentration of these pollutants as a way of establishing concentration data sources for mapping out their distribution patterns in the environment in order to regulate them their use and disposal.

In chapter three, the CoPc-X-*f*-MWCNTs hybrids (X = flav or bo) were fabricated as well as spectroscopically and microscopically characterized. Glassy carbon electrodes modified with the nanoconjugates afforded robust CMEs which showed electrocatalytic activities towards the emerging pollutant, APAP. The resultant CMEs showed good resistance to surface fouling and afforded good reproducibility as per the relatively linear ranges of detection. The optimal electrocatalytic activities of the CMEs were attributed to their enhanced effective surface areas of the CMEs accompanied with their faster diffusion- and convection-controlled electron transfer kinetics. Modelled equivalence circuits were validated by

good fits between the experimental and calculated data. Superior electron transfer rates of the CMEs were emphasized by their lower charge transfer resistance attained in comparison to that of the bare GCE. The MPc-nanofabricated electrodes also displayed excellent selectivity when tested against a range of pharmaceutical interferent species.

In chapter four, self-assembled monolayers of CoPcs followed by electropolymerization of 3-hexythiophene onto gold electrodes were *in situ* fabricated. The electrocatalytic parameters of the resultant CMEs were optimized carefully. Under optimized conditions, the CMEs could detect the mercury(I) and -(II) cations simultaneously. Relatively moderate LOD values of 1.48 x 10^{-5} M (for the SAMs-**3**|Poly(3-HT) Au electrode) and 4.06 x 10^{-5} M (for the SAMs-**4**|Poly(3-HT) Au electrode) were attained where the corresponding calibrations plots rendered linear ranges of detection of 4.21 x 10^{-5} – 3.37x10^{-3} M and 3.37 x 10^{-4} – 3.37 x10^{-3} M. Both CMEs showed favourable sensing capabilities of the mercury cations in the presence of the divalent cations, $Cu^{2+}$and Zn^{2+} and a typical heavy metal pollutant, Pb^{2+}, as well as selected anions. The SAMs-**3**|Poly(3-HT) Au electrode could reliably quantify Hg(II) in the surface water of a river sample with an excellent recovery of 104% attained provided confidence in our standard addition method as well as the integrity of the CME.

In chapter five, a durable and sensitive CoPc-cou-*f*-MWCNTs/Naf-5/Pt sensor for the catalytic oxidation of NVP was successfully fabricated by the sequential drop-casting of a suspension mixture of the cobalt phthalocyanine and the multiwalled carbon nanotubes followed by a drop and dry of Nafion (5%). Under the optimized conditions, CoPc-cou-*f*-MWCNTs/Naf-5/Pt showed lower detection limits than other NVP electrochemical sensors. The CoPc-cou-f-MWCNTs/Naf-5/Pt could detect NVP

in relatively broad linear concentration ranges using chronoamperometry and linear sweep voltammetry, respectively. Furthermore, the sensor showed excellent discrimination capabilities against selected common organic interferents present in the matrices. A recovery of 110% was attained by the LSV determination of NVP in a Msunduzi river water sample pre-spiked at 1.75 μM NVP. The sensor has the potential for the accurate and precise analysis of NVP in surface water samples. Moreover, the CME affordedexcellent reproducibility and repeatability results.

6.2. Future work

The scope of the future work will entail the use of carefully chosen analyte-targeting substituents and the formation of their asymmetric substituted MPcs for subsequent electrode modification *via* the established Click reaction between the electrografted azido groups and the alkynyl mast groups of the asymmetric MPcs. The modification entails usually the grafting of the azido-aniline hydrochloride onto the bare electrode, which is then followed by clicking the MPc onto the electrode via the alkyne terminated MPc, resulting in a more robust and stable films.[1] This asymmetrical modification coupled with carefully chosen analyte-targeting and other biological substituents. The latter class includes flavonoids, chromones, coumarins, alkaloids. For example flavonoids exhibit very important biological activities such as anti-inflammatory, cytotoxicity and antiviralactivities,[2, 3] will be utilized to increase the selectivity and sensitivity of the chemically modified electrodes for targeted electrocatalytic determination of pollutants in the main water reservoirs in KwaZulu-Natal. These interactions would be facilitated through structure similarity or biological effects affinity.

6.3. References

1. İpek, Y.; Dinçer, H.; Koca, A., *Sensors and Actuators B: Chemical* **2014,** *193*, 830-837.

2. Kale, M.; Patwardhan, K., *Journal of Current Pharma Research* **2014,** *4*, 1150.

3. González-Paramás, A. M.; Ayuda-Durán, B.; Martínez, S.; González-Manzano, S.; Santos-Buelga, C., *Current medicinal chemistry* **2019,** *26*, 6976-6990.